HYGRIC PERFORMANCE ASSESSMENT OF AUTOCLAVED AERATED CONCRETE TREATED WITH NANO DISPERSIVE CALCIUM HYDROXIDE SOLUTION

A THESIS SUBMITTED TO
THE GRADUATE SCHOOL OF NATURAL AND APPLIED SCIENCES
OF
MIDDLE EAST TECHNICAL UNIVERSITY

BY

GELAREH TANIDEH

IN PARTIAL FULFILLMENT OF THE REQUIREMENTS
FOR
THE DEGREE OF MASTER OF SCIENCE
IN
BUILDING SCIENCE IN ARCHITECTURE

FEBRUARY 2022

Approval of the thesis:

HYGRIC PERFORMANCE ASSESSMENT OF AUTOCLAVED AERATED CONCRETE TREATED WITH NANO DISPERSIVE CALCIUM HYDROXIDE SOLUTION

submitted by **GELAREH TANIDEH** in partial fulfillment of the requirements for the degree of **Master of Science in Building Science in Architecture, Middle East Technical University** by,

Prof. Dr. Halil Kalıpçılar
Dean, Graduate School of **Natural and Applied Sciences** _____

Prof. Dr. Fatma Cânâ Bilsel
Head of the Department, **Architecture** _____

Assoc. Prof. Dr. Ayşe Tavukçuoğlu
Supervisor, **Architecture, METU** _____

Prof. Dr. Emine Nevin Caner-Saltık
Co-Supervisor, **Architecture, METU** _____

Examining Committee Members:

Prof. Dr. Sinan Turhan Erdoğan
Civil Engineering, METU _____

Assoc. Prof. Dr. Ayşe Tavukçuoğlu
Architecture, METU _____

Prof. Dr. Gülser Çelebi
Interior Architecture, Çankaya University _____

Date: 04.02.2022

I hereby declare that all information in this document has been obtained and presented in accordance with academic rules and ethical conduct. I also declare that, as required by these rules and conduct, I have fully cited and referenced all material and results that are not original to this work.

Name, Last name: Gelareh Tanideh

Signature:

ABSTRACT

HYGRIC PERFORMANCE ASSESSMENT OF AUTOCLAVED AERATED CONCRETE TREATED WITH NANO DISPERSIVE CALCIUM HYDROXIDE SOLUTION

Tanideh, Gelareh
Master of Science, Building Science in Architecture
Supervisor: Assoc. Prof. Dr. Ayşe Tavukçuoğlu
Co-Supervisor: Prof. Dr. Emine Nevin Caner-Saltık

February 2022, 132 pages

The focus of the study is to uncover whether the treatment of autoclaved aerated concrete (AAC) surface with alcohol dispersion of calcium hydroxide $Ca(OH)_2$ nanoparticles controls its high water absorption properties to some extent or not. AAC as a lightweight and porous concrete material, is well-known for its high breathing and thermal resistivity features while it suffers from high water absorption and capillary suction in exposed conditions. Laboratory analyses were conducted on four types of AAC, used as thermal insulation board, masonry infill unit, precast structural elements, and load-bearing masonry units. For the examinations, the nano dispersive $Ca(OH)_2$ solution prepared at laboratory conditions was penetrated from exposed surfaces of AAC samples by capillary suction. The performance properties of the untreated and treated AAC samples were examined in terms of basic physical, physicomechanical, and hygric properties, with emphases on water vapor permeability, capillary suction, and fine porosity characteristics. The impact of the nano solution on the fine pores of AAC types and its penetration depth was

monitored mainly with ultrasonic testing, image analyses of cross-sections by optical microscopy, and XRD analyses. The results show that the penetration of nano dispersive $Ca(OH)_2$ solution reduces the capillary water suction to a certain extent on the surface perpendicular to the rising direction, which is the actual exposed surface at constructions. The physicomechanical properties of AAC products enhance after treatment while their inherent high breathing features are still kept. In addition, for in-situ monitoring of untreated and treated AAC surfaces the relevant ultrasonic reference data were established.

Keywords: Autoclaved aerated concrete (AAC), Alcohol dispersion of calcium hydroxide ($Ca(OH)_2$) nano particles, Hygric properties, Capillary suction, Ultrasonic testing

ÖZ

NANO TANELİ KALSİYUM HİDROKSİT SOLÜSYONU EMDİRİLMİŞ GAZBETONUN HİGRİK ÖZELLİKLERİNİN TAYİNİ

Tanideh, Gelareh
Yüksek Lisans, Yapı Bilimleri, Mimarlık
Tez Yöneticisi: Doç. Dr. Ayşe Tavukçuoğlu
Ortak Tez Yöneticisi: Prof. Dr. Emine Nevin Caner-Saltık

Şubat 2022, 132 sayfa

Bu çalışmanın temel amacı, otoklavlanmış gaz beton (AAC) yüzeyinin kalsiyum hidroksit ($Ca(OH)_2$) nano taneli solüsyonu emdirilmesi ile, gaz betonun yüksek su emme özelliklerini belirli bir seviyede kontrol edip etmediğini ortaya çıkarmaktır. Gaz beton, hafif ve gözenekli beton malzemesi olarak, yüksek nefes alma ve ısıl direnç özellikleri ile bilinirken, açık hava koşullarına maruz kaldığında yüksek düzeyde su emme ve kılcal su emme özellikleri sıkıntı yaratmaktadır. Bu çalışmada, ısı yalıtım levhası, duvar dolgu bloğu, prekast yapı elemanları, ve taşıyıcı duvar bloğu olarak kullanılan dört tip gaz beton örnekleri ile laboratuvar analizleri yapılmıştır. İncelemeler için laboratuvar koşullarında hazırlanan nano taneli $Ca(OH)_2$ çözeltisi, gaz beton numunelerinin açıkta kalan yüzeylerine kapiler emme ile nüfuz ettirilmiştir. Emdirme işlemi yapılmamış (kontrol) ve emdirme işlemi yapılmış gaz beton numunelerinin performans özellikleri, temel fiziksel, fizikomekanik ve higrik özellikler açısından incelenmiş, su buharı geçirimliliği, kılcal emme ve ince gözeneklilik özelliklerine odaklanılmıştır. Nano taneli

solüsyonun, gaz beton tiplerinin ince gözeneklerine etkisi ve nüfuz ettiği derinliği, ultrasonik ölçümler, optik mikroskop ile örnek kesitlerinin görüntü analizleri ve XRD analizleri ile izlenmiştir. Sonuçlar, nano taneli $Ca(OH)_2$ çözeltisinin, özellikle de gaz betonun inşaatlarda kullanımı esas alındığında, dış ortam tarafında kalan yükselme yönüne dik yüzeyine uygulandığında, kılcal su emme düzeyini belirli seviyede azalttığını göstermektedir. Emdirme işlemi ile muamele edilen gaz beton ürünlerinin fizikomekanik özellikleri belirgin düzeyde artarken, gaz betonun kendine özgü olan yüksek nefes alma nitelikleri korunabilmiştir. Ek olarak, muamele edilmiş ve edilmemiş gaz beton yüzeylerinin yerinde izlenebilmesini sağlayacak olan ultrasonik muayene yönteminin uygulama kriterleri tanımlanmış ve ilgili ultrasonik referans verileri oluşturulmuştur.

Anahtar Kelimeler: Otoklavlanmış gaz beton, $Ca(OH)_2$ nano partikülleri içeren alkol dispersiyonu, Higrik özellikler, Kılcal su emme, Ultrasonik muayene

To my beloved family,

ACKNOWLEDGEMENTS

First of all, I would like to express my sincere thanks to my thesis supervisor, Assoc. Prof. Dr. Ayşe Tavukçuoğlu for her guidance, support, patience, and constant encouragement in this long journey. I appreciate her time and feedback tremendously, especially her recommendations that have lightened my way. I would also like to thank my co-supervisor, Prof. Dr. Emine Caner Saltık, for her invaluable support and extensive knowledge, experience, and keen insight into the subject.

In addition to my advisor, I would like to thank all members of the thesis examining committee, namely Prof. Dr. Sinan Turhan Erdoğan and Prof. Dr. Gülser Çelebi, for accepting to be a part of the committee and their valuable time and feedback.

I should extend my gratitude to my dearest friends Fatıma Erol, Fulya Karahan Dağ, and Meltem Erdil for their help with the experimental part of the work and invaluable discussions throughout the study.

Finally, I would like to express my gratitude to my mother Farisa, my father Alireza, and my brother Martia, who have always believed in me in my life and for their unconditional support, love, and patience. Thank you for constantly reminding me of the importance of positivity and kindness. Thank you for raising me right. This thesis is dedicated to them.

TABLE OF CONTENTS

LIST OF TABLES

TABLES

LIST OF FIGURES

FIGURES

CHAPTER 1

INTRODUCTION

Fine aggregates and foaming additives have been used to lower the weight of concrete since Roman times. The reaction of an alkaline binder (cement and lime) with acid was the first attempt of Hoffmann in 1889 to lighten the weight of aerated concrete by releasing carbon dioxide (CO_2). Aylsworth and Dyer then used aluminum powder and calcium hydroxide to make porous cementitious materials in 1914. Aerated concrete was first invented in 1922 by a Swedish engineer. It was subsequently followed by Eriksson in 1923 to develop the modern autoclaved aerated concrete (AAC) through a pressurized steam curing process known as autoclaving, which reduced drying shrinkage and increased material strength. These experiments and innovations drew considerable attention and further refinements were made to improve the performance of AAC. Thus, in 1929, the first factory of AAC was established. Panels and lintels were the first reinforced AAC components manufactured in 1935. AAC has been employed in building construction since the early stages of the 20th century (Fudge *et al*., 2019; Gökmen, 2017; Boggelen, 2014).

Autoclaved Aerated Concrete (AAC), commonly known as autoclaved cellular concrete, is a highly porous material containing a large number of closed air pores (Liu *et al*., 2021). AAC is composed of fine aggregates such as sand or fly ash mixed with cement and water along with aluminum powder as expanding factor. The formation of porous structure in AAC materials is mainly influenced by aluminum powder. The porosity matrix of AAC materials consists of micron-scale tobermorite crystals and mm-scale air pores (Ioannis *et al*., 2008; Sherin and Saurabh, 2018). AAC is a lightweight material whose lightness is achieved through chemical reactions during the mixing process (Liu *et al*., 2021). AAC products are produced for various applications such as thermal insulation boards, masonry infill units, load-

bearing masonry units, and prefabricated structural elements, including wall panels, floor panels, roof panels, and lintels. Since AAC products can be sanded and cut to the desired size with drills and hand saws, their on-site installation can be accomplished easily and quickly (Sherin and Saurabh, 2018).

In comparison to other traditional construction materials, AAC is recognized as a green building material by LEED (Leadership in Energy and Environmental Design) and the USGBC (US Green Building Council) (Li *et al*., 2018). With the advantages of high breathability, low density, low thermal conductivity, fire resistance, and good sound insulation due to a large number of air voids, AAC materials are widely used in building construction (Qu and Zhao, 2017; Li *et al*., 2018; Liu *et al*., 2021). However, high water absorption propeties of AAC materials restricts them from being used as external blocks (Sherin and Saurabh, 2018). The exposed surface of the AAC blocks experiences significant water penetration through capillary suction due to the highly porous structure of the AAC materials. Water-saturated AAC samples show lower durability in weathering conditions. Moreover, the compressive strength, tensile strength, thermal conductivity, and breathability of AAC materials decrease as the moisture content increases. Therefore, the exposed surface of AAC blocks should be coated to control water absorption and capillary water suction properties (Vejmelkova *et al*., 2009; Duano *et al*., 2021). Surface coating applications contribute to the extended service life of AAC materials (Kus and Norberg, 1999; Kus, 2003). Various methods are used in the literature to reduce the water absorption properties of AAC products. Plasters and paints applied in layers, which is one of the techniques commonly used to reduce water absorption in AAC materials, disturb the high breathable feature of AAC while forming a water-impermeable outer skin (Kus and Norberg, 1999; Sezemanas *et al*., 2013; Duano *et al*., 2021).

Alcohol dispersion of calcium hydroxide ($Ca(OH)_2$) nano particles is a commonly used solution for consolidating calcareous materials, which replaced the traditional water-saturated mixture of calcium hydroxide (lime-water) due to their nano-size particles that lead to deep deposition and penetration into fine and capillary pores

(Davey, 1961; Borsoi, 2017; Fernandeza *et al*., 2017). Calcium hydroxide particles react with carbon dioxide (CO_2) in the air and convert to calcium carbonate (calcite crystals) under high relative humidity conditions (Giorgi *et al*., 2010). This carbonation process is faster alcohol dispersion of $Ca(OH)_2$ nano particles as alcohols evaporate very quickly (Daehne and Herm, 2013).

Nano dispersive ($Ca(OH)_2$) solution is used in this study to improve the hygric properties of AAC materials. Since lime is one of the raw material components of AAC products, the treatment with nano ($Ca(OH)_2$) solution is considered compatible with AAC materials. The main purpose of this research is to reduce the capillary water absorption behavior of AAC products by filling the capillary pores of the exposed surface with nano dispersive $Ca(OH)_2$ solution to a certain depth and forming nano calcium carbonate ($CaCO_3$) particles in the pores while maintaining the breathability of the AAC blocks. To this end, comprehensive material analyses, including standard laboratory tests, were performed to determine the material properties of untreated (control) AAC samples and treated AAC samples with the alcohol dispersion of $Ca(OH)_2$ nano particles in terms of physical, hygric, and physicomechanical properties.

In this chapter, the argument and research objectives on which this thesis is based, along with a brief overview of the research procedure performed in the study and the content of the remaining chapters are presented following subheadings.

1.1 Argument

As a lightweight, high porous, high breathable nature, high fire-resistant, earthquake resistant, sound insulation, and enough strength to be used as masonry building materials, Autoclave Aerated Concrete (AAC) meets all these requirements that increase its popularity in the construction market (Taşdemir and Ertokat, 2002; Korniyenko *et al*., 2016; He *et al*., 2018; Fudge *et al*., 2019). However, the high water absorption and high capillary water suction properties make AAC materials

susceptible to weathering cycles. The presence of fine and capillary pores higher in quantity results in significant water penetration from the exposed surface of the AAC blocks by capillary suction. As the pores fill with water, the strain on the pore wall increases, resulting in crack formation. Moreover, the performance of water-saturated AAC materials is reduced in terms of compressive strength, tensile strength, and durability. Therefore, the exposed surface of AAC materials should be protected from water penetration to reduce the adverse impact of weathering conditions such as wetting-drying and freezing-thawing (Korniyenko *et al*., 2016; Fudge *et al*., 2019). Exterior coatings are applied to AAC materials to improve functionality and abrasion resistance while also controlling capillary water suction properties. Coating materials for the protection of AAC building structures should be selected based on their compatibility with AAC properties (Fudge *et al*., 2019). Surface defects such as flakes, scales, and cracks can appear if AAC materials are coated without considering their characteristics (Andolsun, 2006). In addition, incompatible plasters and paints applied in layers disturb the high breathable feature of AAC while forming a water-impermeable outer skin. The water vapor permeability, thermal conductivity, and mechanical strength of AAC materials are reduced in the presence of moisture and water. Therefore, to avoid related problems, materials that keep AAC breathable and water vapor permeable should be used for coating purposes (Kuş, 2002; Felekoğlu, 2004).

The alcohol dispersion containing $Ca(OH)_2$ nano particles can be a suitable option for coating the exterior surfaces of AAC products to reduce their water permeability properties. As an adaptable, durable, and long-lasting surface coating material, calcium hydroxide (lime) is compatible with most construction materials, and its application goes back to ancient times (Mold and Godbey, 2005). The aim of using calcium hydroxide nanoparticles is to improve their dispersion and solubility in water and, consequently, increase their performance in surface coatings. In addition, alcoholic solvents are added to the water mixture to accelerate the carbonation rate of the calcium hydroxide nanoparticles. Nanoparticles penetrate the fine pores and capillaries of the AAC material, reducing capillary absorption while keeping the

material breathable. This is a new approach to coating construction materials instead of using traditional plastering and painting techniques. The alcohol dispersion of $Ca(OH)_2$ nano particles, which can be prepared in various concentrations and particle size distributions, is a promising method for the consolidation of calcareous stones. Its impact on the performance properties of AAC has not been examined yet in the literature. In this regard, the study is shaped to better understand whether nano dispersive ($Ca(OH)_2$) solution, when penetrating the fine capillaries of AAC, can improve the physicomechanical and hygric properties of AAC or not.

1.2 Aim and Objectives

The study's main target is to find a way out to control the high water absorption of autoclaved aerated concrete (AAC) products. The study examines the potentials of a solution, namely the alcohol dispersion containing calcium hydroxide nanoparticles when used as a surface treatment material, in this regard. The research aims to uncover whether the calcium hydroxide nanoparticles' alcohol dispersion reduces their high water absorption properties to some extent or not when it is penetrated through the exposed surfaces of autoclaved aerated concrete (AAC) products.

Considering the research scope, the objectives of the study are as follows:

- to define material properties of the examined AAC products with an emphasis on their hygric properties;
- to prepare the alcohol dispersion of calcium hydroxide nanoparticles for surface treatment,
- to assess the effectiveness of the treatment by the analyses of AAC products before and after treatment in terms of physical, hygric, and physicomechanical properties with emphases on water vapor permeability, capillary suction, fine porosity, and ultrasonic pulse velocity characteristics,

— to discuss the impacts of the nano dispersive $Ca(OH)_2$ solution, if used as surface treatment or consolidation treatment based on changes in hygric and physicomechanical performances of the AAC products,
— to evaluate the potentials of ultrasonic testing for in-situ monitoring purposes and establish the reference ultrasonic pulse velocity (*UPV*) data taken in direct and indirect transmission modes from untreated and treated AAC samples for the in-situ *UPV* measurements,
— to discuss the achieved data for the improvement of international standards related to the production and performance properties of AAC products.

1.3 Thesis Structure

This study is presented in 6 chapters, the first of which is introduction. The argument, aim and objectives of the study are presented in this chapter. In addition, the structure of the thesis is explained in the disposition part.

In the second chapter, a comprehensive literature review was conducted on material properties of AAC in terms of raw material properties, physical properties, hygric properties, and physicomechanical properties, along with different techniques used to control capillary water suction properties of AAC materials. Also, a compilation of national and international standards used for the production, performance, and construction of AAC products are given. Lastly, the material properties of examined AAC products in this study are introduced. In the second place, the production process of calcium hydroxide (lime), its carbonation under high relative humidity conditions, and replacement of alcohol dispersion of calcium hydroxide ($Ca(OH)_2$) nano particles with the saturated lime-water mixture for consolidation of stone structures are briefly described.

In the third chapter, AAC products were sampled. The methodology for the experimental laboratory tests conducted for the study is described clearly under the

headings of basic physical, hygric, physicomechanical, mineralogical and microstructural properties.

In the fourth chapter, experimental results are given. The properties of both control AAC samples and AAC samples treated with nano dispersive $Ca(OH)_2$) solution are explained with relevant tables, graphics and figures.

In the fifth chapter, the results are discussed in terms of the material properties of examined AAC products, performance evaluation of alcohol dispersion of calcium hydroxide nanoparticles on hygric and physicomechanical properties of AAC products, guiding remarks for reliable UPV measurements of AAC samples, and improvement of international standards related to AAC products.

Finally, as a conclusion part, the last chapter includes a summary of the findings of the study, as well as recommendations for further research.

CHAPTER 2

LITERATURE REVIEW

In this chapter, a brief literature review was done, especially on the material properties of autoclaved aerated concrete (AAC) in terms of raw material properties, physical properties, hygric properties, and mechanical properties, which contribute to its unique performance. A compilation of various treatment methods used in the literature to improve the material properties of AAC was reviewed. Moreover, the standards related to the AAC production, performance, and construction are summarized. The material properties of the examined AAC products were then introduced. Here, the characteristics of nano calcium hydroxide ($Ca(OH)_2$), known as nano-lime, and the carbonation process to better define its compatibility with calcareous materials, as well as its utilization in the consolidation of stone elements to improve their performance, were investigated. Lastly, the treatment of hygric properties of AAC materials has been identified as the main focus of this study.

2.1 Material Properties of Autoclaved Aerated Concrete (AAC)

AAC is an autoclaved calcium-silicate mortar that contains sand and/or fly ash, lime, cement, expanding agent (Al, Zn, H_2O_2), and water. The expanding agent is the main factor in the formation of large pores, which reduces the density of AAC materials (Narayanan and Ramamurthy, 2000b; Qu and Zhao, 2017; Qin and Gao 2019). AAC is defined in Turkish Standards as a lightweight concrete produced by mixing three main components of fine siliceous aggregate, binder (lime or cement), and a pore-forming agent to reduce density, followed by autoclaving process to increase mechanical strength (TS EN 12602;2011).

In the production process of AAC, sand or fly ash is first finely grouted and mixed with water. Then this slurry is mixed with lime, cement, expansion agent and some extra amount of water in an automatic mixer. The final mixture is then poured into molds, where the expansion agent reacts with the other ingredients, allowing the mixture to grow and form a cake in the mold. During this expansion process, millions of finely dispersed air pores are formed in the concrete. For reinforced products, reinforcement mesh of anti-corrosion treated steel is placed in the mold before concrete is poured. The semi-solid material is then cut by wires and put in autoclaves under the pressure of steam to cure for several hours. AAC items are now ready to be packaged and shipped (**Figure 2.1**) (Ioannou *et al*., 2008). Aluminum powder is the most widely used expansion agent in AAC production. The performance of the aluminum powder is influenced by factors such as particle size and purity of aluminum content, cement alkalinity, and techniques used to prevent gas from escaping before the mortar hardens (Narayanan and Ramamurthy, 2000b). Recently, some wastes, such as municipal solid waste, have been used as an aerating agent and active silicon source instead of traditional aluminum powder. In addition, the use of industrial by-products in AAC production has attracted the attention of scientists as they contribute to recycling waste. The presence of air pores makes AAC brittle. Therefore, the use of fiber in AAC production can increase the elasticity of the material by bridging micro and macro cracks (Qu and Zhao, 2017).

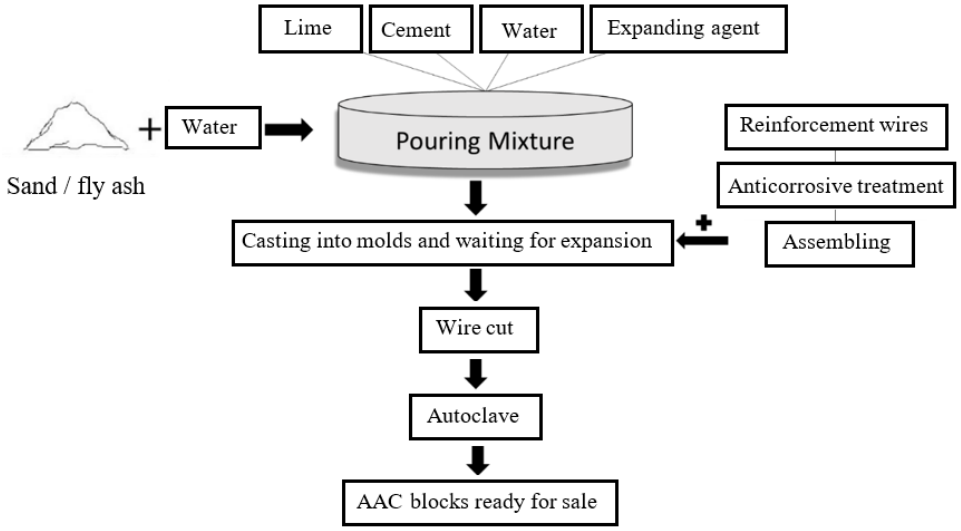

Figure 2.1. Production process of Autoclaved Aerated Concrete.

2.1.1 Raw Material Properties of AAC

According to the investigation of X-Ray Powder Diffraction (XRD), Tobermorite ($C_5S_6H_5$) is the main mineral of AAC materials. The important characteristics of the AAC materials, including structural strength and heat conductivity, are partially dependent on the Tobermorite crystals (Schreiner *et al*., 2019). Therefore, it is important to investigate the formation and amount of Tobermorite crystallinity during the autoclave process (Matsui *et al*., 2011).

Tobermorite is a natural calcium silicate hydrate (C-S-H) formed after autoclaving AAC materials under hydrothermal circumstances (Schreiner *et al*., 2019). Hydrothermal reactions between lime (CaO), cement, aluminum powder (Al_2O_3), and water (H_2O) occur before autoclaving (Drochytka and Černý 2020). Calcium hydroxide ($Ca(OH)_2$) is formed by the hydration of lime (**Figure 2.2** reaction 1). In the hydration of cement, alite and belite as cement minerals convert to C-S-H and CH, respectively (**Figure 2.2** reactions 2 and 3). CH reacts with aluminum powder to produce calcium aluminate hydrates and hydrogen gas (**Figure 2.2** reaction 4). The released hydrogen gas is the main factor in forming aeration pores. During autoclaving process, calcium aluminate hydrates which mainly composed of C-A-H and C-S-H react with silica to form Tobermorite (**Figure 2.2** reactions 5 and 6) (Beltagui *et al*., 2017). The production process of Tobermorite is summarized in **Figure 2.2**. Depending on the raw materials used for AAC production, different peaks appear in the XRD trace. The general XRD trace of AAC material is shown in **Figure 2.3**.

Tobermorite can be easily produced from Ca-rich CSH gels compared to Si-rich CSH gels (Drochytka, 2020). Therefore, the ratio of Ca/Si has a significant effect on the structure and micro-morphology of crystallization. Various Tobermorite morphologies that obtained by Scanning Electron Microscopy (SEM) are shown in **Figure 2.4**. The more silica consumed during the reaction, the higher plate-like Tobermorite is produced, resulting in a lower Ca/Si ratio (**Figure 2.4 a**). If the Ca/Si ratio is more than one (>1), short silica chains transform the Ca-rich C-S-H into

needle-like Tobermorite crystals (**Figure 2.4 b**). At a low Ca/Si ratio (<0.8), grass-type Tobermorite structures are formed (**Figure 2.4 c**). The ideal Ca/Si ratio for the formation of Tobermorite is typically in the range of 0.8 to 1. If the values are outside the specified range, compressive strength can be reduced, and AAC shrinkage can be increased (Qu and Zhao, 2017).

Before Autoclaving (Hydration Process)

$$CaO + H_2O \rightarrow Ca(OH)_2 \quad (1)$$
$$C + H \rightarrow C\,H \quad (2)$$
$$C_3S + H \rightarrow CH + C - S - H \quad (3)$$
$$CH + A \rightarrow C - A - H + H_2 \quad (4)$$

After Autoclaving (Formationt of Tobermorite)

$$C - A - H + S \rightarrow C_5S_6H_5 \quad (5)$$
$$C - S - H + S \rightarrow C_5S_6H_5 \quad (6)$$

Figure 2.2. Simplified process of the Tobermorite formation in AAC production (Beltagui *et al*., 2017).

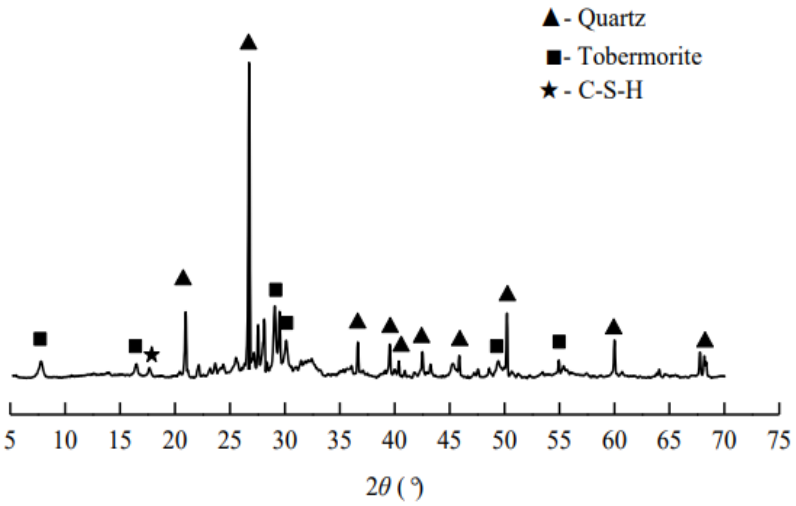

Figure 2.3. Simplified process of the Tobermorite formation in AAC production (Beltagui *et al*., 2017).

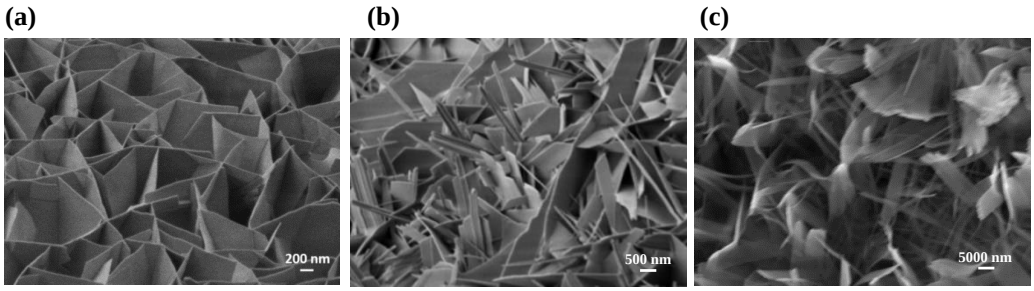

Figure 2.4. SEM images of Tobermorite morphologies produced in various AACs with different Ca/Si ratios; **a)** plate-like; **b)** needle-like; **c)** grass-like (Charakterisierung and Fakult, n.d.; Mostafa, 2005; Schreiner *et al.*, 2019).

In addition to the Ca/Si ratio, the autoclaving time and temperature also affect the formation and amount of Tobermorite crystalline phases. However, prolonged pressure in the autoclave limits the formation of Tobermorite. Since various autoclave systems or steam pressures are used in the production of AAC materials, a specific time for autoclaving is not defined (Melichar *et al*., 2018). According to the study done by Mostafa (2005), the intensity of Tobermorite formation remained unchanged after 2 hours of autoclaving. While Kunchariyakun *et al*. (2015) reported that even by increasing the autoclaving time from 8 hours to 18 hours, the intensity of the Tobermorite phase remained constant after 8 hours of autoclaving (Qu and Zhao, 2017). Aluminum content is the other factor that affects the formation of Tobermorite. Only a small amount of aluminum can speed up the commencement of Tobermorite formation by decreasing the autoclaving temperature and time (Qu and Zhao, 2017; Melichar *et al*., 2018). The reactivity of the silica source as well as the addition of alkali and sulfate compounds have an impact on Tobermorite formation (Drochytka and Černý, 2020).

Tobermorite and well-crystallized C-S-H, as the main structural elements of AAC materials, react with carbon dioxide (CO_2) in an environment with higher relative humidity and temperature, transforming into silica gel and calcium carbonate ($CaCO_3$). This process is known as carbonation, and it is one of the major sources of AAC deterioration as it ages (Matsushita *et al*., 2000). In addition to humidity and temperature, factors such as CO_2 concentration, material quality, mix design, loading state, and curing condition all have an impact on the carbonation process. The higher the amount of carbon dioxide, the higher the rate of carbonation process. AAC material in good quality without any cracks is less affected by the carbonation process. Cracks provide a direct path for CO_2 to enter, resulting in early chemical deterioration of the concrete. In the raw material mix of AAC, increasing the ratio of water to cement or sand to binder can result in greater porosity, which increases the rate of carbonation. Low-level compressive stress inhibits micropores or microcracking, thereby reducing interconnected pores, resulting in carbonation resistance. The pore structure of AAC has a significant impact on the carbonation

process because CO_2 diffusion is dependent on the intensity of linked pores (Qiu, 2020). Carbonation reduces the strength and frost resistance of AAC, resulting in increased deflection, shrinkage, and lattice-like cracks (Qu and Zhao, 2017). It is worth noting that the carbonation process is slow in natural atmospheric conditions due to the lower concentration of CO_2 in the air (Koronthalyova and Bagel, 2015).

2.1.2 Physical Properties of AAC

Density is the main parameter in determining material properties. The physical properties of AAC materials are affected by bulk density (Różycka and Pichór, 2016). The bulk density of AAC depends on the amount of aluminum powder in the mixture and the water/solid ratio. The water/solid ratio should not be low or high; otherwise, inadequate aeration or pore rapture will occur, resulting in higher density. Therefore, the required amount of water is determined by the consistency of the mixture instead of a predetermined amount (Andolsun, 2006; Sherin and Saurabh, 2018). Bulk density, thermal conductivity, and compressive strength are three interrelated properties of AAC. The compressive strength and thermal conductivity of AAC increase as the unit weight of the material increases (Qu and Zhao, 2017). The dry density range of AAC is between 0.30–1 g/cm^3 according to the European Standard BS EN 12602:2016 (TS EN 12602 in Turkish) (**Table 2.1**).

Table 2.1. Dry Density Classes of Autoclaved Aerated Concrete (EN 12602:2016).

Density Class	**0.30**	**0.35**	**0.40**	**0.45**	**0.50**	**0.55**	**0.60**	**0.65**
Dry Density (g/cm^3)	>0.25 ≤0.3	>0.3 ≤0.35	>0.35 ≤0.4	>0.4 ≤0.45	>0.45 ≤0.5	>0.5 ≤0.55	>0.55 ≤0.6	>0.6 ≤0.65
Density Class	**0.70**	**0.75**	**0.80**	**0.85**	**0.90**	**0.95**	**1**	
Dry Density (g/cm^3)	>0.65 ≤0.7	>0.7 ≤0.75	>0.75 ≤0.8	>0.8 ≤0.85	>0.85 ≤0.9	>0.9 ≤0.95	>0.95 ≤1	

AAC with a density higher than 0.35 g/cm^3 can be used as load-bearing material, while AAC with a lower density is appropriate for thermal insulation. The variation in the pore volume of AAC leads to the production of AAC materials in a wide range

of densities that can be used for a variety of applications (Andolsun, 2006; Wakili *et al*., 2015). Density variations mostly depend on the number of aeration pores. Pore distances in AAC can range from one millimeter to zero millimeters, meaning that the pores are in contact or even linked. Since the air pores in low-density AAC materials are in contact with each other, spherical pores can be deformed as a result of these encounters (Schober, 2011). AAC materials used in the construction process are determined to have higher densities than initial dry densities due to their moisture absorption feature. AAC materials can absorb water in the range of 25 to 35% by mass of dry material and even up to 45% by mass in low-density ranges after manufacturing (Aroni, 2004). AAC carbonation can also occur due to changes in relative humidity and temperature, which increase the initial dry density (Andolsun, 2006).

Porosity is the other factor that can affect the density of AAC materials. Shrinkage, permeability, strength, diffusivity, and creep are all dependent on the porosity and pore size distribution of AAC (Narayanan and Ramamurthy, 2000a). One of the salient features of AAC is its special pore structure (He *et al*., 2018). The ratio of pore volume in AAC ranges from 65 to 90%, resulting in lower density materials (Schober, 2011; Qu and Zhao, 2017). As the porosity increases, the thermal conductivity decreases due to the formation of air pores, which is considerably influenced by the addition of the expanding agent (Chen *et al*., 2021).

The pore structure of AAC consists of aeration pores, micropores, and mesopores. Aeration pores, also known as macro pores, are the most visible pores in AAC, which are formed as air pores in the wet mix after the addition of the expanding agent and then transformed into nearly spherical voids (**Figure 2.5 a**). Although these aeration pores are separated from each other, they are actually interlinked together by the underneath microporous system. When AAC is broken or cut in the finished state, these large pores provide the characteristic surface of the material. The air pores formed in the AAC manufacturing process contribute 25 to 70% of the total pore volume, ranging from 65 to 90%. Therefore, aeration pores occupy the largest pore volume in AAC materials. Micropores contain all the porosity around aeration pores.

They are composed of a cruciform aggregation of Tobermorite with thin platelets, resembling a system of sharp-edged box cells (**Figure 2.5 b**). Micropores are the major contributor to capillary suction as they consist of microcapillaries smaller than 50 nm in diameter and macro capillaries from 50 nm to 50 µm. The space between aeration pores and micropores is filled by mesopores. Mesopores are shrinkage cracks that occur at various phases of the production process. These cracks are either unfilled or bonded with a network of Tobermorite platelets larger than those found in the matrix (**Figure 2.5 c**). These cracks play a significant role in the AAC pore structure by connecting most air pores. Therefore, AAC has an open cellular structure. However, AAC with a density higher than 0.55 g/cm^3 can have pore distances large enough to form a closed cellular system of air pores. The cracks orientation is perpendicular to the rising direction of AAC. Eventually, it should be noted that the total porosity is not greatly affected by the mesopores. (Narayanan and Ramamurthy, 2000a; Andolsun 2006; Ioannou *et al*., 2008; Schober, 2011; Qu and Zhao, 2017; Matsuno *et al*., 2020; Chen, *et al*., 2021).

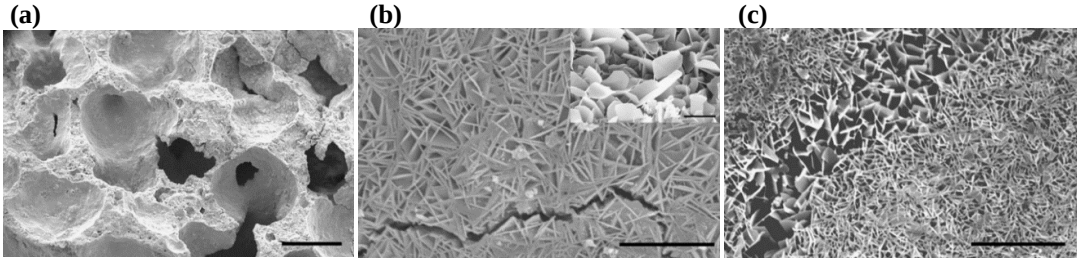

Figure 2.5. a) Low magnification view of AAC microstructure: aeration pores (scale bar is 500 µm); **b)** High magnification view of AAC microstructure, showing Tobermorite platelets and a mesopore crack. (scale bar in main image is10 µm, smaller corner image is a higher magnification of the plate-like pore structure and scale bar is 5 µm); **c)** High magnification view of AAC microstructure: mesopore, filled with coarse Tobermorite (scale bar is 20 µm) (Ioannou *et al*., 2008).

The illustration of AAC microstructure according to the description of Schober (2005) is presented in **Figure 2.6**. AAC pore structure can be affected by the expanding powder dosage and mixing time. In addition, the water/solid ratio in the raw material composition determines the total volume of micropores, so that a transition from micropores to macropores and vice versa is possible within a certain range (Schober, 2005; Chen *et al*., 2021). As the macropore ratio increases, the

amount of micropores decreases, which contributes to the higher apparent density (**Table 2.2**). In addition, the apparent density is influenced not only by porosity but also by the pore size distribution (Schober, 2005).

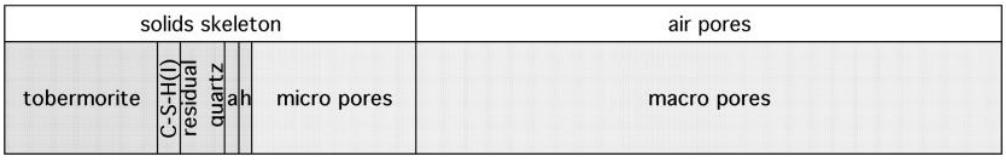

Figure 2.6. Schematic representation of volume parts in the structure of aircrete (a = anhydrite, h = hydrogarnet). Apparent density is about 0.40 g/cm^3 in this case, and raw materials are: pure quartz sand, lime, portland cement, anhydrite and water (Schober, 2005).

Table 2.2. Porosity characteristics of AAC products which differ in density (Schober, 2005).

Apparent Density	**Macropores**	**Micropores**	**Total Porosity**
g/cm^3	%	%	%
0.10	83	13	0.96
0.15	77	17	0.94
0.35	70	16	0.86
0.40	65	19	0.84
0.60	45	21	0.76
0.80	27	41	0.68

Pore size and distribution are major elements in determining the durability of the material, which is defined by its water saturation coefficient (*S-value*). The water saturation coefficient is one of the variables for evaluating the resilience of porous materials to freezing-thawing and wetting-drying cycles. A saturation coefficient of 0.80 is considered a threshold value for calcareous materials, meaning that the material is 80% water-saturated and susceptible to freeze-thaw cycles above this value (Hirschwald, 1908; RILEM, 1980; BRE, 1997; Ordonez *et al.*, 2003; Topal and Sözmen, 2003; Chen, 2004). AAC materials were examined for their *S-values* in the study conducted by Andolsun (2006). Results determined that AAC material with higher density had a higher *S-value* than the lower density AAC material. Both obtained values were less than 0.8, indicating that they are frost-resistant (**Table 2.3**).

Table 2.3. The results of water saturation coefficients (*S-value*) of AAC (Andolsun, 2006).

Bulk Density g/cm^3	**Porosity** (%)	**Water Saturation Coefficient (*S-value*)** unitless
0.40	78	0.46
0.60	69	0.62

2.1.3 Hygric Properties of AAC

The hygric characteristics of materials are essential input parameters for analyzing moisture-related issues (Feng *et al*., 2015). AAC can transport large amounts of vapor and moisture due to its pore structure (Jacobs and Mayer, 1992). Porosity, pore size distribution, and pore geometry are three fundamental components of AAC pore structure (Chen *et al*., 2021). The pore structure of AAC can affect its permeability characteristics. Permeability is defined as the passage of fluid or gas through a porous material under the influence of a pressure differential. The permeability characteristic depends on pore size, type, and distribution rather than pore volume. Open pores, which are connected to the outer boundary of the material, increase the permeability of AAC, because closed pores are separated from the outside and are mainly used for sound and thermal insulation or low-weight structural components. **Figure 2.7** shows the relationship between pore types and permeability. Materials with open-pore structures have high permeability properties (Hamad, 2014).

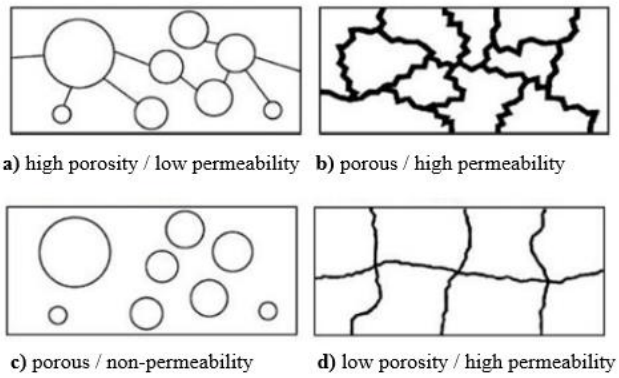

Figure 2.7. Schematic diagram exhibiting differences between porosity and permeability (Hamad, 2014).

Water vapor transmission is defined as water vapor permeability or water vapor diffusion resistance index (*μ-value*), while water transfer is explained by capillary absorption and water permeability (Andolsun, 2006). Water vapor transmission is considered the primary transport system in the low to medium relative humidity range compared to the liquid water and liquid-vapor phase transitions in porous building materials (Tian *et al*., 2019). In the case of dry AAC components, the transfer of water vapor is the dominant action by the empty pores, but when exposed to water, the pores are filled with water due to the dominance of capillary absorption (Andolsun, 2006). The water vapor diffusion resistance index (*μ-value*), which relies on dry density, is crucial for calculating moisture transfer in porous construction materials. Factors such as temperature and relative humidity can affect the *μ-value*. The *μ-value* increases with increasing temperature, as shown in **Table 2.4** (Kočí *et al*., 2019). However, at low temperatures with high relative humidity, the *μ-value* decreases (Yi *et al*., 2016). This fact can be seen in **Figure 2.8**, reflecting the findings of Feng and Janssen, 2021.

Table 2.4. Water vapor transport properties of the AAC with the density of 0.30±2.5 g/cm^3 in wet-cup measurement (Kočí *et al*., 2019).

Temperature ℃	**Water vapor diffusion resistance index (*μ-value*)** unitless
5	3.37
15	4.58
25	5.03

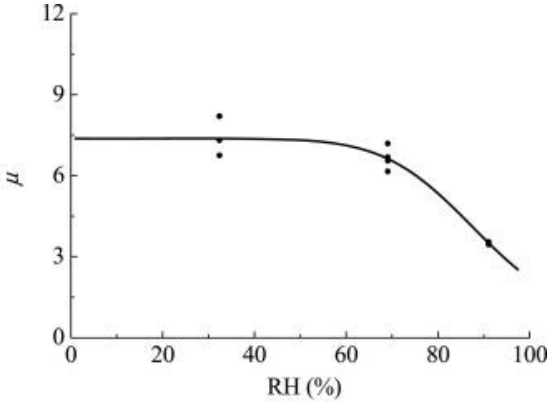

Figure 2.8. The changes in the *μ-value* relative to changes in RH (Feng and Janssen, 2021).

Jerman *et al*. (2013) conducted a detailed study on water vapor transfer of three AAC materials with different bulk densities. According to the results obtained, AAC material with a density of 0.36 g/cm^3 had the highest *μ-value* in both directions along the block (A-Direction) and across the block (B-Direction) due to the highest pore volume detected among others (**Table 2.5**).

Table 2.5. The water vapor transport parameters of the AAC materials examined in the wet cup arrangement in both directions along the block (A-Direction) and across the block (B-Direction). (Jerman *et al*., 2013).

Density Class g/cm^3	**Water vapor diffusion resistance index (*μ-value*)** unitless	
	A-Direction	**B-Direction**
0.30	2.9	2.2
0.36	3.0	3.3
0.50	2.9	3.1

Table 2.6 shows the water and gas permeability values of AAC samples in different density ranges. The similarity between water and gas permeability values of AAC indicated that aeration pores have a negligible effect in vapor permeability characteristics of AAC materials (Andolsun, 2006).

Table 2.6. The water and gas permeability values for AAC samples with varying densities and porosities (Jacobs and Mayer, 1992).

Bulk Density g/cm^3	**Porosity** %	**Water Permeability** 10^{-14}m^2	**Gas Permeability** 10^{-14}m^2
0.39	84.0	3.0±1.8	2.8±1.4
0.49	78.9	1.0±0.6	1.4±0.4
0.61	74.8	2.0±1.5	2.4±1.6
0.63	74.2	2.9±1.8	2.4±0.3

The water content in AAC comes from at least three distinct sources. AAC usually contains around 30 % water by weight of dry material after autoclaving. This water content is lost to the atmosphere after several years, as shown in **Figure 2.9** (Houst *et al*., 1983; RILEM 1993; Andolsun, 2006; Ahmed and Kamau, 2017). At high

relative humidity conditions, AAC absorbs moisture through capillary pores. When the AAC surface comes into touch with liquid water, the water is immediately absorbed through capillary suction (Ahmed and Kamau, 2017). The high water absorption properties of AAC materials are related to the high porosity and abundance of pore channels. The water is first absorbed by the capillary pores smaller than one μm in diameter and then by the large aeration pores (Qu and Zhao, 2017). Capillary pores play a significant role in water absorption, but air pores only create convoluted channels that lengthen the water flow paths (Jerman *et al*., 2013). Since the aeration pores are connected to each other only by a few mesopores, the air is probably trapped inside them. Aeration pores perform weakly in capillary water transport as they reach gravitational balance quickly. Therefore, the water absorption process can be roughly represented as the total of two mechanisms: water absorption by aeration pores that quickly finds gravity balance, and gradual capillary uptake by the capillary pores (**Figure 2.10**) (Ioannou *et al*., 2008).

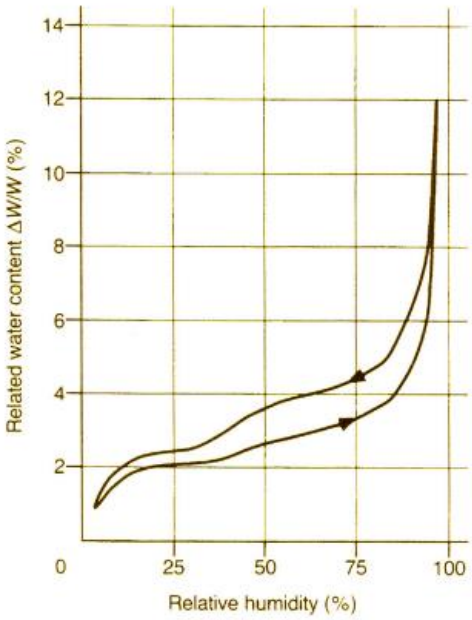

Figure 2.9. Typical Adsorption and Desorption Isotherm of AAC (Houst *et al*., 1983; RILEM, 1993; Andolsun, 2006).

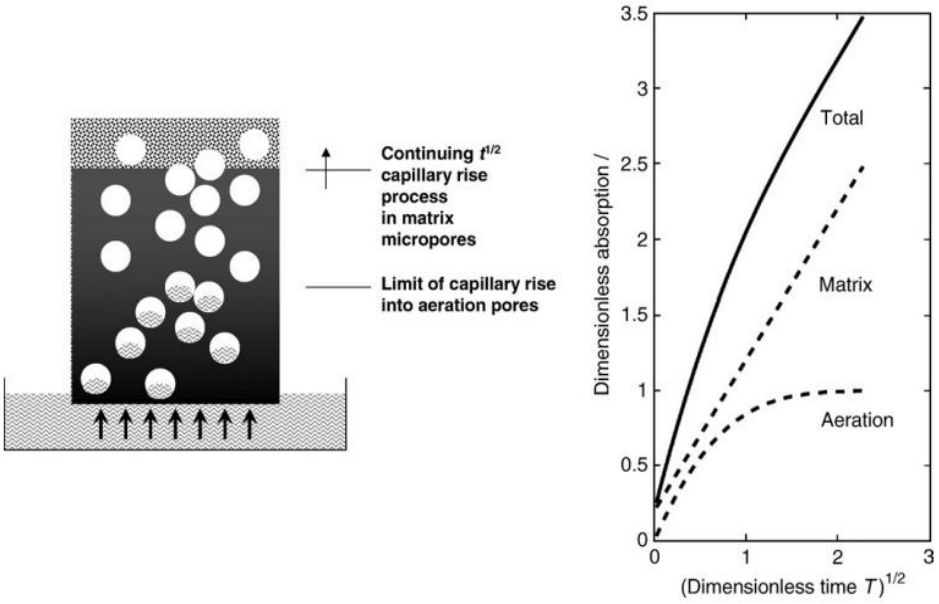

Figure 2.10. Mechanism of capillary absorption and air entrapment during the capillary absorption of water into AAC (Ioannou *et al.*, 2008).

The capillary water absorption (*A-value*) of AAC materials with different densities was investigated by Pražák and Lunk (1992). The results of their experiments determined that the capillary water absorption coefficient (*A-value*) increased as the density increased (**Table 2.7**).

T**able 2.7.** The capillary water absorption coefficient (*A-value*) of AAC samples with respect to their bulk density and porosity values (Pražák and Lunk, 1992).

Bulk Density g/cm^3	**Porosity** (%)	**Capillary Water Absorption Coefficient (*A-value*)** kg/m^{2}s$^{0.5}$
0.39	81	0.038
0.50	79	0.061
0.65	74	0.066

Andolsun (2006) examined *A-values* for AAC materials with two different densities. The results showed that the lower density AAC material had a lower *A-value* (**Table 2.8**).

Table 2.8. The capillary water absorption coefficient (*A-value*) of AAC samples with two different densities (Andolsun, 2006).

Bulk Density kg/cm^3	**Porosity** (%)	**Capillary Water Absorption Coefficient (*A-value*)** $kg/m^2s^{0.5}$
0.40	78	0.0255
0.60	69	0.0367

Jerman *et al*. (2013) studied the hygric properties of AAC materials with three different bulk densities in two directions which were along the block (Direction-A) and across the block (Direction-B). The results of the *A-values* are given in **Table 2.9** according to the density and porosity values. AAC samples with higher density values were detected to have higher *A-values*.

Table 2.9. The capillary water absorption coefficient (*A-value*) of AAC samples with respect to their bulk density and porosity values (direction A is along the block and direction B is across the block) (Jerman *et al*., 2013).

Bulk Density kg/m^3	***A-value*** **(Direction-A)** $kg/m^2s^{0.5}$	***A-value*** **(Direction-B)** $kg/m^2s^{0.5}$	**Total pore volume** g/cm^3	**Porosity** %
0.30	0.028	0.030	0.8229	85.1
0.36	0.032	0.031	0.7575	83.7
0.50	0.044	0.044	0.2825	77.6

AAC materials suffer from high drying shrinkage due to their high porosity and low aggregate content (Qu and Zhao, 2017). In drying shrinkage, the space between the pores reduces as they lose moisture, resulting in significant volumetric changes. AAC products with less than 6% moisture content experience faster drying shrinkage. The porosity and volume of micropores can also affect the drying shrinkage (Koudelka et al., 2015). Autoclaving is the other factor that can reduce the drying shrinkage of AAC materials up to 12-50% by creating a higher amount of Tobermorite (Ramamurthy and Narayanan 2000b; Qu and Zhao, 2017).

2.1.4 Physicomechanical and Mechanical Properties of AAC

The bulk density and compressive strength of AAC materials are interdependent. As the unit weight of AAC increases, the strength also increases (**Figure 2.11)** (Różycka and Pichór, 2016). RILEM (1993) categorized AAC into groups based on specific compressive strength, as indicated in **Table 2.10**. In ASTM C1693-11:2017 standard, the strength classes of AAC materials are classified according to their compressive strength values (**Table 2.11**). AAC samples may have the same density ranges with different compressive strength values due to various raw material mixtures and microstructure formation. The water/solid ratio in the raw material mixture of AAC determines the density and compressive strength. As the water to solid ratio decreases, the density increases, resulting in higher strength. Another equally significant factor affecting the compressive strength of AAC is its morphological properties. The higher amount and larger size of Tobermorite crystallinity play an important role in achieving higher compressive strength in AAC materials. The cement to sand ratio affects the formation of Tobermorite. Therefore, the cement to sand ratio should be from 0.8 to 1 to prevent decomposition and inhibition of Tobermorite. Quartz sand and coarse aggregate sand provide higher strength values to AAC when used at a maximum rate of 20% (Schober, 2005; Qu and Zhao, 2017). Moreover, pore size, shape, and distribution, and curing time, influence the compressive strength of AAC materials (Pehlivanlı *et al*., 2015).

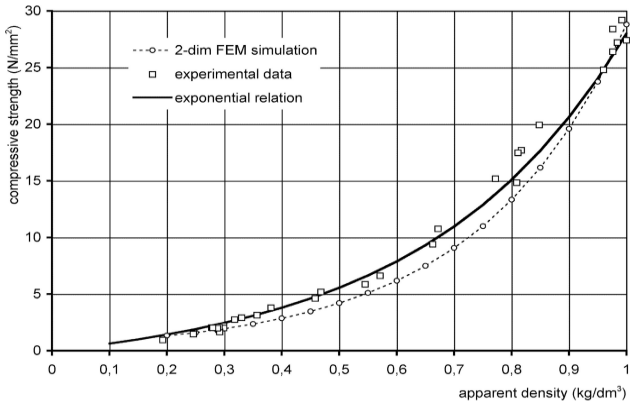

Figure 2.11. Relation between strength and apparent density of AAC over the range from 0.1 to 1 g/cm^3 (Schober, 2005).

Table 2.10. Classification of AAC According to Characteristic Compressive Strength (RILEM, 1993; p.4).

Property	Low	Medium	High
Compressive Strength (MPa)	>1.8	1.8-4.0	>4.0
Young's Modulus (MPa)	<900	900-2500	>2500
Density (g/cm^3)	0.20-0.40	0.30-0.60	0.50-1
Thermal Conductivity (dry) (W/m K)	<0.10	0.06-0.14	>0.12

Table 2.11. Physical Requirements of AAC (ASTM C1693-11:2017).

Strength Class	Compressive Strength, psi (MPa)	Nominal Dry Bulk Density, lb/ft^3 (g/cm^3)	Density Limits, lb/ft^3 (g/cm^3)	
	min		Lower Limit >	Upper Limit ≤
AAC-2	290 (2.0)	25 (0.40)	22 (0.35)	28 (0.45)
		31 (0.50)	28 (0.45)	34 (0.55)
AAC-3	435(3.0)	31 (0.50)	28 (0.45)	34 (0.55)
		37 (0.60)	34 (0.55)	41 (0.65)
AAC-4	580 (4.0)	31 (0.50)	28 (0.45)	34 (0.55)
		37 (0.60)	34 (0.55)	41 (0.65)
AAC-5	725 (5.0)	37 (0.60)	34 (0.55)	41 (0.65)
		44 (0.70)	41 (0.65)	47 (0.75)
AAC-6	870 (6.0)	37 (0.60)	35 (0.55)	41 (0.65)
		44 (0.70)	41 (0.65)	47 (0.75)

AAC materials have slightly different compressive strength values according to the rising direction of the slurry. Fission develops in the pore walls during the rising process, leading to the horizontal production of microscopic cracks that cause anisotropy in strength and other properties (Schober, 2005). As shown in **Figure 2.12**, the compressive strength perpendicular to the rising direction of AAC is slightly higher than the compressive strength from the rising direction.

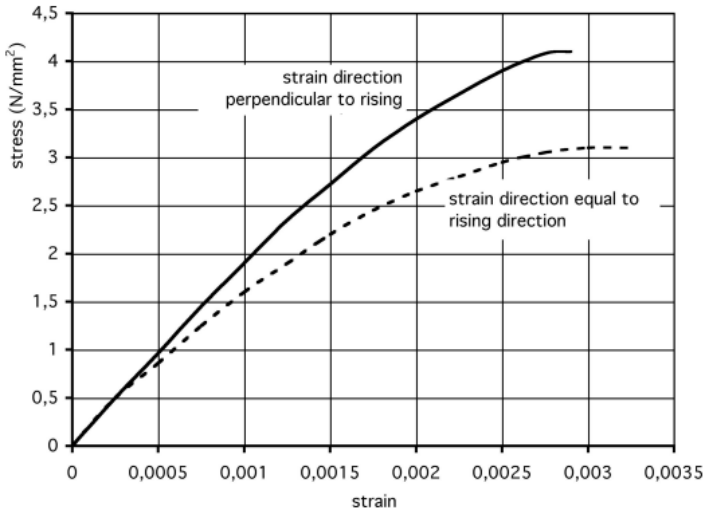

Figure 2.12. Stress strain relations of AAC cubes under compression in different directions relative to rising direction (expanding of the green cake) (Schober, 2005).

There is a correlation between moisture and compressive strength of AAC blocks (Deng *et al*., 2019). As the percentage of moisture content in AAC materials increases, the compressive strength decreases (**Table 2.12**).

Table 2.12. Basic mechanical properties of AAC (Deng *et al*., 2019).

The moisture content %	**Peak stress** MPa	**Peak strain** 10^{-3}	**Modulus of elasticity** MPa	**Residual strength** MPa
0	5.59	6.08	1133.6	2.64
5	4.47	5.57	1021.8	2.42
10	3.95	5.56	973.9	2.18
20	3.88	5.39	954.4	1.83
30	3.82	5.34	943.5	1.98
40	3.79	5.22	939.1	1.73
50	3.34	4.58	908.4	1.55
60	3.35	4.27	909.7	1.82

Modulus of elasticity (E_{mod}), as the other indicator of strength, measures the stiffness of construction material. The higher the density and compressive strength, the higher the E_{mod} values of the aerated concrete (Narayanan and Ramamurthy, 2000a). The E_{mod} values of aerated concrete are much lower than that of conventional and

lightweight concrete. AAC materials have E_{mod} values ranging from 1.0 to 8.0 GPa for densities of 0.40 to 1.2 g/cm^3 (Qu and Zhao, 2017). As the moisture content increases, the compressive strength and E_{mod} values decrease to some extent (**Table 2.12**) (Deng *et al*., 2019).

Ultrasonic pulse velocity (*UPV*), as a non-destructive technique, can be used to determine the physicomechanical properties of AAC by measuring the velocity of ultrasonic wave transfer from one point to another at a given distance (Jasiński, 2020). Factors such as porosity, pore size and distribution, admixtures, the distance between transducers, transducers positions, moisture content, and age of the material can affect the *UPV* measurement results (Ndagi *et al*., 2019). Higher density AAC materials have higher *UPV* measurements. This fact can be seen in **Table 2.13**, reflecting the findings of the study conducted by Jasiński *et al*. (2019) and Jasiński (2020).

Table 2.13. Test results for ultrasound velocity in AAC (Jasiński *et al*., 2019; Jasiński, 2020).

Range of Density (Nominal Class of Density) g/cm^3	**Mean Path Length** mm	**Range of Passing Time of Wave** µs	**Range of Ultrasound Velocity (*UPV*)** m/s
0.37 – 0.44 (0.40)	100.2	53.5 – 60.9	1647 – 1801
0.46 – 0.53 (0.50)	100.3	53.0 – 59.3	1691 – 1849
0.56 – 0.61 (0.60)	100.4	49.5 – 54.6	1841 – 1942
0.65 – 0.72 (0.70)	100.2	45.1 – 48.6	2064 – 2159

In another study, Andolsun (2006) investigated the *UPV* values for AAC materials with two different densities. **Table 2.14** summarizes the outcomes of the UPV test.

Table 2.14. The results of mechanical properties of AAC in terms of ultrasonic velocity (*UPV*) (Andolsun, 2006; Tavukçuoğlu and Grinzato, 2006).

Density kg/m^3	**Mean Path Length** mm	**UPV** m/s
0.40	50	1802-1974
0.60	50	1952-2282

The *UPV* measurement results of the AAC materials can be different in various studies due to the different raw material consumption in the manufacturing process.

2.2 Treatment Techniques to Control Hygric Properties of AAC

Both durability properties of the building materials and the exposed weathering conditions have significant impacts that have to be considered to assess the performance of exterior walls made of AAC and its complementary materials/layers. The exposure duration and intensity also affect the durability and life span of wall components. Here, moisture, resulting in dampness problems, is the most important weathering factor. It triggers some other decay factors as well, such as soluble salts. Controlling water penetration from the exposed surfaces by keeping the moisture content in the material to a certain extent (below the critical moisture content level) is one of the precautions to control the damaging effects of weathering cycles, such as wetting-drying, freezing-thawing, and salt crystallization cycles (Kus and Noberg, 1999; Kus, 2003).

AAC is a type of lightweight concrete and well-known with its higher thermal resistance and breathable characteristics compared to other lightweight concrete products, such pumice blocks. Despite of its such potentials, AAC has some well-known weaknesses, such as high water absorption in exposed conditions and penetration by capillary suction (He *et al*., 2018). Therefore, the exposed surfaces of AAC products have to be protected commonly by the plaster finishing layers which have low water permeability features. However, these finishing layers mostly hinder the high breathable characteristics of AAC layers and results in entrapped moisture problems and reduction in thermal resistivity (Andolsun, 2006; Sezemanas *et al*., 2013; Duano *et al*., 2021).

For this reason, surface coating treatment can be considered to control water penetration from the exposed surfaces of AAC and reduce the adverse impacts of weathering conditions. Instead of a plaster finishing, surface coating application can

be preferable since this treatment allows keeping the inherent porous texture of AAC for aesthetic purposes. The studies of Kus and Norberg (1999) show that water repellent coatings are promising to extend the service life of AAC surfaces. Here, special care should be given to water vapor permeability features of the surface coating material. In this regard, any surface treatment is expected to allow high breathability while controlling the water penetration to a certain extent (Andolsun, 2006; Belkharchouche and Chaker, 2016; Boukhattem *et al*., 2017).

The studies in the literature show that various protective techniques to control the high water absorption features of AAC products and their performances are examined. These protective techniques can be categorized mainly into four groups as follows:

- Treating AAC surfaces with *water-repellent surface coating* products,
- Using *lime-cement based plasters with water-repellent additives* to plaster AAC surfaces,
- Treating plastered surfaces of AAC with *water-repellent surface coating* products,
- *Manufacturing qualified AAC products* with improved mechanical and water impermeability properties.

In the case of AAC blocks treated with water-repellent surface coating products, Vejmelkova *et al*. (2009) examined the changes in capillary water absorption coefficient values (*A-value*, $kg/m^2s^{0.5}$) of AAC samples coated with five different coating bases and compared them with the uncoated control sample. AAC samples were covered with epoxy resin on all sides except the face side, which was treated with one of the coating materials, such as: Polyvinyl acetate dispersion (P), Resin dispersion with filler (F), Organic silicate face painting (S), Silicate-modified painting (K), and Flexible acrylate painting (HC). According to the results, AAC samples coated with S acted as a waterproof barrier and presented the lowest *A-value* among all treated AAC samples. The F and HC coating bases were other viable options for external protection. However, these coatings are not recommended in

areas with heavy rainfall because water penetration accelerates after three hours at washed surfaces. The P and K coatings demonstrated a slight reduction in water penetration, making them unsuitable for exterior use. The F, HC, P, and K coating bases were found to be inappropriate for long-term water protection.

In another study, Kus (2003) investigated both two techniques of using water-repellent additives in the AAC plaster mix and applying various water-repellent surface coatings to the plastered surfaces of AAC in order to control capillary water absorption coefficient (*A-value*) properties of AAC materials. AAC samples in five different systems were used in this experiment, including uncoated and untreated AAC as a control sample (O). The rest four samples were rendered with three layers of the lime-cement mixture (R), excluding one sample containing water-repellent additive in its lime-cement mixture (S2). Two of the three samples rendered with a lime-cement mixture were coated, one with styrene acrylate paint (P) and the other with silane-siloxane emulsion(S1). The lateral surfaces of all AAC samples were covered with four layers of epoxy resin, except for the exposed surface. The samples were examined in two groups and the results obtained were compared with the unexposed samples in terms of capillary water absorption coefficients (*A-value*). The first group was the artificially weathered samples exposed to UV light with water cycles for 2500 hours in an aging system called xenon-arc-type. The other was naturally aged specimens placed on a south-facing 45°C metal rack on the roof of the building in Gävle for 36 months. The results of the experiment were as follows:

— In the unexposed AAC group, treated AAC samples had a lower *A-value* than O and R samples.
— In the artificially weathered samples, a slight increase in the *A-value* was observed in S1 and S2 samples compared to their unexposed values. The highest change was detected in the P sample.
— In naturally weathered samples, samples S2 and P had higher values in *A-value* after 36 months, but sample S2 performed better.

In order to improve the performance properties of the plaster used to render the AAC blocks from the outside, Duano *et al*. (2021) conducted a study on the AAC plastering mortar containing magnesium phosphate cement (MPC) to evaluate its water retention, drying shrinkage, and compressive strength properties. MPC mortar was produced in two different series containing various doses of fly ash and cenosphere. In the first group, MPC was partially replaced by fly ash (0-30% by weight). The second group with a fixed amount of fly ash (30% by weight of MPC) contained sand replaced with different percentages of cenospheres. The water to binder ratio in all of the mixes was 0.15, with a borax addition level of 4% by weight of the magnesia. Results showed that water retention of MPC mortar was enhanced by adding fly ash content. MPC mortars without fly ash addition had 85% water retention, which increased to 97.2% with 40% fly ash substitution. The addition of 0% to 20% fly ash substitution affects the MPC mortar to improve its mechanical strength, while the fly ash content of more than 20% reduces the compressive strength, flexural strength, and bond strength. However, cenospheres addition reduced the compressive strength, flexural strength, bond strength, and water retention rate of MPC mortar. Replacement of sand with cenospheres decreased drying shrinkage and thermal conductivity due to the hollow nature of cenosphere particles. The AAC block cannot absorb water from the mortar applied on its surface since the MPC mortar hardened in a short time (30 minutes). In another study, Sezemanas *et al*. (2013) added different ratios of natural zeolite (clinoptilolite) to the AAC plaster mixture. Laboratory experiments were conducted to determine dry density, the force of plaster adhesion to AAC material, dry shrinkage, compressive strength, water vapor permeability, and capillary water absorption coefficient (*A-value*). Results determined that AAC samples with higher zeolite additive content showed higher density, compressive strength, and adhesive strength. The water vapor permeability decreases (the vapor resistance coefficient increases) as the amount of zeolite in the mixture increases. There was a slight decrease in the *A-value* with increasing zeolite content in the mixture. Calcium stearate is present in all

samples as a hydrophobic substance, which preconditions a low water absorption value.

Some studies have investigated substituting AAC raw materials with various substances to produce AAC products with higher mechanical and water impermeability properties. In this regard, Seddighi *et al*. (2021) evaluated the effect of replacing different amounts of graphene nanoparticles (GP) with cement on the mechanical and water absorption properties of the AAC specimens. AAC samples with three various nano-graphene mixtures (0.2, 0.4, 0.8% by cement weight) were compared to reference AAC sample without nano-graphene. According to the results, as the amount of nano-graphene content in the AAC raw material components increased, the compressive strength and tensile strength increased, but the modulus of elasticity, water absorption and water uptake height decreased. In another study, Pachideh and Gholhaki (2019) used pozzolanic additives such as silica fume, zeolite and granulated blast furnace slag at a rate of 7, 14 and 21% by weight of cement to improve the mechanical and water absorption properties of AAC blocks. Results determined that compressive and tensile strength of the AAC materials was enhanced due to the pozzolanic additions. AAC samples containing silica fume had the lowest water absorption followed by zeolite and granulated blast furnace slag containing specimens. Kapala and Dachowski (2016) developed chalcedony-based AAC blocks to improve physical and mechanical properties. For this purpose, AAC blocks containing different amounts of chalcedony were replaced with 10, 20, and 30% by weight of sand and gypsum content and compared with control AAC samples. According to the results, the density of AAC materials increased as the amount of chalcedony in the mixture increased. However, a slight decrease was detected in the compressive strength of AAC samples containing more than 10% chalcedony. The *A-value* decreases slightly as the amount of chalcedony increases compared to the control sample. AAC samples containing 30% chalcedony had the lowest A-value, about 16% lower than the control sample.

2.3 Standards Related to the AAC Terminology, Production, Performance, Testing and Construction

There are several international standards in the literature on AAC terminology, production (manufacturing), performance characteristics, testing, and construction. They are mainly ASTM and EN standards and listed in **Table 2.15**. Some standard focus on the production process of unreinforced and reinforced AAC masonry units summarize the raw materials characteristics, their compositions and portions in the mixture as well as manufacturing process including the autoclaving time and temperature, the wire cutting process and the final dimensions (ASTM C1660-10(2018); ASTM C1693-11(2017); EN 12602(2016), PN-89/B-06258(1989)).

Some standards (PN-89/B-06258(1989); EN 845-2:2013+A1:2016; ASTM C1694-09(2017); ASTM C1686-09(2017); ASTM C1691-21; ASTM C1692-18) explain:

— the application instructions related to some of the AAC products, such as masonry units, reinforced AAC panels and lintels, and
— the mortar bed (adhesive or jointing mortar) used to bond AAC masonry units, its ingredients with a focus on cement binder, performance testing based on splitting tensile strength.

Some standards explain the performance criteria and testing related to some of the AAC products, such as masonry units, reinforced AAC panels and lintels. Some of them specify the measurable characteristics that are used to determine basic physical, hygric, physicomechanical, and mechanical properties of AAC. These properties are defined as bulk density, water vapor permeability, water absorption, moisture sorption, moisture desorption, capillary suction, shrinkage, durability, compressive strength, shear strength, flexural strength, and thermal properties (PN-89/B-06258(1989); EN 771-4+A1:2015). On the other hand, these standards do not involve, identify or explain any numerical data related to these performance properties, except compressive strength (RILEM, 1993; ASTM C1693-11:2017; Łaskawiec *et al*., 2018). Some standards focus on testing procedures, such as testing

the compressive strength of AAC masonry units and flexural strength of masonry assemblages and reinforced AAC products (ASTM C1692-18; ASTM C1686-09(2017)). Some research discusses the mechanical properties and pore structure of AAC products in relation to their durability performances (Schober, 2005; Różycka and Pichór, 2016; Qu and Zhao, 2017). Despite of the international standards and many research on AAC products, there is still a great gap on the numerical data, especially in the standards, that define some ranges related to the performance characteristics of AAC products, their classification related to their performances, and their qualification assessment. In addition, it is observed that the data achieved by the tests in recent research and the literature are not interpreted or discussed to identify some acceptable ranges for various qualification of AAC products based on performance properties (Łaskawiec *et al*., 2018). This can be attributed to the lack of relevant information in the standards as well. Viewing all, there is necessity to improve the content of international and national standards by the studies:

— Defining the crucial performance properties,
— Determining and producing numerical data related to these performance properties,
— Identifying acceptable ranges contributing to classify and qualify the ACC products in relation to their performances.

Such research studies focusing on the above mentioned subjects are expected:

— To improve the standards content related to AAC products commonly used in the construction market, and
— To better understand the potentials and limitations of AAC products that can be guiding for the production of innovative AAC type.

Table 2.15. Lists of standards related to AAC terminology, production, performance, testing, and construction.

Standard		Content		
Code	Title	Production	Performance	Construction
EN 771-4+A1:2015	Specification for masonry units– Part4:Autoclaved aerated concrete masonry units		✓	
EN 845-2:2013+A1:2016	Specification for ancillary components for masonry– Part2:Lintels		✓	✓
EN 12602:2016	Prefabricated reinforced components of autoclaved aerated concrete	✓	✓	
EN 680:2006/Az1:2008	Determination of the drying shrinkage of autoclaved aerated concrete		✓	
PN-89/B-06258(1989)	Autoclaved Aerated Concrete	✓	✓	✓
EN 15304	Determination of the freeze-thaw resistance of autoclaved aerated concrete		✓	
BS EN 772-11:2011	Determination of water absorption of aggregate concrete, autoclaved aerated concrete, manufactured stone, and natural stone masonry units due to capillary action		✓	
EN 772-10:2011	Determination of moisture content of calcium silicate and AAC		✓	
ASTM C1693-11(2017)	Standard Specification for Autoclaved Aerated Concrete (AAC)	✓	✓	
ASTM C1694-09(2017)	Standard Specification for Reinforced Autoclaved Aerated Concrete (AAC) Elements		✓	✓
ASTM C1691-21	Standard Specification for Unreinforced Autoclaved Aerated Concrete (AAC) Masonry Units		✓	✓
ASTM C1660-10(2018)	Standard Specification for Thin-bed Mortar for Autoclaved Aerated Concrete (AAC) Masonry	✓	✓	
ASTM C1692-18	Standard Practice for Construction and Testing of Autoclaved Aerated Concrete (AAC) Masonry		✓	✓
ASTM C1686-09(2017)	Standard Practice for Installation and Testing of Reinforced Autoclaved Aerated Concrete (AAC) Units			✓
STP1356-EB	Structural Properties of Autoclaved Aerated Concrete Masonry		✓	
UNE-EN 679:2006	Determination of the compressive strength of autoclaved aerated concrete		✓	
UNE-EN 680:2006	Determination of the drying shrinkage of autoclaved aerated concrete		✓	
UNE-EN 15304:2011	Determination of the freeze-thaw resistance of autoclaved aerated concrete		✓	

2.4 Introduction on Material Properties of the Examined AAC Products

Production and use of AAC in Turkey are in the form of blocks or steel-reinforced panels. AAC blocks are classified into three main types, including wall blocks, floor blocks, and insulation blocks. AAC steel-reinforced panels include floor and roof elements, wall elements, and lintels. The AAC products that can be used in both construction and consolidation applications are masonry blocks which are classified into three main types; plain-end blocks, grooved blocks, and U-shaped blocks (www.kcs.com.tr).

In this study, laboratory analyzes were performed on four basic types of AAC materials used in Turkey including thermal insulation board (G0/150), masonry infill unit (G2/400), precast structural elements, such as wall panels, lintels (G3/500), and load-bearing masonry units (G4/600). The AAC blocks used for this study were supplied by a Turkish AAC company (KÇS Kipaş Gazbeton). As stated by the manufacturer, all AAC products are produced in accordance with TS EN 12602 Standard. AAC products examined in this study consist of quartz sand, lime, Portland cement, gypsum, aluminum powder and water as raw materials. The difference between the AAC types was the mixing ratios of these ingredients. The AAC mixtures were poured into casting molds and reached their final volume before being converted to AAC cakes at the set temperature. Afterward, AAC cakes were wire cut and autoclaved for 12 hours at 12 atm pressure and 190°C until they reached their mechanical strength (www.kcs.com.tr).

In this study, the AAC surface perpendicular to the rising direction used by the manufacturer was investigated. **Table 2.16** shows the properties of the masonry blocks and thermal insulation plate provided by the manufacturer.

Table 2.16. Manufacturer's product specifications for AAC insulation plate and masonry blocks (www.kcs.com.tr).

Material properties	**G0/150**	**G2/400**	**G3/500**	**G4/600**
Type	Insulation Panel	Infill Block	Panel	Load-bearing Block
Length (cm)	30-60	30-60	30-60	30-60
Width (cm)	5-40	5-40	5-40	5-40
Height (cm)	20-40	20-40	20-40	20-40
Dry bulk density (g/cm^3)	≤0.15	≤0.40	≤0.50	≤0.60
Compressive Strength (MPa)	≥0.4	≥2.5	≥3.5	≥5
Water Vapor Diffusion Resistance Index (*μ-value*)	7/10	5/10	5/10	5/10
Thermal conductivity W/mK	≤0.05	≤0.11	≤0.13	≤0.16

2.5 Lime Production and Carbonation Process

Calcium hydroxide ($Ca(OH)_2$), more commonly known as lime, is one of the main building materials used by civilizations for centuries (Holmes and Wingate, 1997). Lime does not exist naturally, and it should be produced. Lime goes through different stages in the production process called the 'lime cycle' (**Figure 2.13**). The first process is calcination, in which limestone as a raw material is heated in the kiln at temperatures above 900 °C until CO_2, and any water content are released and calcium oxide (CaO), known as quicklime, is obtained (Edwin 1929; Holmes and Wingate, 1997). The quicklime has a micro-crystalline structure and is highly reactive. Some of the obtained quicklime is used directly in the production of concrete blocks, but most of it is slaked in the hydration reaction, which is the second process in the lime cycle (Borsoi, 2017). In the hydration process, calcium oxide (CaO) or quicklime is mixed with water in certain proportions to produce calcium hydroxide ($Ca(OH)_2$) or lime as a dry final product. The final stage of the lime cycle is the carbonation process, in which lime reacts with CO_2 from the air to form calcium carbonate ($CaCO_3$) and release H_2O. The process has now reverted to its first state. Although

calcium carbonate, which is formed as a result of carbonation, looks chemically similar to the raw material used in the first stage, the physical properties of the two are different (Davey, 1961). As one of the stable calcium carbonate polymorphs, the formation of calcite crystals can affect the consolidation strength (Borsoi, 2017). The particle size and shape of the calcite crystals produced as a result of the carbonation reaction can be modified by carefully selecting specific parameters such as temperature and relative humidity during the reaction, reactant concentration and molar ratio (Fernandeza *et al*., 2017; Giorgi *et al*., 2010).

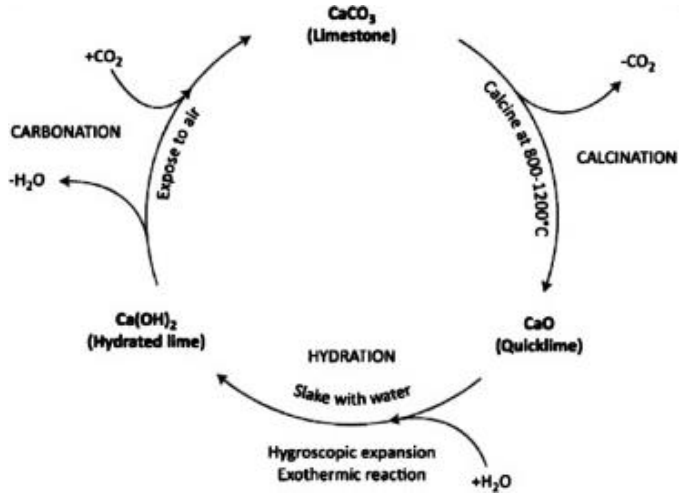

Figure 2.13. Schematic representation of the lime cycle (Billong *et al*., 2020).

During the carbonation process, the chemical reaction causes a change in the crystal structure, which increases material strength by forming a network of crystalline bonds and decreasing porosity. Therefore, some material properties, such as gas diffusivity, permeability, and capillarity are affected by changes in the microstructure of the material (Arandigoyen *et al*., 2006). The rate of carbonation reaction can be influenced by temperature and relative humidity (Revill *et al*., 2006). As temperature and relative humidity increase, the carbonation accelerates, while the solubility of CO_2 decreases. Therefore, 20 °C can be a suitable temperature for the carbonation process (Grandet, 1975). The other factor that can affect the rate of carbonation reaction is the CO_2 concentration. The higher the CO_2 concentration, the higher the carbonation rate (Moorehead, 1986; Cultrone *et al*., 2005). The amount of

CO_2 diffusion into the matrix depends on the pore structure, the water content in the pores, the capillary absorption system, and capillary condensation (Van Balen, 2005; Çizer *et al*., 2012).

2.6 Use of Nano Dispersive Calcium Hydroxide Solution for Stone Consolidation Purposes

One of the significant applications of calcium hydroxide that continues to date is in stone consolidations by building a bridge to establish the lost cohesion. Calcium hydroxide is a material compatible with stone structures as it turns into calcite crystals, which is the main raw material of the stone (Davey, 1961; Fernandeza *et al*., 2017). In the consolidation of calcareous materials, a saturated solution of calcium hydroxide and water is used. Calcium hydroxide particles are deposited in the pore structure of the material through the evaporation of the water and converted to calcite crystals after carbonation (Borsoi, 2017). However, the lower solubility of calcium hydroxide particles in water and their poor penetration into fine pores of decayed materials, calcium hydroxide nanoparticles were replaced in the water-saturated mixture (Fernandeza *et al*., 2017).

Nano calcium hydroxide ($Ca(OH)_2$) solution is composed of nanometer-sized particles of calcium hydroxide synthesized in water with other specific organic solvents, especially alcohols, to increase the solubility of the solution and the depth of penetration. The use of short-chain alcohols as dispersed media leads to kinetically stable dispersions and rapid carbonation due to the higher evaporation rate of alcohols (Giorgi *et al*., 2010). The water content is an important factor as the carbonation can only take place in the presence of both water and CO_2. Less than 5% water content in alcohol-based nano ($Ca(OH)_2$) solution can lead to deep deposition of nanoparticles in the porosity matrix. Limestone with large pores or lime-based mortars have been reported to have better in-depth consolidation but, the calcium hydroxide nanoparticles are heterogeneously dispersed at depth (Ghaffari *et al*., 2012; Borsoi, 2017). The following are the advantages of using an alcohol-based

nano calcium hydroxide solution over a saturated solution of calcium hydroxide and water traditionally used in stone consolidation:

- The ability to reach deep into damaged areas without being limited by particle size,
- Fast carbonation process due to rapid evaporation of alcohol solvent resulting in faster consolidation effect,
- Eco-friendly and free of hazardous additives (Daehne and Herm, 2013).

The calcium hydroxide nanoparticles can also be used as additives in building materials to improve mechanical and thermal properties. Another use of calcium hydroxide nanoparticles is to prevent the formation of soluble salts, which are the main decay factor of stone monuments, mortars, and murals (Fernandeza *et al*., 2017). There are different methods for applying nano dispersive calcium hydroxide ($Ca(OH)_2$) solution in the consolidation of decayed materials, including brushing, spraying, injection, dipping, systematic dripping and vacuum impregnation (D'Armada and Hirst, 2012). Spraying or brushing are commonly used for in-situ applications, while immersion and capillary absorption are frequently used in laboratory research. Generally, the nano solution used for consolidation is absorbed by capillary suction in all methods (Borsoi, 2017).

According to the results of using nano dispersive ($Ca(OH)_2$) solution in the consolidation of lime-based structures reported in the literature, it can improve compressive and flexural strength by forming crystalline bonds that slightly reduce porosity. Moreover, the treated material is more resistant to the detrimental effects of weathering, such as freezing and thawing, as well as wetting and drying. Nano-sized calcium hydroxide particles deposit in the pore structure of treated material but do not interfere with the breathing properties. Therefore, consolidation with nano-solution does not clog the surface of the material with a thick treatment layer. In terms of hygric properties, the capillary water absorption coefficient (*A-value*) of the consolidated materials is slightly reduced due to the formation of calcite crystals in

capillaries and fine pores (Daehne and Herm, 2013; Natali *et al*., 2014; Ruffolo *et al*., 2014; Rodriguez-Navarro *et al*., 2016; Badreddinea *et al*., 2020).

CHAPTER 3

MATERIAL AND METHOD

This section describes the sample preparation and the experimental methods based on the relevant standards.

Here, the preparation of untreated Autoclaved Aerated Concrete (AAC) samples, the preparation of the alcohol-based nano dispersive calcium hydroxide ($Ca(OH)_2$) solution used for the surface treatment, and the procedure of treating AAC samples with nano dispersive ($Ca(OH)_2$) solution for several laboratory experiments are described.

The untreated Autoclaved Aerated Concrete (AAC) samples are named as the control samples in the text. These samples are listed in **Table 3.1** together with their sample codes and descriptions. The treated samples correspond to the AAC samples, one side of which was treated with nano dispersive calcium hydroxide $Ca(OH)_2$ solution by capillary suction. The impact of the nano dispersive solution was examined by testing the same sample before and after treatment. The changes in performance properties of the samples before and after treatment show the performance of the nano dispersive solution.

Table 3.1. List of AAC samples examined in the study including their sample codes and descriptions.

Sample Code	AAC product type	Description
G0/150	thermal insulation board	The product with a bulk density of 150g/cm^3 in average
G2/400	masonry infill unit	The product with a bulk density of 400g/cm^3 in average
G3/500	precast structural elements, i.e. wall panels, lintels	The product with a bulk density of 500g/cm^3 in average
G4/600	load-bearing masonry units	The product with a bulk density of 600g/cm^3 in average

The laboratory tests are composed of basic physical, physicomechanical, and compositional properties analyses of both control and treated AAC samples. The list of the laboratory tests conducted on the untreated and treated AAC samples is given in **Table 3.2** together with relevant standards. The emphasis is given on the basic physical and hygric (moisture-related) performance properties of AAC samples, specifically bulk density, effective porosity, water absorption capacity, fine porosity, saturation coefficient (*S-value*), water vapor diffusion resistance index (*μ-value*), evaporation rate, critical moisture content, and capillary water absorption coefficient (*A-value*). The basic physicomechanical properties involve ultrasonic pulse velocity (*UPV*, m/s) measurements taken in direct (UPV_{DIRECT}) and indirect ($UPV_{INDIRECT}$) transmission modes. The UPV measurements were also taken in two directions, the rising direction and perpendicular to the rising direction, to better understand whether the material behaves anisotropic or not. The Modulus of Elasticity (E_{mod}, GPa) performances of AAC samples were calculated indirectly by using the measured density and UPV values in relevant equations, and the calculation method is explained in Section 3.3. The mineralogical and microstructural analyses are composed of XRD analyses of untreated and treated AAC samples and image analyses of their AAC cross-sections by optical microscopy. The formation of calcite crystals in the pores of treated AAC samples was confirmed by the XRD analyses. The magnified images of the treated and untreated surfaces belonging to the treated sample were analyzed to verify the penetration depth through the height of the treated sample.

Table 3.2. List of laboratory analyses on material properties, standards and references used to perform experimental methods.

Material Property (measurable parameter)	**Analysis Method**
Physical Properties	
Bulk Density - (ρ), g/cm³	RILEM, 1980; Teutonico, 1988
Effective Porosity - (φ), % by volume	
Fine Porosity- ($\varphi_{0.5\mu}$), % by volume	De Castro, 1978; Massa ve Amadori, 1990; Caner-Saltık *et al*., 1998; Tavukçuoğlu *et al*., 2016
Rate of fine porosity to total porosity- ($R_{0.5\mu}$), %	
Water Absorption Coefficient - (θ), % by weight	RILEM, 1980; Teutonico, 1988
Saturation coefficient- (*S-value*), unitless	RILEM, 1980
Water vapour diffusion resistance index - (μ), unitless	RILEM, 1980; Teutonico, 1988; TS EN ISO 12572; 2001; TS EN ISO 7783:2012; TS EN 1015- 19/A1:2013; ASTM E96/E96M:2016
Water vapor transmission rate - (*RT*), g/hm^2	
Equivalent air layer thickness of water vapor permeability resistance- (*SD*), m	
Water vapor permeability - (SD^{-1}), m^{-1}	
Permeance, g/sm^{2}Pa or metric perm	ASTM E96/E96M:2016
Maximum evaporation rate as a function of moisture content vapour flow rate (Drying rate) - (R_E), kg/m^{2}h	RILEM, 1980; Torraca, 1988; Massari and Massari, 1993; Garrecht, 1996; BS EN ISO 13788: 2002; Tavukçuoğlu and Grinzato, 2006
Critical moisture content - (θ_C), % by volume	
Capillary water absorption coefficient - (*A-value*), kg/m^{2}s$^{0.5}$	RILEM, 1980
Sorptivity – (*I*), mm	ASTM C1585-20
Penetrativity - (v), mm/s$^{0.5}$	Washburn, 1921
Physicomechanical Properties	
Ultrasonic pulse velocity (perpendicular to surface)- (UPV_{DIRECT}), m/s	RILEM, 1980; ASTM D 2845-08: 2017
Ultrasonic pulse velocity (parallel to surface)- ($UPV_{INDIRECT}$), m/s	
Modulus of Elasticity- (E_{mod}), GPa	
Raw Materials and Microstructural Properties	
Cross Section Analysis	Stereo Optic Microscope
X-Ray Diffraction Analysis (XRD)	X-Ray Diffractometer

3.1 AAC Sampling

In this study, four types of AAC products, including G0/150, G2/400, G3/500, and G4/600 which supplied by a Turkish company were investigated in terms of their physical, hygric, physicomechanical, mineralogical and microstructural properties using specific standards. For this purpose, AAC samples of various sizes were prepared for the laboratory analyses performed in this study. Samples with three geometric shapes were used in this research:

- Cubes with the size of 5×5×5 cm for determination of bulk density, effective porosity, water absorption capacity, saturation coefficient, fine pore porosity, as well as ultrasonic pulse velocity measurements, three parallel samples for each AAC type,
- Prisms with the size of 5×5×2.5 cm, that their 5×5 cm square base is perpendicular to the AAC rising direction, for determination of water vapor permeability, evaporation rate, and ultrasonic pulse velocity measurements, three parallel samples for each AAC type,
- Prisms with the size of 5×5×20 cm, that their 5×5 cm square base is perpendicular to the AAC rising direction, for determination of capillary water suction and ultrasonic pulse velocity measurements, three parallel samples for each AAC type (**Figure 3.1**).

Table 3.3 lists the dimensions and number of samples used in laboratory analyses for each AAC type.

Figure 3.1. AAC samples taken from the local manufacturer used for the sample preparation with dimensions of 5×5×20 cm (left), 5 ×5×2.5 cm (up), 5×5×5 cm (down) for each type (from left side, respectively; G0/150, G2/400, G3/500, and G4/600).

Table 3.3. A summary of sample sizes, number of samples, and direction examined for each laboratory analyses.

Laboratory Analyses	Sample size in cm	Number of samples				Examined Direction
		G0/150	G2/400	G3/500	G4/600	
Bulk density, Effective porosity, Water absorption capacity, Saturation coefficient, Fine pore porosity	5 × 5 × 5	3	3	3	3	Perpendicular to rising direction
Water vapor permeability	5 × 5 × 2.5	3	3	3	3	
Evaporation rate and Critical moisture content	5 × 5 × 2.5	3	3	3	3	
Capillary water suction	5 × 5 × 20	3	3	3	3	Rising direction and perpendicular to rising direction
Ultrasonic pulse velocity	5 × 5 × 2.5	3	3	3	3	
	5 × 5 × 5	3	3	3	3	
	5 × 5 × 20	3	3	3	3	

3.2 Preparation of Alcohol Dispersion of Calcium Hydroxide $Ca(OH)_2$ Nanoparticles

The nano dispersive solution was prepared by the magnetic stirring of 50 grams of calcium oxide (CaO) (Aldrich calcium oxide nanopowder 160 nm BET, 98% purity), 25 ml of distilled water, and 975 ml of ethanol for three days (Caner, 2011). In order to detect the formation of calcium hydroxide nanoparticles, 10 ml of nano dispersive solution was taken after three days and left to dry in a desiccator containing calcium chloride ($CaCl_2$) to be analyzed by XRD. Portlandite minerals, which represent calcium hydroxide particles, were detected in XRD traces (**Figure 3.2**). Calcite peaks were also found in lower amounts due to the carbonation of $Ca(OH)_2$ particles.

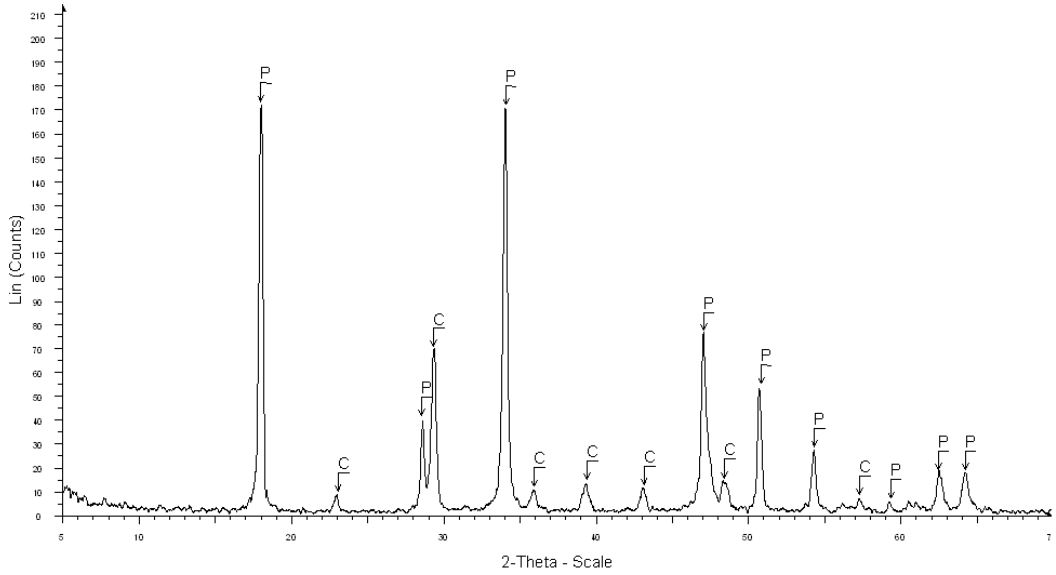

Figure 3.2. XRD traces of nano dispersive $Ca(OH)_2$ solution (P: Portlandite, C: Calcite).

3.3 Preparation of Treated AAC Samples with Nano Dispersive $Ca(OH)_2$ Solution

The treatment method consists of two stages. First, the alcohol-based nano dispersive ($Ca(OH)_2$) solution was injected only on the surface perpendicular to the rising direction of the AAC control samples (**Figure 3.3**). The nano solution penetrated into fine pores and capillaries through capillary suction. During the injection, the

nano solution used for the treatment of AAC samples was continued to be magnetically stirred to prevent the sedimentation of the calcium hydroxide nanoparticles. AAC samples of various sizes were injected with different amounts of nano solution. The amount of injected nano solution was calculated according to the sample volume and porosity values of control AAC types. The average porosity value of the four control AAC types was determined to be 80% by volume based on the porosity measurement results, implying that 20% of the AAC volume is composed of a solid matrix. For control AAC samples with the smallest size (5×5×2.5 cm), the amount of injected nano solution was calculated by multiplying sample volume with the average porosity value (20% by volume). The obtained result was rounded to 20. Therefore, 20 ml of nano solution was injected into the samples with dimensions of 5×5×2.5 cm. The amount of nano solution injected in control AAC samples with dimensions of 5×5×5 cm was doubled. However, in control AAC samples with the largest size (5×5×20 cm), the material only absorbed 80 ml nano solution by injection at one time. The injection process for each AAC sample was performed at once. The amount of nano solution injected into AAC samples of various sizes is summarized in the **Table 3.4**. For each AAC type, the same certain amount of nano dispersive solution was injected. All AAC samples were injected from the surface perpendicular to the rising direction. However, in 5×5×20 cm sized AAC samples, the samples were injected in two directions, from the rising direction and the perpendicular to the rising direction. AAC samples were then left in laboratory conditions (30±3% RH) for one day to dry.

Table 3.4. The amount of nano solution injected into AAC samples of various sizes.

Sample Size in cm (length × width × height)	**Amount of injected nano ($Ca(OH)_2$) solution in ml**
5 × 5 × 2.5	20
5 × 5 × 5	40
5 × 5 × 20	80

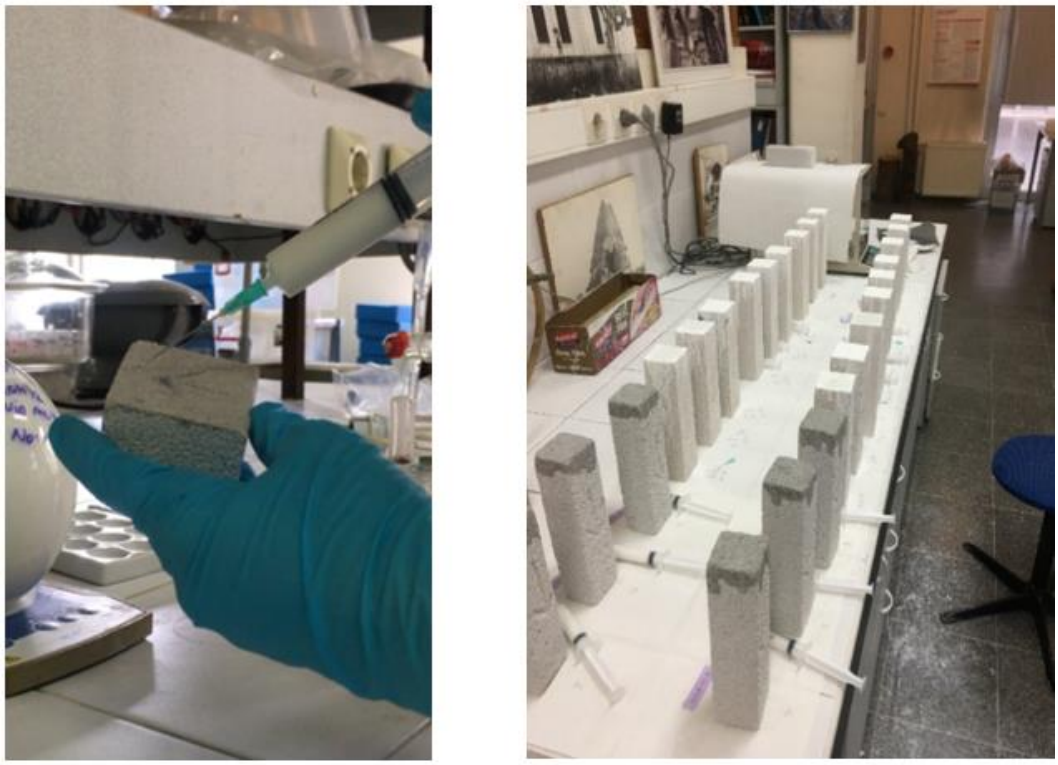

Figure 3.3. Application method of the alcohol-based nano dispersive ($Ca(OH)_2$) solution for treatment of AAC samples.

In the second stage, treated AAC samples were kept in a high relative humidity chamber (85±5%) for 28 days (**Figure 3.4**). Treated AAC samples were exposed to atmospheric carbon dioxide to perform the carbonation reaction of calcium hydroxide nanoparticles by opening the chamber for 10 to 15 minutes each day. After 28 days when the carbonation process was completed, treated AAC samples were dried in the oven at 40 ℃ for one day to achieve constant weight, and then placed in a desiccator filled with calcium chloride ($CaCl_2$) to reach ambient temperature (Caner, 2011).

Figure 3.4. Carbonation process of AAC samples in a chamber with high relative humidity.

3.4 Determination of Basic Physical and Hygric Properties

The laboratory analyses on physical and hygric properties of AAC samples include determination of bulk density (ρ), effective porosity (φ), fine porosity ($\varphi_{0.5\mu}$), ratio of fine porosity to total porosity ($R_{0.5\mu}$), water absorption capacity (θ), saturation coefficient (*S-value*), water vapor diffusion resistance index (μ-*value*), equivalent air layer thickness of water vapor permeability resistance (*SD*), water vapor transmission rate (*RT*), evaporation rate (R_E), critical moisture content (θ_C), capillary water absorption coefficient (*A-value*), sorptivity (*I*), and penetrativity (*v*). The relevant experimental methods for each laboratory analyses, terminologies, and equations are explained in further subheadings.

3.4.1 Bulk Density, Effective Porosity, Water Absorption Capacity, Saturation Coefficient, and Fine Pore Porosity

In terms of moisture-related features, the properties which define the pore structure of AAC samples, including the bulk density (ρ, g/cm^3), effective porosity (φ, % by volume), water absorption capacity (θ, % by weight), saturation coefficient (*S-value*, unitless), fine pore porosity ($\varphi_{0.5\mu m}$, % by volume), and the ratio of fine porosity to total porosity ($R_{0.5\mu m}$, as thousandth) were examined.

Three parallel AAC samples with the dimensions of 5×5×5 cm from each different AAC type in control and treated conditions were examined to have more accurate results. First, samples were left in distilled water at atmospheric pressure for 24 hours, and their weights were measured as $M_{24HOURS}$ (**Figure 3.5 a**). Afterward, samples were put in a vacuum using a HERAEUS vacuum chamber at 0.132atm (100 torr) pressure for half an hour until all fine pores were filled with water (**Figure 3.5 b**). The weights of the samples were then measured and recorded as saturated weights (M_{SAT}). Test samples were once again submerged into distilled water, and their weights were recorded as Archimedes weights (M_{ARCH}). Samples were then dried in the oven at 60 °C for 24 hours to reach the constant weight, and their measured weights were noted as dry weights (M_{DRY}). The dry weight of the test samples is recorded at this stage due to the disintegration of the samples during the saturation stage. In order to dehumidify and reach ambient temperature, samples were transferred to a desiccator filled with calcium chloride ($CaCl_2$) for three days. Afterward, test samples were placed in another dissector containing saturated barium chloride solution prepared by mixing 15 gr of barium chloride ($BaCl_2$) in 250 ml distilled water to provide 88% relative humidity condition. All dry samples were subjected to this high relative humidity condition for two weeks, and temperature and relative humidity were controlled by a data logger. The weights of the samples were recorded after two weeks as $M_{88\%}$.

All the test samples were weighed with the sensitivity of 0.0001 g to calculate bulk density, effective porosity, fine pore porosity, water absorption capacity, and saturation coefficient.

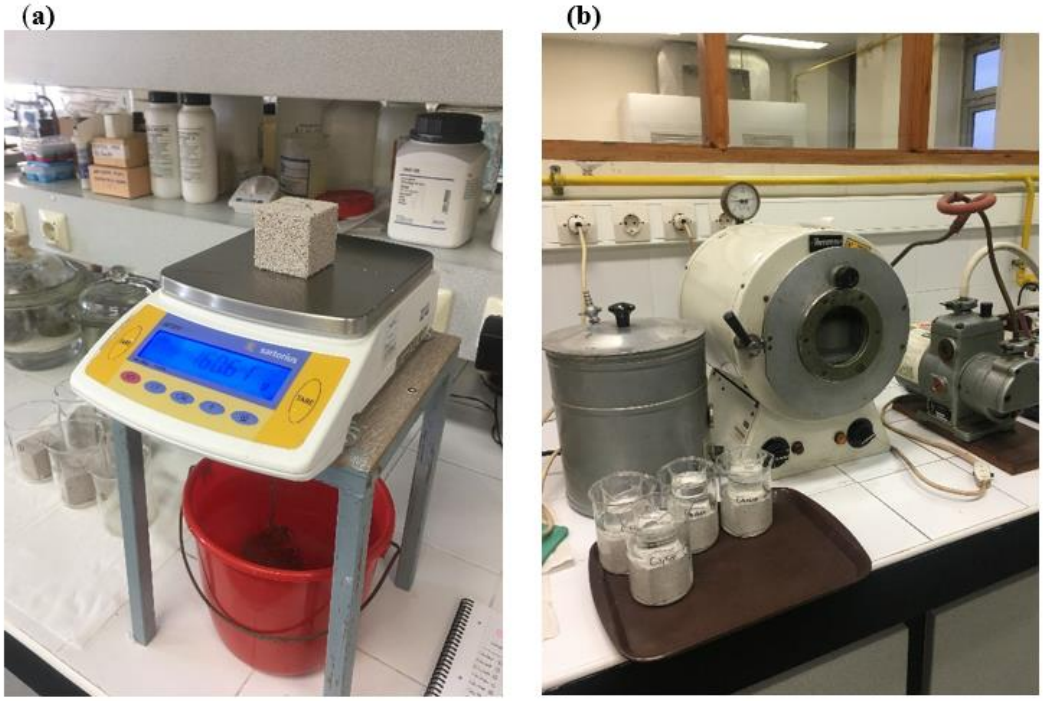

Figure 3.5. (a) Measurement of sample weights after 24 hours saturation with water; (**b)** Samples completely saturated with water in the vacuum chamber prepared for the determination of bulk density and effective porosity.

Bulk density (ρ) is defined as the ratio of the dry mass to the bulk volume of the test sample. Its definition unit is g/cm^3 and calculated by the formula presented in **Equation 3.1** (RILEM, 1980; Teutonico, 1988).

$$\rho = \frac{M_{DRY}}{M_{SAT} - M_{ARCH}}, g/cm^3 \quad (3.1)$$

Porosity (φ) is the percentage of the total volume occupied by voids or pores in a solid over the total volume. It is expressed as the percentage of volume and calculated by **Equation 3.2** (RILEM, 1980; Teutonico, 1988).

$$\varphi = \frac{M_{SAT} - M_{DRY}}{M_{SAT} - M_{ARCH}} \times 100, \% \text{ by volume} \quad (3.2)$$

Water absorption coefficient (θ) is defined as the maximum quantity of water absorbed by a porous material immersed in distilled water (Teutonico *et al.*, 1988). The water absorption capacity of a material is expressed as a percentage of the dry mass of the test sample and calculated using **Equation 3.3** (RILEM, 1980).

$$\theta = \frac{M_{SAT} - M_{DRY}}{M_{DRY}} \times 100, \text{ \% by weight} \quad \textbf{(3.3)}$$

Saturation coefficient (*S-value*) is the ratio of the volume of water absorbed by the pores after complete immersion in distilled water under atmospheric pressure to the total pore volume accessible to water (RILEM, 1980). It is a dimensionless coefficient expressed as a number in the range of 0 to 1 and calculated using **Equation 3.4**.

$$\textit{S-value} = \frac{M_{24HOURS} - M_{DRY}}{M_{SAT} - M_{DRY}}, \text{ unitless} \quad \textbf{(3.4)}$$

Fine porosity ($\varphi_{0.5\mu m}$) is the ratio of fine pores smaller than 0.5 µm to the total volume of a material. It is expressed as a percentage and calculated using **Equation 3.5** (De Castro, 1978; Massa and Amadori, 1990; Caner-Saltık *et al*., 1998; Tavukçuoğlu *et al*., 2016).

$$\varphi_{0.5\mu m} = \frac{M_{87\%} - M_{DRY}}{M_{SAT} - M_{ARCH}} \times 100, \text{ \% by volume} \quad \textbf{(3.5)}$$

The ratio of fine porosity corresponding to pores smaller than 0.5 µm to total porosity ($R_{0.5\mu m}$). It is expressed as a fraction in thousandth and calculated using the formula in **Equation 3.6** (De Castro, 1978; Massa and Amadori, 1990; Caner-Saltık *et al*., 1998; Tavukçuoğlu *et al*., 2016).

$$R_{0.5\mu m} = \frac{M_{87\%} - M_{DRY}}{M_{SAT} - M_{DRY}}, \text{ as thousandth} \quad \textbf{(3.6)}$$

3.4.2 Water Vapor Permeability

In order to analyze the water vapor permeability characteristics of both control and treated AAC samples, the measurable parameters specified in standards were

investigated to determine the equivalent air layer thickness of water vapor permeability resistance (*SD*, m), permeability (SD^{-1}, m^{-1}), water vapor diffusion resistance index (*μ-value*, unitless), water vapor transmission rate (*RT*, g/hm^2) and, permeance (metric perm) (RILEM, 1980; Teutonico, 1988; TS EN ISO 12572; 2001; TS EN ISO 7783:2012; TS EN 1015- 19/A1:2013; ASTM E96/E96M:2016).

Three parallel AAC samples with dimensions of 2.5×5×5 cm were tested for water vapor permeability from the surface perpendicular to the AAC rising direction. The thickness of each sample was measured from all four sides using a Vernier caliper, then the average of these measurements was recorded as width (S_o). Cylindrical containers were used for each test sample. The containers were filled with distilled water till 2 cm air gap was left between the water surface and the top of the container. Test samples were placed on top of the cylindrical containers. The bottom surface of test samples covering the containers along with lateral surfaces were wrapped in three layers of stretch film, then sealed with melted paraffin to avoid water vapor transmission from other sides. This process has been done on all surfaces exposed to ambient air except the top surface (**Figure 3.6 a**). All test samples were weighed to an accuracy of 0.0001 g and recorded as initial weights. Afterward, samples were placed in a desiccator filled with calcium chloride ($CaCl_2$) to ensure standard relative humidity levels (30±5% RH) (**Figure 3.6 b**). A data logger was used to monitor temperature and relative humidity levels. Samples were weighed at a certain hour each day until the weight loss per unit time of each sample remained constant.

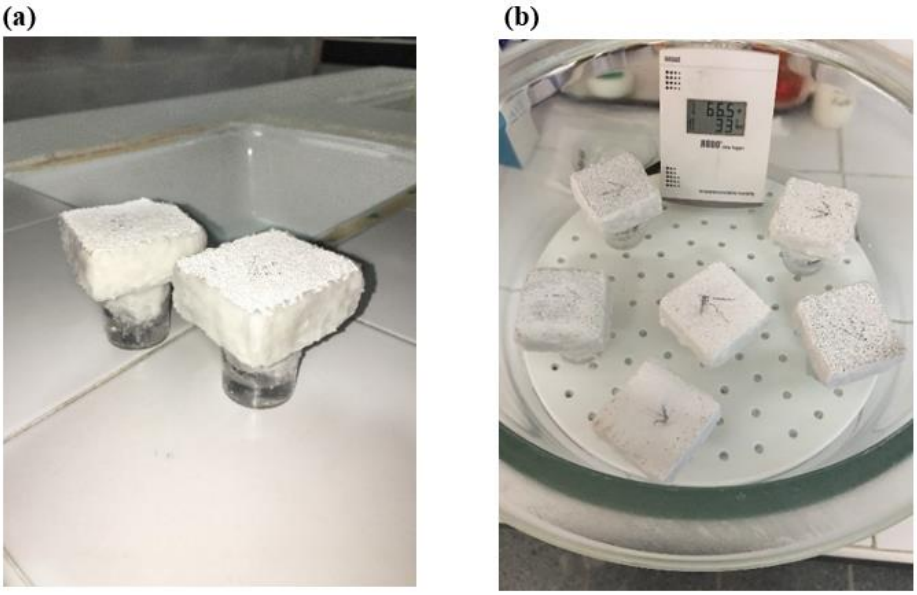

Figure 3.6. (a) Bottom surface of test samples covering the containers and lateral surfaces completely covered with paraffin; **(b)** Samples kept in a desiccator under standard relative humidity conditions for the determination of water vapor permeability characteristics.

Water vapor permeability is defined as the amount of water vapor transferred from one side of a unit thickness of flat material to the other due to the difference in vapor pressure per unit time under certain temperature and relative humidity conditions. Water vapor permeability properties are expressed as equivalent air layer thickness of water vapor permeability resistance (*SD*), and calculated using **Equation 3.7**. Permeability (SD^{-1}) is the water vapor permeability value of a material for a given thickness, calculated by dividing the *SD* value of a material by 1 (**Equation 3.8**). The water vapor resistance index (*μ-value*) is calculated using the formula in **Equation 3.9**, dividing *SD* value by the thickness of the test samples (TS EN ISO 12572, 2012; ASTM E96/E96M: 2016).

$$\boldsymbol{SD = (\Psi L \times A \times (P1 - P2)/I) - SL, m} \quad \textbf{(3.7)}$$

$$\boldsymbol{SD^{-1} = \frac{1}{SD}, m^{-1}} \quad \textbf{(3.8)}$$

$$\boldsymbol{SD = \mu S_o, unitless} \quad \textbf{(3.9)}$$

Where,

SD: Equivalent air thickness of vapor permeability resistance, (m)

SD^{-1}: Water vapor permeability value, (m^{-1})

μ: Water vapor diffusion resistance index = SD/ S_o, (unitless)

S_o: Thickness of the sample, (m)

ΨL: Constant= 6.89×10^{-6} (kg/mh (kg/m^2))

A: Area of the sample through which water vapor is evaporated, (m^2)

P1: P_o multiplied by % relative humidity in the container (kg/m^2)

P2: P_o multiplied by % relative humidity in the medium (kg/m^2)

P_o: Pressure at measured temperature (kg/m^2) (18.6466 mm Hg = 253.5016 kg/m^2 at 21ºC) (Lange and Forker, 1967)

I: Weight change in unit time, (kg/h)

SL: Thickness of air beneath the sample, (m)

Water vapor transmission rate (*RT*) is defined as the steady flow of water vapor per unit time through the unit area of a body, normal to specific parallel surfaces, under certain temperature and humidity conditions at each surface. It is expressed in g/hm^2 and calculated using **Equation 3.10** (ASTM E96/E96M: 2016; TS EN ISO 7783:2012).

$$\boldsymbol{RT = \frac{G}{t\times A}, g/hm^2} \qquad \textbf{(3.10)}$$

Where,

RT: Rate of water vapor transmission, (g/hm^2)

G: Weight change, (g)

t: Time, (h)

A: Test area (cup mouth area), (m^2)

According to TS EN ISO 7783: 2012, water vapor permeability is classified based on the values of equivalent air layer thickness of water vapor permeability resistance (*SD*, m) and water vapor transmission rate (*RT*, g/hm^2) of building materials, which are summarized in **Table 3.5**. Standard indicates that *SD* values below 0.14 m show high, *SD* values between 0.14 m and 1.4 m show medium and, *SD* values higher than 1.4 m show low permeability. In addition, the permeability is low at *RT* values less than 0.6 g/hm^2, medium at *RT* values between 0.6 and 6.0 g/hm^2, and high at *RT* values higher than 6.0 g/hm^2.

Table 3.5. The classification of water vapor permeability for building materials according to *SD* and *RT* values (TS EN ISO 7783: 2012).

Permeability Class	***SD***	***RT***
	m	g/hm^2
Low permeability	> 1.4	< 0.6
Medium permeability	0.14 – 1.4	0.6 – 6.0
High permeability	< 0.14	> 6.0

Permeance is defined as the water vapor transmission rate across a unit area of a material under a unit vapor pressure difference at the specified temperature and humidity conditions. Permeance is expressed in g/sm^{2}Pa and calculated according to the formula in **Equation 3.11.** Permeance is also expressed in "metric perm", where 1 g/Pasm² equals 1.75x10^7 metric perm (ASTM E96/E96M: 2016).

$$\boldsymbol{Permeance = \frac{RT}{\Delta P} \times \frac{1}{3600} = \frac{RT}{S \times (R_1 - R_2)} \times \frac{1}{3600}, g/sm^2Pa \text{ or (metric perm)}} \quad \textbf{(3.11)}$$

Where,

RT: Rate of water vapor transmission, (g/hm^2)

ΔP: Vapor pressure difference, Pa

S: Saturation vapor pressure at test temperature, (Pa) (3168.74 Pa at 25°C) (Wexler, 1976)

R_1: Relative humidity in the cylindrical containers, (%)

R_2: Relative humidity in the desiccator, (%)

3.4.3 Evaporation Rate and Critical Moisture Content

The drying behavior of AAC samples was investigated in terms of critical moisture content (θ_C, % by volume) and maximum evaporation rate (R_{Emax}, kg/m^{2}h) in both control and treated AAC samples.

AAC samples with dimensions of 5×5×2.5 cm were tested for evaporation rate on a surface perpendicular to the AAC rising direction before and after treatment. Three parallel samples were used to get accurate results. The test samples were initially oven-dried at 60 °C to achieve constant weight. Samples were then placed in beakers filled with distilled water for 24 hours. They were then kept under vacuum at a pressure of 0.132atm (100 torr) for 20 minutes, and their weights were recorded as M_{SAT}. All surfaces of the samples were covered with three layers of stretch film, except the top surface perpendicular to the AAC rising direction with the dimensions of 5×5 cm. Covered samples were then weighed to determine the weight of the stretch film. The wet samples were simultaneously placed on the grid sheet to be dried under almost constant conditions at 21±4 ℃ and 30±3% relative humidity (**Figure 3.7**). The weights of the samples were recorded as M_T at regular intervals of 15-30-60 minutes, 2-4-8-12-12-12 hours, and then every 24 hours until all samples were dried. The dried samples were then placed in a desiccator containing calcium chloride ($CaCl_2$) to dry completely at less than 30% RH, and their weights were recorded as M_{DRY}. All weights were measured with a sensitivity of 0.0001 grams.

The moisture content (θ, % by volume) for each sample is determined by calculating the formula in **Equation 3.12**. The amount of moisture content over time is plotted on a graph to indicate a drying curve (RILEM, 1980; Torraca, 1988; Massari and Massari, 1993; Garrecht, 1996; BS EN ISO 13788: 2002; Tavukçuoğlu and Grinzato, 2006).

$$\theta = \frac{M_T - M_{DRY}}{M_{SAT} - M_{ARCH}} \times 100, \% \qquad (3.12)$$

The evaporation rate (R_E, kg/m^{2}h) is defined as the change in mass per unit time versus the surface open to evaporation (RILEM, 1980). It is calculated according to **Equation 3.13**.

$$\boldsymbol{R_E = \frac{dM}{A \times dt}, kg/m^2h} \quad \textbf{(3.13)}$$

Where,

R_E: Evaporation rate, (kg/m^{2}h)

dM: Change in mass of the (wet) sample, (kg)

A: Surface area open to evaporation, (m^2)

t: Time interval, (h)

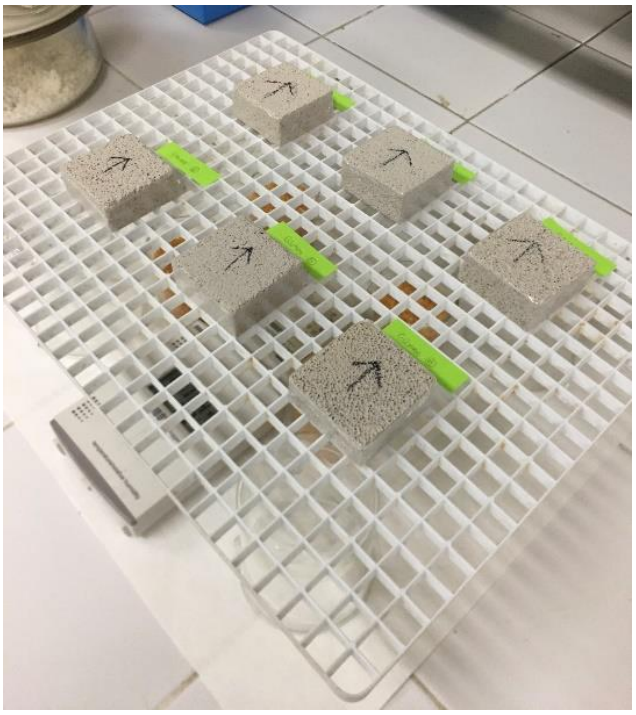

Figure 3.7. AAC samples left for drying at constant conditions of 21±4℃ and 30±3% RH.

In order to comprehend the drying behavior of the AAC types, two curves were plotted. One curve is the evaporation rate (kg/m^{2}h) over moisture content (% by volume), where the critical moisture content (θ_C, % by volume) and the maximum

evaporation rate (R_{Emax}, kg/m^{2}h) are determined. The other curve is the moisture content (% by volume) as a function of time (h) from which the critical time (t_C) is determined. For each type of AAC before and after treatment, these two curves were plotted to compare the changes in drying behavior.

The critical moisture content (θ_C) is defined as the amount of moisture content in the transition phase between the saturated and dry phases of the wet material, above which the material can be damaged. It is a physical parameter specific to each material and is required in humid areas to evaluate whether the moisture content of the material is higher or lower than θ_C value. Materials with a moisture content below θ_C level have a faster drying process and weight loss due to evaporation from the pores However, if the moisture content is above θ_C level, the slope of the evaporation rate decreases due to vapor diffusion through the capillary pores. Factors such as salt crystallization, freezing-thawing, and wetting-drying cycles can affect the moisture content. The critical time (t_C) is the time during which the rapid evaporation rate on the drying curve corresponding to the θ_C level begins to slow down (RILEM, 1980; Torraca, 1988; Massari and Massari, 1993; Garrecht, 1996; BS EN ISO 13788: 2002; Tavukçuoğlu and Grinzato, 2006).

3.4.4 Capillary Water Suction

In the context of capillary water suction characteristics of AAC types, capillary water absorption coefficient (*A-value*, kg/m^{2}s$^{0.5}$), sorptivity (*I*, mm), and penetrativity (*v*, mm/s$^{0.5}$) properties of untreated and treated samples are examined.

In this experiment, control and treated AAC samples were examined from their 5×5 cm base in two directions, rising direction and perpendicular to the rising direction. The capillary suction test was performed on three parallel AAC samples with dimensions of 5×5×20 cm. The control and treated samples were examined from their 5×5 cm treated square base surfaces. Samples were first dried in the oven at 60°C to achieve constant weight. For each AAC sample, a basin was introduced and

a piece of mesh sheet with small bases was used to prevent the direct contact of the sample bottom with water (**Figure 3.8 a**). Distilled water was added to the basin so that the sample was immersed to a height of 2 mm from the bottom surface. The water level was kept constant during the experiment by adding water when needed. The basin was covered to prevent evaporation of water and to keep the relative humidity constant (65±5%) (F**igure 3.8 b**). The weights of the samples were measured at time intervals of 1-3-5-10-15-30 minutes, 1-8-12 hours, and then every 24 hours until the sample was completely saturated with water. The height of the capillary rise in each sample was recorded at the same time as the samples were weighed. Samples were weighed with a sensitivity of 0.01 grams. The saturated samples were then dried in the oven at 60°C for one day and transferred to the desiccator filled with calcium chloride ($CaCl_2$) to reach ambient temperature. The dry weights of the samples were then recorded.

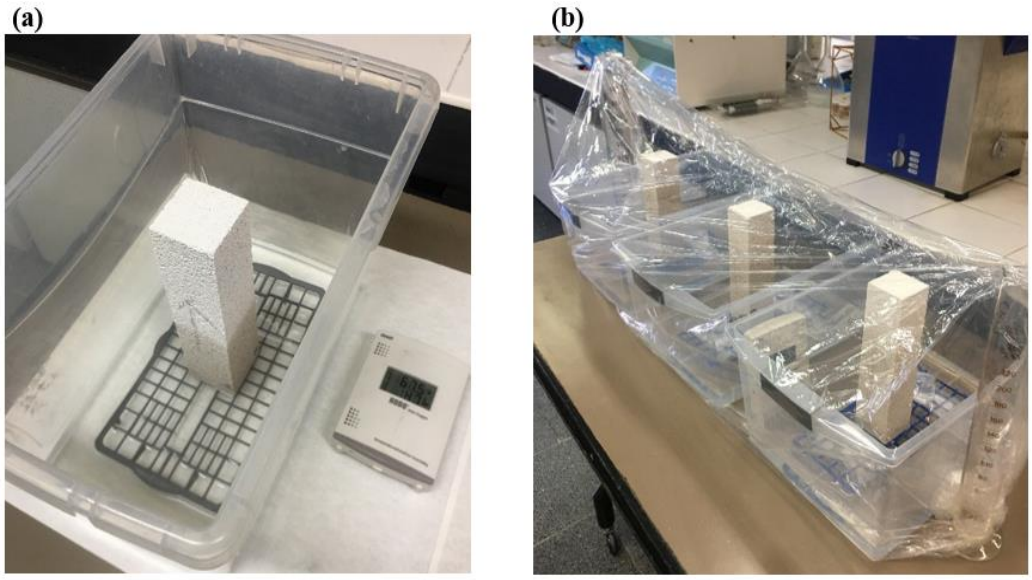

Figure 3.8. Sample placed on the mesh sheet left for capillary water suction in the basin containing distilled water; **b)** Basin covered with stretch film to prevent water from evaporation.

Capillary water absorption coefficient (*A-value*, $kg/m^2s^{0.5}$) is defined as the amount of water absorbed at a given time by the surface of a dry sample in contact with the water surface. It is calculated using **Equation 3.14**. The slope of the line in the

diagram of water absorption per unit area (kg/m^2) over square root time ($s^{0.5}$) corresponds to the capillary water absorption coefficient or *A-value* (RILEM, 1980).

$$\boldsymbol{A = m/\sqrt{t},\ kg/m^2s^{0.5}} \quad \textbf{(3.14)}$$

Where,

A: Capillary water absorption coefficient, ($kg/m^2s^{0.5}$)

m: The mass of water absorbed per unit area until time t, (kg/m^2)

t: Time passed after the capillary rise starts, (s)

Sorptivity (*I*, mm) is defined as the increase in sample mass due to capillary water absorption as a function of time when only one surface of the sample is exposed to water. It is expressed as millimeter and calculated by **Equation 3.15** (ASTM C1585-20).

$$\boldsymbol{I = \frac{m_t}{a \times b},\ mm} \quad \textbf{(3.15)}$$

Where,

I: Sorptivity, (mm)

m_t: Change in specimen mass at the time t, (g)

a: Exposed area of the specimen, (mm^2)

b: Density of the water, (g/mm^3)

Penetrativity (*v*, $mm/s^{0.5}$) is the velocity of capillary rise per unit time and it is calculated by **Equation 3.16** (Washburn, 1921).

$$\boldsymbol{v = l/t^{0.5},\ mm/s^{0.5}} \quad \textbf{(3.16)}$$

Where,

V: Penetrativity, ($mm/s^{0.5}$)

l: Level of capillary rise, (mm)

t: Time allotted, (s)

3.5 Determination of Basic Physicomechanical Properties

Physicomechanical properties of AAC samples were examined before and after treatment through ultrasonic pulse velocity (*UPV*) and modulus of elasticity (E_{mod}) tests.

As a non-destructive method, ultrasonic pulse velocity (*UPV*) can estimate the strength of the material by detecting the amount of porosity, defects, internal cracks, or degradation changes using ultrasonic waves (Naik *et al*., 2004). The *UPV* procedure is mainly the propagation velocity of a pulse of sound waves from one point to another at a certain distance. PUNDIT Plus, as a pulse generating equipment with 220 kHz transmitter and receiver probes, was used for *UPV* measurements in this study. The *UPV* measurements were performed on both control and treated AAC samples in three various dimensions of 5×5×2.5 cm, 5×5×5 cm, and 5×5×20 cm. In this study, UPV measurements were done in both direct transmission (UPV_{DIRECT}) and indirect transmission ($UPV_{INDIRECT}$). In UPV_{DIRECT} mode, the transmitter and receiver are located on opposite sides of the sample. However, in the indirect method ($UPV_{INDIRECT}$), the transducers are on the same surface and are mostly used for in-situ studies. UPV_{DIRECT} and $UPV_{INDIRECT}$ measurements were taken in 3 directions, one from the rising direction and the other two from perpendicular to the rising directions. AAC samples with different sizes were examined for *UPV* measurements as follows:

— In AAC samples with the dimensions of 5×5×2.5 cm, UPV_{DIRECT} measurements were taken from five points on the 5×5 cm surfaces, and one midpoint on the lateral surfaces (**Figure 3.9**). Their $UPV_{INDIRECT}$ measurements were taken from two cross points on the 5×5 cm surfaces and two points facing each other on the lateral surfaces (**Figure 3.10**).

— In AAC samples with the dimensions of 5×5×5 cm, UPV_{DIRECT} measurements were taken from five points on three facing surfaces (**Figure 3.11 a**), and $UPV_{INDIRECT}$ measurements were taken from two cross points on all surfaces (**Figure 3.11 b**).

— In AAC samples with the dimensions of 5×5×20 cm, UPV_{DIRECT} measurements were taken from five points on the 5×5 cm surfaces, and nine points with the intervals of 2 cm on the 5×20 cm surfaces (**Figure 3.12 a)**. Their $UPV_{INDIRECT}$ measurements were taken from two cross points on the 5×5 cm surfaces, and two points on the 5×20 cm surface, which one of them is a fixed point at a distance of 2 cm from the treated surface and the other moves from the fixed point to the maximum of 13 cm with even-numbered intervals (**Figure 3.12 b**).

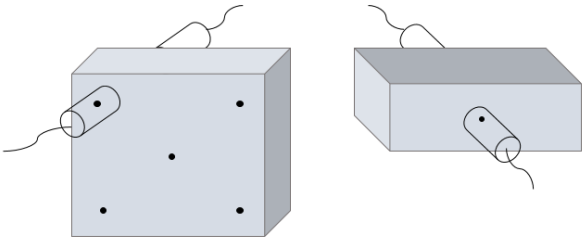

Figure 3.9. The schematic drawing showing the positions of the Transmitter probe (T) and Receiver probe (R) when ultrasonic pulse velocity measurements are carried out in direct transmission mode (UPV_{DIRECT}) from 5×5×2.5cm sized AAC samples and taken perpendicular to the rising direction (left) and parallel to the rising direction

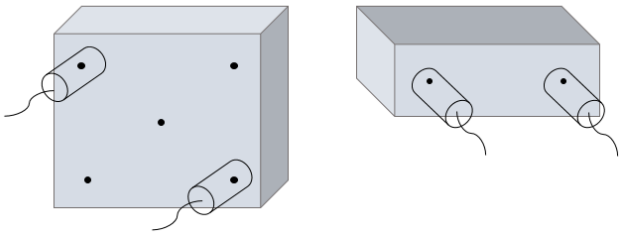

Figure 3.10. The schematic drawing showing the positions of the Transmitter probe (T) and Receiver probe (R) when ultrasonic pulse velocity measurements are carried out in indirect transmission mode ($UPV_{INDIRECT}$) from 5×5×2.5cm sized AAC samples and taken perpendicular to the rising direction (left) and parallel to the rising direction

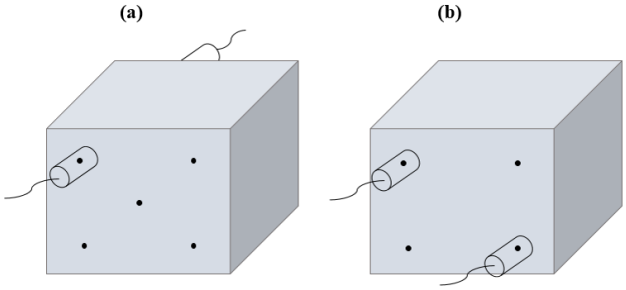

Figure 3.11. a) The schematic description of the procedure used for UPV_{DIRECT} measurements in AAC samples with the dimensions of 5×5×5 cm; **b)** The schematic description of the procedure used for $UPV_{INDIRECT}$ measurements in AAC samples with the dimensions of 5×5×5 cm.

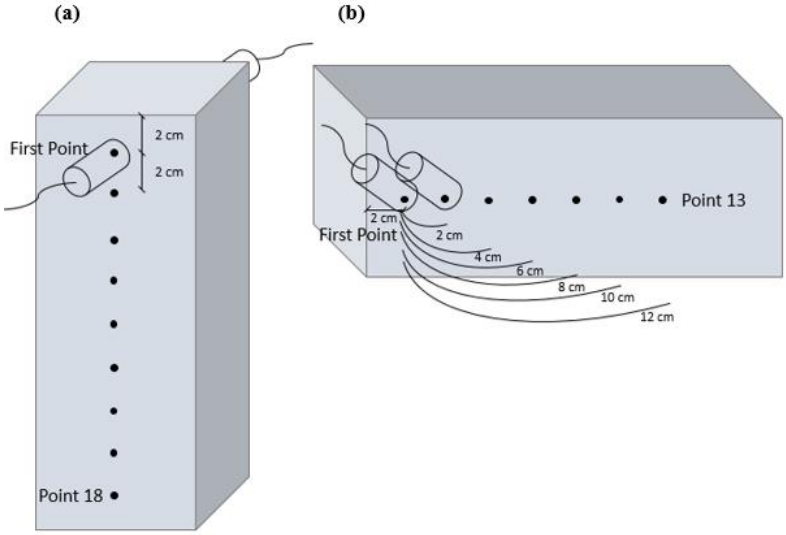

Figure 3.12. a) The schematic description of the procedure used for UPV_{DIRECT} measurements in AAC samples with the dimensions of 5×5×20 cm; **b)** The schematic description of the procedure used for $UPV_{INDIRECT}$ measurements in AAC samples with the dimensions of 5×5×20 cm.

The time taken for ultrasonic waves to pass through AAC samples of certain thickness was measured and recorded. The ultrasonic velocity of the waves is calculated by **Equation 3.17** (RILEM, 1980; ASTM D 2845-08: 2017).

$$\boldsymbol{V = \frac{d}{t}, m/s} \qquad \textbf{(3.17)}$$

Where,

V: Velocity, (m/s)

d: Distance traversed by the wave, (m)

t: Travel time, (s)

Using the direct ultrasonic pulse velocity measurements (UPV_{DIRECT}) and bulk density values of AAC samples, the modulus of elasticity (E_{mod}) values are determined. The modulus of elasticity (E_{mod}) is defined as the ratio of stress to strain, which reveals the deformation of the material when exposed to external forces. It is calculated using **Equation 3.18** (RILEM, 1980; ASTM D 2845-08: 2017).

$$\boldsymbol{E_{mod} = D.V^2 . \frac{(1+V_{dyn})(1-2V_{dyn})}{V_{dyn}}, MPa} \qquad \textbf{(3.18)}$$

Where,

E_{mod}: Modulus of elasticity, (MPa)

D: Bulk density of specimen, (kg/m^3)

V: Wave velocity, (m/s)

V_{dyn}: Poisson's ratio, (unitless)

Poisson's ratio (V_{dyn}) is defined as the ratio of lateral strain to the longitudinal reduction of the material under stress and it ranges from 0.0 to 0.5. In this study, 0.18 is taken as a value for V_{dyn} according to the literature findings (Timoshenko, 1970; Topal, 1995; Tunçoku, 2001).

3.6 Determination of Mineralogical and Microstructural Properties

In order to determine mineralogical and microstructural properties, X-ray diffraction (XRD) analyses and image analyses of cross-sections were performed on the AAC samples before and after treatment.

3.6.1 X-Ray Diffraction Analyses (XRD)

The mineral compositions of the AAC samples before and after treatment were investigated by X-Ray Diffraction (XRD) analyses in detail. The Bruker X-Ray Diffraction D8-Discover instrument was utilized for this experiment, which was

connected to a computer that controlled the setup and stored the data. CuKα radiation was used for the analyses, which was set to 40 kV and 40 mA. The XRD traces were taken in the range of 5°-70° for the 2θ values.

Each of the AAC samples was first powdered to a particle size of less than 0.125 mm, then poured into a sample holder and spread out to obtain a smooth, flat surface. The outcome is a diffraction pattern, which is a set of raw data displaying relative intensity, interplanar spaces, and location of peaks within a predetermined range.

3.6.2 Image Analyses of Cross Sections

Image analyses of cross-sections produced for each AAC type before and after treatment were performed using the Leica stereo optic microscope to determine the general texture and microstructural properties, such as the size of macropores in AAC samples before and after treatment.

Image analyses were taken from the surface perpendicular to the rising direction of the AAC samples before and after treatment with nano dispersive ($Ca(OH)_2$) solution at 7x and 40x magnifications. For cross-section image analyses, treated AAC samples were cut vertically from the treated surface using the Dewalt DW876 BandSaw 1000w machine to determine the penetration depth of the nano $Ca(OH)_2$ solution.

CHAPTER 4

RESULTS

The following sections present the results of the experiments on basic physical, hygric, physicomechanical, and compositional properties of both control and treated AAC samples in terms of bulk density (ρ), effective porosity (φ), fine pore porosity ($\varphi_{0.5\mu}$), ratio of fine pore porosity to total open porosity ($R_{0.5\mu}$), water absorption capacity (θ), saturation coefficient (*S-value*), water vapor diffusion resistance index (μ-*value*), equivalent air layer thickness of water vapor permeability resistance (*SD*), evaporation rate (R_E), critical moisture content (θ_C), capillary water absorption coefficient (*A-value*), sorptivity, penetrativity, ultrasonic pulse velocity (UPV, m/s), modulus of elasticity (E_{mod}), X-ray diffraction (XRD) analyses and image analyses of cross-sections. In addition, the performance properties of treated AAC samples with nano dispersive calcium hydroxide ($Ca(OH)_2$) solution were compared with untreated (control) AAC samples. The related results are reported under the appropriate subheading along with figures and tables.

4.1 Results of Bulk Density, Effective Porosity, Water Absorption Capacity, Saturation Coefficient, and Fine Pore Porosity Analyses

The results of bulk density, effective porosity, water absorption capacity, saturation coefficient, fine pore porosity, and ratio of fine pore porosity to total open porosity values determined for control AAC types are given in **Table 4.1 a**. While, the data presented in **Table 4.1 b** are the results of AAC types treated with nano dispersive ($Ca(OH)_2$) solution.

Table 4.1. Physical properties; bulk density (ρ), effective porosity (φ), water absorption capacity (θ), saturation coefficient (*S-value*), fine pore porosity ($\varphi_{0.5\mu}$), ratio of fine pore porosity to total open porosity ($R_{0.5\mu}$) of **(a)** control AAC types; and **(b)** AAC types treated with nano $Ca(OH)_2$ solution.

(a)

Sample Name	ρ	φ	θ	*S-value*	$\varphi_{0.5\mu}$	$R_{0.5\mu}$
	g/cm^3	% by volume	% by weight	unitless	% by volume	(as thousandth)
G0/150	0.16±0.00	90.25±0.74	561.43±5.78	0.32±0.02	0.7±0.06	8/1000
G2/400	0.42±0.01	80.57±0.70	193.12±7.03	0.45±0.04	1.02±0.03	13/1000
G3/500	0.50±0.01	77.33±0.54	154.99±3.81	0.52±0.04	1.19±0.01	15/1000
G4/600	0.62±0.01	71.78±0.97	115.33±2.54	0.64±0.01	1.40±0.04	19/1000

(b)

Sample Name	ρ	φ	θ	*S-value*	$\varphi_{0.5\mu}$	$R_{0.5\mu}$
	g/cm^3	% by volume	% by weight	unitless	% by volume	(as thousandth)
G0/150	0.18±0.00	88.51±1.15	485.33±1.18	0.30±0.02	0.52±0.04	6/1000
G2/400	0.43±0.01	74.16±0,96	178.75±6.07	0.38±0.04	0.75±0.03	10/1000
G3/500	0.51±0.01	69.86±1.58	143.57±5.27	0.42±0.05	0.87±0.06	12/1000
G4/600	0.63±0.00	62.65±1.25	101.66±2.57	0.52±0.06	1.07±0.06	17/1000

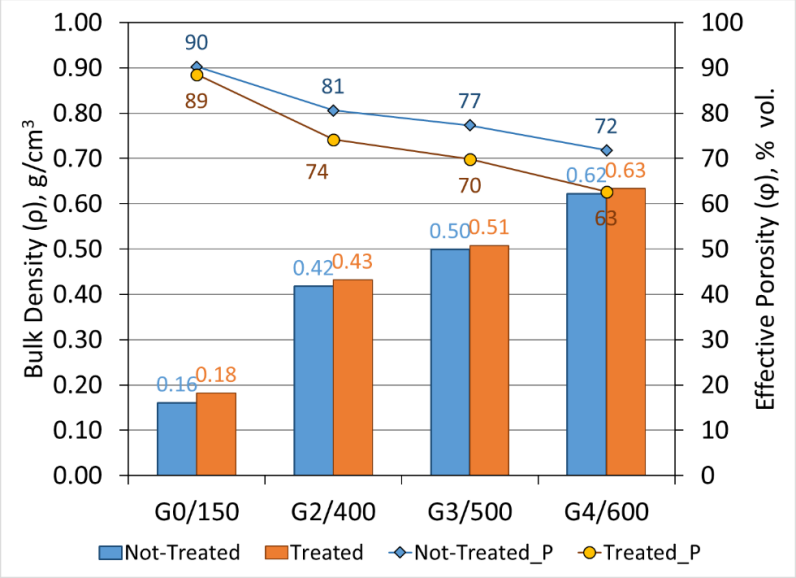

Figure 4.1. Bulk density (ρ) and effective porosity (φ) characteristics of both control and treated AAC types.

According to the results presented in **Table 4.1** and **Figure 4.1**:

— The bulk density values of G0/150, G2/400, G3/500, and G4/600 control samples were found to be 0.16±0.00, 0.42±0.01, 0.5±0.01, and 0.62±0.01 g/cm^3, respectively. Treated AAC samples were found to be slightly denser compared to the control samples. The bulk density of treated AAC samples was determined to be 0.18±0.00, 0.43±0.01, 0.51±0.01, and 0.63 g/cm^3 for G0/150, G2/400, G3/500, and G4/600, respectively.

— The results of effective porosity analysis confirmed that AAC samples are highly porous, with values of 90.25±0.74, 80.57±0.70, 77.33±0.54, and 71.78±0.97 % by volume for G0/150, G2/400, G3/500, and G4/600, respectively. However, in treated samples, effective porosity decreased to 88.51±1.15, 74.16±0.96, 69.86±1.58, and 62.65±1.25% by volume, for G0/150, G2/400, G3/500, and G4/600, respectively.

— The use of AAC blocks in building applications should be kept under control due to their high water absorption capacity. The results of the water absorption capacity verified this fact with the obtained values of 561±5.78, 193.12±7.03, 154.99±3.81, and 115.33±2.54 % by weight for G0/150, G2/400, G3/500, and G4/600 control samples, respectively. In treated AAC samples, the water absorption capacity values decreased. The highest reduction in the water absorption capacity was observed in treated G0/150, which is about 485.33±1.18 % by weight. For other treated AAC types, G2/400, G3/500, and G4/600, the reduction was detected in the range of about 11 to 15 % by weight, resulting in values of 178.75±6.07, 143.57±5.27, and 101.66±2.57 % by weight, respectively.

— The *S-value* of treated AAC samples decreased to the range of 0.30 to 0.52. The G4/600 sample has the highest *S-value* in both control and treated conditions, indicating a structure with a higher proportion of fine pores. In addition, G4/600 has the highest reduction in *S-value* among other AAC types after treatment, indicating a high proportion of fine pores were filled with nano ($Ca(OH)_2$) solution. The *S-values* of both control and treated AAC types were below the freezing-thawing resistance limit of 0.8 (BRE, 1997).

— In control AAC samples, the fine pore porosity was determined to be 0.7±0.06, 1.02±0.03, 1.19±0.01, and 1.40±0.04 % by volume for G0/150, G2/400, G3/500, and G4/600, respectively. According to the fine pore porosity values, the ratio of fine pores to total porosity (fine pores smaller than 0.5 microns in total porosity) for G0/150, G2/400, G3/500, and G4/600 was determined to be 8/1000, 13/1000, 15/1000, and 19/1000, respectively. In treated samples, these ratios decreased by about 20 to 30 % by volume, resulting in 6/1000, 10/1000, 12/1000, and 17/1000, for G0/150, G2/400, G3/500, and G4/600, respectively.

4.2 Results of Water Vapor Permeability Analyses

The results of the water vapor permeability test performed on the surface perpendicular to the rising direction of both control and treated AAC samples are presented in **Table 4.2**. Based on the *μ-value* and *SD-value* results, examined AAC types are considered highly breathable materials even after being treated with nano ($Ca(OH)_2$) solution (TS EN ISO 7783: 2012) (**Figure 4.2**).

Table 4.2. Water vapor diffusion resistance index (*μ-value*), equivalent air layer thickness of water vapor permeability resistance (*SD*), permeability (SD^{-1}), water vapor transmission rate (*RT*), and permeance of **(a)** control AAC types; and **(b)** AAC types treated with nano ($Ca(OH)_2$) solution.

(a)

Sample Name	***μ-value*** unitless	***SD*** m	***SD^{-1}*** m^{-1}	***RT*** g/hm^2	***Permeance*** metric perm
G0/150	2.25	0.050	19.95	14.99	36
G2/400	3.75	0.089	11.27	9.66	23
G3/500	3.97	0.094	10.84	9.33	22
G4/600	4.09	0.097	10.40	9.04	21

(b)

Sample Name	***μ-value*** unitless	***SD*** m	***SD^{-1}*** m^{-1}	***RT*** g/hm^2	***Permeance*** metric perm
G0/150	1.30	0.033	30.71	20.00	48
G2/400	3.11	0.078	12.87	10.29	25
G3/500	3.30	0.082	12.15	10.27	25
G4/600	3.49	0.086	11.67	9.82	24

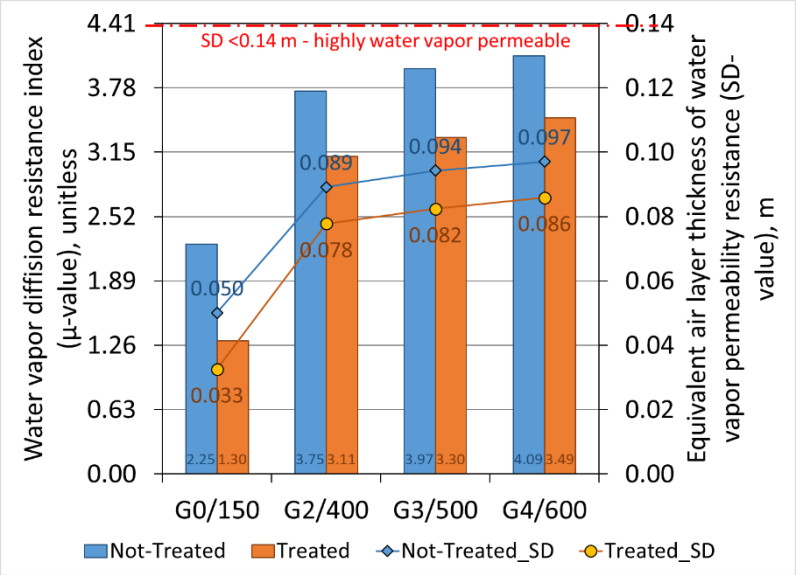

Figure 4.2. Water vapor diffusion resistance index (*μ-value)* and equivalent air layer thickness of water vapor permeability resistance (*SD*) characteristics of both control and treated AAC types.

According to the results presented in **Table 4.2** and **Figure 4.2**:

— Water vapor diffusion resistance index values (*μ-value*) of control AAC samples were determined in the range of 2.25 and 4.09. G0/150 has the lowest *μ-value* among others due to its high porosity. G2/400 and G3/500 showed close values. G4/600 was determined as the most resistant AAC type to water vapor diffusion due to its porous structure. The *μ-values* of treated G0/150, G2/400, G3/500, and G4/600 samples decreased to 1.30, 3.11, 3.30, and 3.49, respectively. The highest reduction after treatment was detected in G0/150, while G4/600 showed minor changes.

— The equivalent air layer thickness of water vapor permeability resistance (*SD*) values of control AAC samples were determined at high permeability level with values of 0.050, 0.089, 0.094, and 0.097 m for G0/150, G2/400, G3/500, and G4/600, respectively. Although, *SD-values* decreased after treatment to 0.033, 0.078, 0.082, and 0.086 m for G0/150, G2/400, G3/500, and G4/600, respectively, treated AAC samples are still highly permeable.

— In control AAC samples, permeability (SD^{-1}) values for G2/400, G3/500, and G4/600 were found to be 11.27, 10.84, and 10.40 m^{-1}. G0/150 has the highest permeability value of 19.95 m^{-1}. In treated AAC samples, permeability values increased to 30.71, 12.87, 12.15, and 11.67 m^{-1} for G0/150, G2/400, G3/500, and G4/600, respectively.

— Water vapor transmission rate (*RT*) values of both control and treated AAC types were found to be higher than 6 g/hm^2, which means they are highly permeable. In treated G2/400, G3/500 and G4/600 samples, *RT-values* increased slightly to 10.29, 10.27, and 9.82 g/hm^2, respectively. However, a significant increase in *RT-value* was observed in G0/150 sample after treatment.

— In treated AAC samples, permeance values slightly increased to 48, 25, 25, and 24 metric perm for G0,150, G2/400, G3/500, and G4/600, respectively. The treated G0/150 showed the highest increase in the permeance value.

4.3 Results of Evaporation Rate and Critical Moisture Content Analyses

The data on bulk density, effective porosity, maximum evaporation rate, critical moisture content, critical moisture content to porosity ratio, and critical drying time are summarized in **Table 4.3**. The drying curves displaying moisture content as a function of time for both control and treated AAC types are given in **Figure 4.3**. Additionally, the evaporation rate over moisture content as a drying rate curves for both control and treated AAC types are shown in **Figure 4.4**.

According to the results:

— The point at which the drying rate decreases and becomes most consistent determines the critical moisture content (θ_C) (**Figure 4.4**). The θ_C*-values* of the control AAC types were determined to be in the range of 24 and 26 % by volume, corresponding to 1/3 of the effective porosity of the samples. In treated AAC samples, the θ_C*-values* increased to the range of 27 to 45 % by volume, approaching half of the effective porosity of the samples. The G4/600 sample has the lowest θ_C-

value in both control and treated conditions. The highest increase of about 30% in θ_C-*value* was detected in G0/150 sample after treatment.

— The ratio of critical moisture content to porosity (θ_C/φ) refers to the percentage of water content in the pore structure, above which water is transported throughout the material by capillary pores. In control AAC types, the ratio of θ_C/φ was found to be in the range of 31 to 42 %, implying that if more than about 40% of the total porosity in AAC types was filled with water, samples would be more susceptible to weathering conditions. However, in treated AAC samples the ratio of θ_C/φ increased, which means that due to the deposition of nanoparticles in pores more water is required to initiate the water transfer from the capillary pores. Therefore, treated AAC samples were found to be less susceptible to deterioration cycles than control samples.

— According to the **Figure 4.3**, the counter point of the critical moisture content (θ_C), where the slop of the line decreases, determines the time critical (t_C). The t_C-*values* of the control G2/400, G3/500, and G4/600 samples were determined as 72 hours, except for the G0/150, which was 96 hours. In treated samples, the t_C-*value* reduced to 48 hours for G0/150, G3/500, and G4/600 and to 36 hours for G2/400.

— The maximum evaporation rate (R_{Emax}) values of control AAC types were determined to be in the range of 0.1253 and 0.1451 kg/m^{2}h. The control G2/400 sample has the highest R_{Emax}-*value*, while control G0/150 sample has the lowest R_{Emax} *value*. After treatment, the R_{Emax}-*values* increased to the range of 0.1806 to 0.2066 kg/m^{2}h.

Table 4.3. Bulk density (ρ), effective porosity (φ), maximum evaporation rate (R_{Emax}), critical moisture content (θ_C), the ratio of critical moisture content to porosity (θ_C/φ) and critical time (t_C) of **(a)** control AAC types; and **(b)** AAC types treated with nano ($Ca(OH)_2$) solution.

(a)

Sample Name	ρ	φ	R_{Emax}	θ_C	θ_C/φ	t_C
	g/cm^3	% by volume	kg/m^{2}h	% by volume	%	h
G0/150	0.16	90.25	0.1253	31.35	35	96
G2/400	0.42	80.57	0.1451	34.24	42	72
G3/500	0.50	77.33	0.1383	24.07	31	72
G4/600	0.62	71.78	0.1334	23.45	33	72

(b)

Sample Name	ρ	φ	R_{Emax}	θ_C	θ_C / φ	t_C
	g/cm^3	% by volume	kg/m^{2}h	% by volume	%	h
G0/150	0.18	88.51	0.1893	44.52	50	48
G2/400	0.43	74.16	0.2066	42.03	57	36
G3/500	0.51	69.86	0.1816	28.45	41	48
G4/600	0.63	62.65	0.1806	27.13	43	48

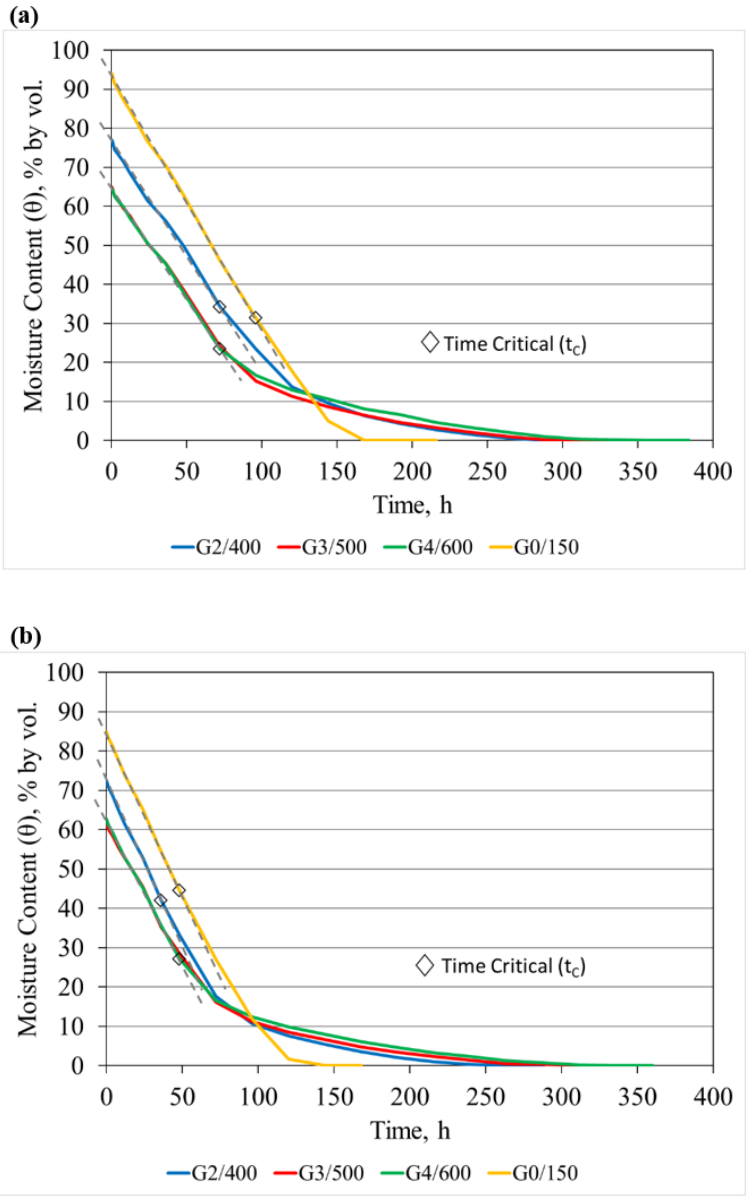

Figure 4.3. The drying curves showing moisture content (θ, % by vol.) versus time (h) of **(a)** control AAC types; and **(b)** AAC types treated with nano ($Ca(OH)_2$) solution.

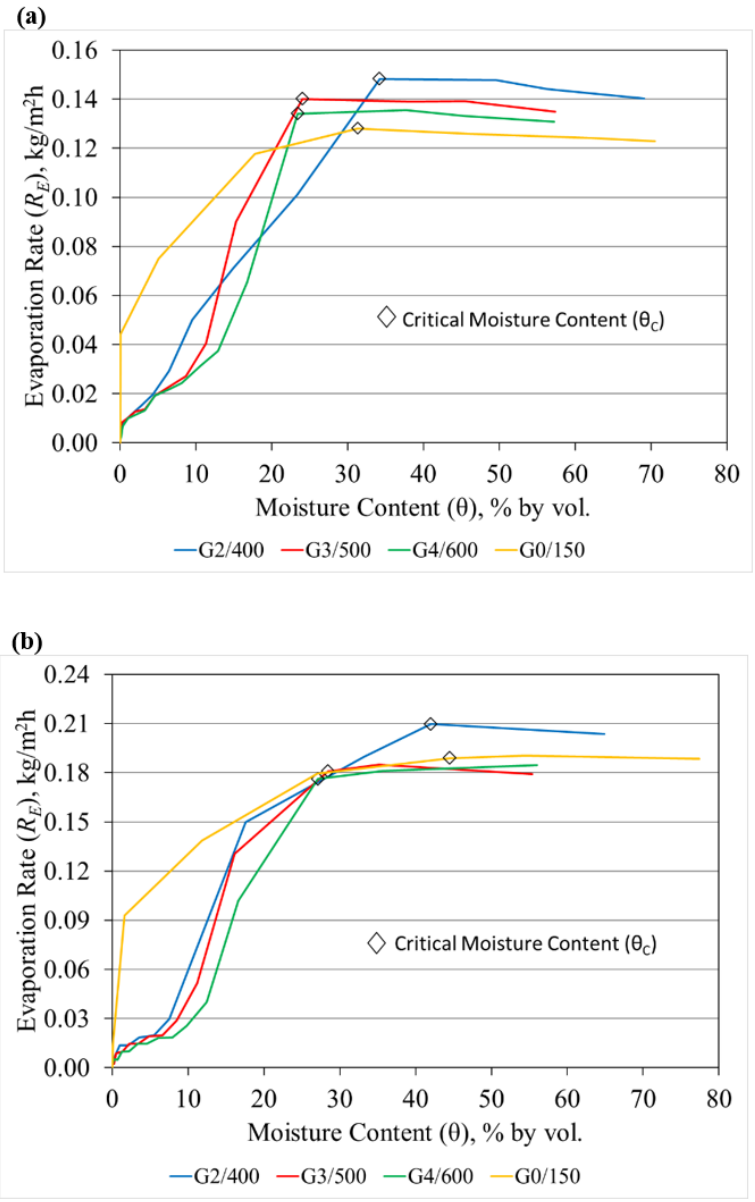

Figure 4.4. The drying rate curves showing evaporation rate (kg/m^{2}h) versus moisture content (% by volume) of **(a)** control AAC types; and **(b)** AAC types treated with nano ($Ca(OH)_2$) solution.

4.4 Results of Capillary Water Suction Properties Analyses

The results of the capillary water suction test performed in rising direction and perpendicular to the rising direction of AAC samples before and after treatment with ($Ca(OH)_2$) solution are given in **Table 4.3** and **Table 4.4**. The capillary water

absorption coefficient (*A-value*) and penetrativity behaviors of AAC samples before and after treatment are presented in **Figure 4.5**, **Figure 4.6, Figure 4.7,** and **Figure 4.8**. Results are summarized below.

— In perpendicular to the rising direction, capillary water absorption coefficients (*A-value*) of control AAC samples were determined in the range of 0.0523 and 0.1225 $kg/m^2s^{0.5}$. The sorptivity values of control G0/150, G2/400, G3/500, and G4/600 samples were found to be 0.0052, 0.0067, 0.0070, and 0.0123 mm, respectively. The penetrativity values of control AAC samples were determined to be varying in a range of 0.20 and 0.35 $mm/s^{0.5}$. G4/600 has the highest *A-value* among other AAC types and the highest penetrativity was detected in G0/150 sample (**Figure 4.5** and **Figure 4.7**). After being treated with nano ($Ca(OH)_2$) solution, the *A-values* of AAC samples decreased to the range of 0.0506 and 0.1035 $kg/m^2s^{0.5}$. The sorptivity of treated G0/150, G2/400, G3/500, and G4/600 samples slightly decreased to 0.0051, 0.0059, 0.0057, and 0.0104 mm, respectively. The penetrativity of AAC samples slightly decreased to the range to 0.18 and 0.33 $mm/s^{0.5}$ due to the penetration of $Ca(OH)_2$ nanoparticles into the pore structure of AAC samples. The highest reduction was determined in G4/600 after treatment (**Figure 4.7 b**). The G2/400 and G3/500 samples showed similar behaviors in *A-value* and penetrativity values before and after treatment.

— In rising direction, capillary water absorption coefficients (*A-value*) of control G0/150, G2/400, G3/500, and G4/600 samples were found to be 0.0535, 0.0583, 0.0596, and 0.0854 $kg/m^2s^{0.5}$, respectively. The sorptivity values of control AAC samples were determined in the range of 0.0053 and 0.0085 mm. The penetrativity values of control AAC samples were determined to be varying in a range of 0.19 and 0.36 $mm/s^{0.5}$. G4/600 has the highest *A-value* among other AAC types and the highest penetrativity was detected in G0/150 sample (**Figure 4.6** and **Figure 4.8**). The nano dispersive ($Ca(OH)_2$) treatment applied on the surface of the rising direction increased the *A-value* of G2/400 and G4/600 samples. The *A-value* of G0/150 was found to be slightly decreased, while the *A-value* of G3/500

remained the same. The same changes were also determined in sorptivity and penetrativity values after treatment (**Figure 4.8 b**).

Table 4.4. Results showing the capillary water absorption coefficient (*A-value*), sorptivity (*I*), and penetrativity (*v*) of the surface perpendicular to the rising direction; **(a)** control AAC types; and **(b)** AAC types treated with nano ($Ca(OH)_2$) solution.

(a)

Sample Name	*A-value*	*I*	*v*
	$kg/m^2s^{0.5}$	mm	$mm/s^{0.5}$
G0/150	0.0523	0.0052	0.35
G2/400	0.0675	0.0067	0.23
G3/500	0.0701	0.0070	0.20
G4/600	0.1225	0.0123	0.31

(b)

Sample Name	*A-value*	*I*	*v*
	$kg/m^2s^{0.5}$	mm	$mm/s^{0.5}$
G0/150	0.0506	0.0051	0.33
G2/400	0.0589	0.0059	0.20
G3/500	0.0572	0.0057	0.18
G4/600	0.1035	0.0104	0.27

Table 4.5. Results showing the capillary water absorption coefficient (*A-value*), sorptivity (*I*), and penetrativity (*v*) of the rising direction surface; **(a)** control AAC types; and **(b)** AAC types treated with nano ($Ca(OH)_2$) solution.

(a)

Sample Name	*A-value*	*I*	*v*
	$kg/m^2s^{0.5}$	mm	$mm/s^{0.5}$
G0/150	0.0535	0.0053	0.36
G2/400	0.0583	0.0058	0.21
G3/500	0.0596	0.0060	0.19
G4/600	0.0854	0.0085	0.23

(b)

Sample Name	*A-value*	*I*	*v*
	$kg/m^2s^{0.5}$	mm	$mm/s^{0.5}$
G0/150	0.0510	0.0051	0.33
G2/400	0.0663	0.0066	0.23
G3/500	0.0593	0.0059	0.19
G4/600	0.0892	0.0089	0.24

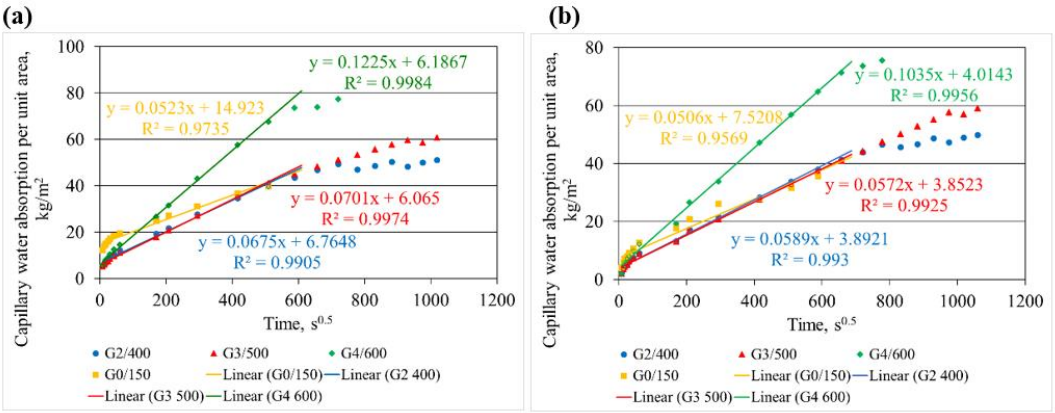

Figure 4.5. The capillary water absorption coefficients (*A-value*) of the surface perpendicular to the rising direction; **(a)** control AAC types; and **(b)** AAC types treated with nano ($Ca(OH)_2$) solution.

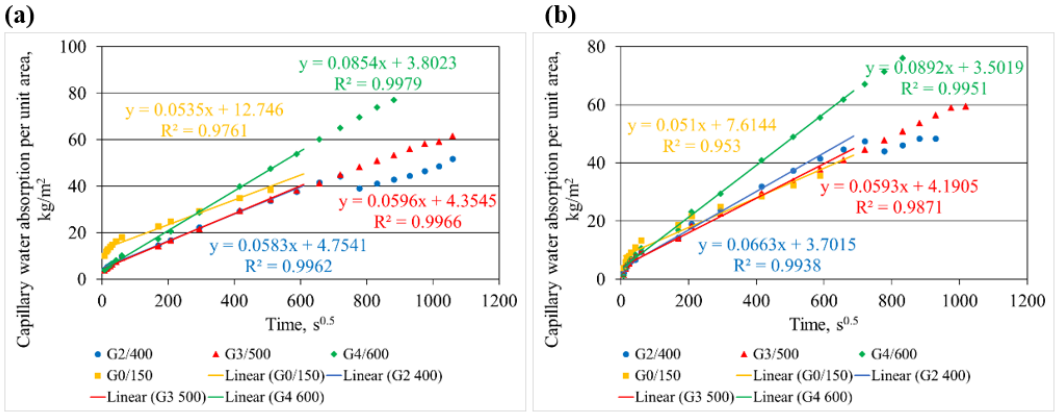

Figure 4.6. The capillary water absorption coefficients (*A-value*) of the rising direction surface; **(a)** control AAC types; and **(b)** AAC types treated with nano ($Ca(OH)_2$) solution.

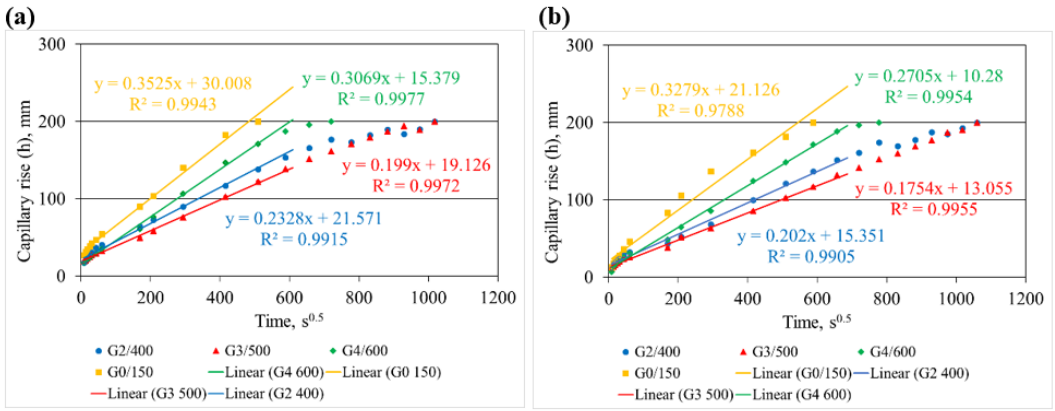

Figure 4.7. The penetrativity of the surface perpendicular to the rising direction; **(a)** control AAC types; and **(b)** AAC types treated with nano ($Ca(OH)_2$) solution.

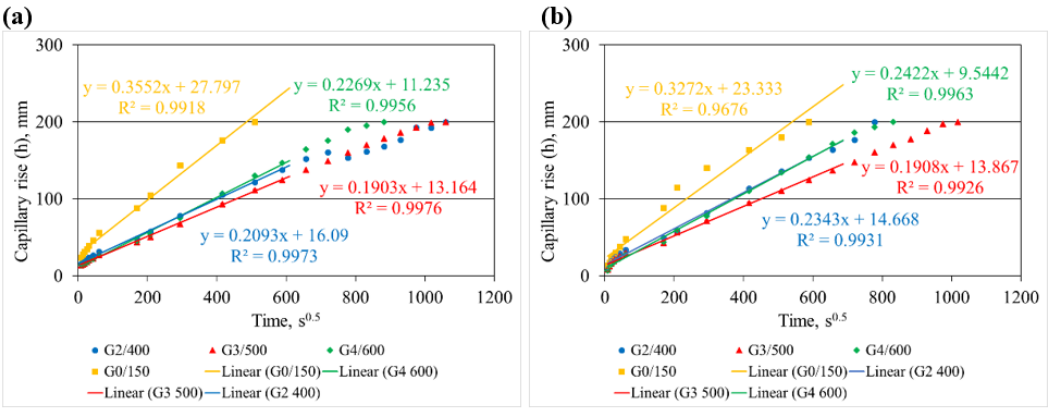

Figure 4.8. The penetrativity of the rising direction surface; **(a)** control AAC types; and **(b)** AAC types treated with nano ($Ca(OH)_2$) solution.

The achieved data showed that the *A-values* of AAC products in the rising direction are slightly lower than the *A-values* perpendicular to the rising direction, except G0/150 product (**Figure 4.9**). The *A-values* in the rising direction of the G2/400 and G3/500 are 14-15% less than the A-values perpendicular to the rising direction. The capillary water absorption behavior of the G4/600 product differs from the others. The *A-value* of G4/600 in the rising direction is noticeably lower than its *A-value* perpendicular to the rising direction with a difference of 30%. That signals that G4/600 products exhibit anisotropic behavior in capillary suction characteristics depending on rising direction.

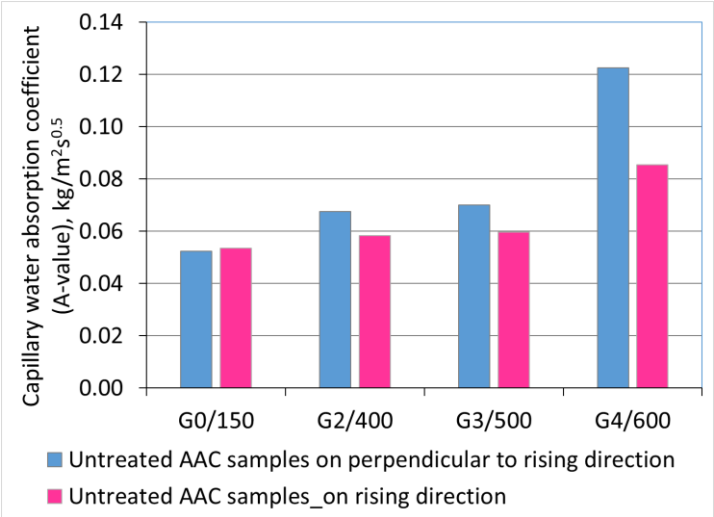

Figure 4.9. A-value of untreated (control) AAC types in perpendicular to the rising direction and rising direction.

4.5 Results of Basic Physiocomechanical Properties Analyses

The physicomechanical properties of AAC samples were determined in terms of ultrasonic pulse velocity (*UPV*) and modulus of elasticity (E_{mod}) values.

Physicomechanical properties of AAC samples before and after treatment are summarized in **Table 4.7**. These tables include ultrasonic pulse velocity values taken in direct (UPV_{DIRECT}) and indirect ($UPV_{INDIRECT}$) transmission modes and the calculated modulus of elasticity (Emod) values. Among four AAC types, transit time readings could not be achieved for the G0/150 sample. this can be attributed to the discontinuities in the highly porous feature of G0/150. Transit time readings cannot be achieved in case ultrasonic waves cannot find a path to pass through the solid matrix. At the same time, it is observed that when the transmitter and receiver probes were in contact with the G0/150 surface and light pressure was applied, the surface of the sample was deformed by collapsing inward. Therefore, UPV_{DIRECT} and $UPV_{INDIRECT}$ measurements were carried out on G2/400, G3/500, and G4/600 samples before and after treatment.

The UPV_{DIRECT} data taken both on the rising direction and perpendicular to the rising direction are similar (**Table 4.6**). The $UPV_{INDIRECT}$ data taken from the surfaces in the rising direction and perpendicular to the rising direction are similar (**Table 4.6**).

Table 4.6. The UPV_{DIRECT} and $UPV_{INDIRECT}$ data taken from AAC samples in all directions, specifically the rising direction and perpendicular to the rising direction.

Sample Name	UPV_{DIRECT} (m/s)			$UPV_{INDIRECT}$ (m/s)		
	Rising direction	Perpendicular to rising direction	Perpendicular to rising direction	Rising direction	Perpendicular to rising direction	Perpendicular to rising direction
G2/400	1480	1438	1480	360	347	430
G3/500	1570	1548	1575	380	380	479
G4/600	1720	1760	1805	410	408	555

The UPV_{DIRECT} values of G2/400 samples were found to be varying in the range of 1455 and 1500 m/s, with an average of 1461±16 m/s. The UPV_{DIRECT} values of G3/500 samples were found to be varying in the range of 1515 and 1580 m/s, with an average of 1559±9 m/s. The UPV_{DIRECT} values of G4/600 samples were found to be varying in the range of 1700 and 1850 m/s, with an average of 1759±15 m/s. After treatment, the UPV_{DIRECT} values increased to 1663±19 m/s for G2/400 samples. In G3/500 samples, the UPV_{DIRECT} values increased following treatment to 1879±24 m/s. In treated G4/600 samples, the UPV_{DIRECT} values increased to the 2242±44 m/s. The highest UPV_{Direct} values was detected in G4/600 both in control and treated conditions (**Table 4.7** and **Figure 4.10**).

— The $UPV_{INDIRECT}$ values of G2/400 samples were determined as 508±28 m/s. The $UPV_{INDIRECT}$ values of G3/500 samples were determined as 564±17 m/s. The $UPV_{INDIRECT}$ values of G4/600 samples were found to be 648±93 m/s. After treatment, the $UPV_{INDIRECT}$ values increased to 629±24 m/s for G2/400 samples. In treated G3/500 samples, the $UPV_{INDIRECT}$ values increased to 691±8 m/s. In treated G4/600 samples, the $UPV_{INDIRECT}$ values increased to 888±20 m/s.

— The E_{mod} values of G2/400 samples were found to 0.83±0.02 GPa. The E_{mod} values of G3/500 samples were found to be 1.12±0.02 GPa. The E_{mod} values of G4/600 samples were found to be 1.81±0.05 GPa. After treatment, the E_{mod} values increased to 1.07±0.04 GPa for G2/400 samples. In G3/500 samples, the E_{mod} values increased following treatment to 1.63±0.07 GPa. In treated G4/600 samples, the E_{mod} values increased to 2.04±1.2 GPa. The highest E_{mod} values was detected in G4/600 both in control and treated conditions (**Figure 4.10**).

Table 4.7. Bulk density (ρ), UPV_{DIRECT}, $UPV_{INDIRECT}$, $UPV_{INDIRECT}$ / UPV_{DIRECT}, and E_{mod} values were determined for **(a)** control AAC types; and **(b)** AAC types treated with nano ($Ca(OH)_2$) solution.

(a)

Sample Name	ρ	UPV_{DIRECT}	$UPV_{INDIRECT}$	$UPV_{INDIRECT}$ / UPV_{DIRECT}	E_{mod}
	g/cm^3	m/s	m/s	ratio	GPa
G2/400	0.42±0.01	1461 ±16	508±28	0.34-0.35	0.83 ±0.02
G3/500	0.50±0.01	1559 ±9	564±17	0.36-0.37	1.12 ±0.02
G4/600	0.62±0.01	1759±15	648±93	0.35-0.37	1.81 ±0.05

(b)

Sample Name	ρ	UPV_{DIRECT}	$UPV_{INDIRECT}$	$UPV_{INDIRECT}$ / UPV_{DIRECT}	E_{mod}
	g/cm^3	m/s	m/s	ratio	GPa
G2/400	0.43±0.01	1663 ±19	629 ±24	0.38	1.07 ±0.04
G3/500	0.51±0.01	1879 ±24	691 ±8	0.37	1.63 ±0.07
G4/600	0.63±0.00	2242 ±44	888 ±20	0.43	2.04 ±1.2

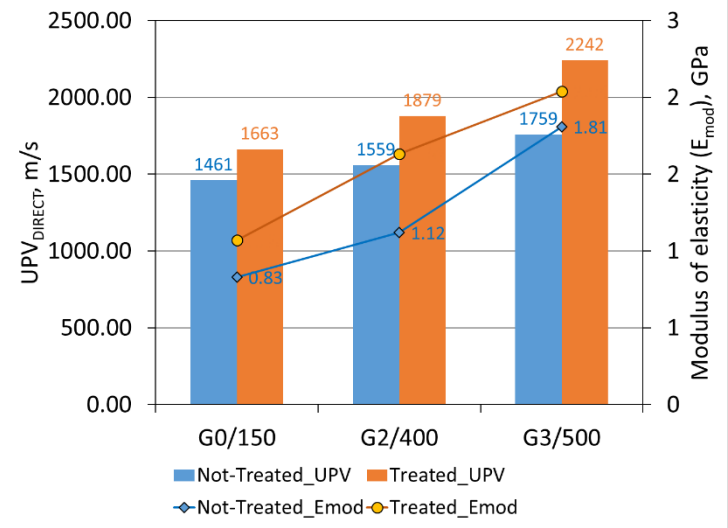

Figure 4.10. *UPV_{DIRECT}* and *E_{mod}* characteristics of both control and treated AAC types.

The results of the *UPV_{DIRECT}* measurements taken from along the height of treated AAC samples with the dimensions of 5×5×20 cm (**Figure 3.12 a**) revealed that penetration depth of nano $Ca(OH)_2$ solution in G2/400 samples was determined to be until 14 cm from the treated surface, while the penetration depth in G3/500 and G4/600 was found to be until 16 cm from the treated surface (**Table 4.8** and **Table 4.9**).

Table 4.8. UPV_{DIRECT} values determined for nine points taken along the height of AAC samples with the dimensions of 5×5×20 cm; **a)** control AAC types; and **(b)** AAC types treated with nano ($Ca(OH)_2$) solution.

(a)

Distance From the Surface to be Treated (cm)	UPV_{DIRECT}		
	G2/400	**G3/500**	**G4/600**
	m/s	m/s	m/s
2	1432	1512	1811
4	1479	1547	1849
6	1386	1604	1879
8	1402	1619	1947
10	1360	1583	1823
12	1467	1541	1760
14	1328	1576	1769
16	1469	1489	1892
18	1401	1438	1764

(b)

Distance From the Treated Surface (cm)	UPV_{DIRECT}		
	G2/400	**G3/500**	**G4/600**
	m/s	m/s	m/s
2	1798	1946	2232
4	1759	1846	2217
6	1702	1822	2200
8	1676	1793	2190
10	1643	1753	2160
12	1610	1716	2017
14	1426	1698	1996
16	1407	1462	1874
18	1397	1382	1760

Table 4.9. *$UPV_{INDIRECT}$* values determined for AAC samples with the dimensions of 5×5×20 cm; **a)** control AAC types; and **(b)** AAC types treated with nano $Ca(OH)_2$ solution.

(a)

Distance From the Surface to be Treated (cm)	$UPV_{INDIRECT}$		
	G2/400	**G3/500**	**G4/600**
	m/s	m/s	m/s
2	654	887	1067
4	533	737	889
6	516	670	792
8	510	566	710
10	501	556	661
12	467	546	605

(b)

Distance From the Surface to be Treated (cm)	$UPV_{INDIRECT}$		
	G2/400	**G3/500**	**G4/600**
	m/s	m/s	m/s
2	995	1370	1691
4	723	957	1287
6	625	781	981
8	610	672	823
10	599	663	720
12	570	574	690

4.6 Results of XRD Analyses

The XRD analyses were performed on powdered each AAC type to determine the major minerals present in the compositions. XRD analyzes were performed on each AAC type to identify the major minerals present in the compositions. A treated AAC sample was also analyzed for changes in mineral composition after being treated with nano ($Ca(OH)_2$) solution. The results presented as XRD traces show the main mineralogical composition giving information about the raw material sources. XRD results of the control G0/150, G2/400, G3/500, G4/600 and treated G4/600 samples were presented in **Figure 4.11**, **Figure 4.12**, **Figure 4.13**, **Figure 4.14**, and F**igure 4.15**, respectively.

The main minerals detected in four AAC types (G0/150, G2/400, G3/500, and G4/600) were Tobermorite and quartz. Calcite peaks were also found in lower intensity. In denser AAC types, the intensity of Tobermorite peaks were determined to be increased. Since Tobermorite crystals play a significant role in the characteristics of AAC materials, materials with higher Tobermorite intensity have higher structural strength. G4/600 has the highest intensity of Tobermorite peaks, while less Tobermorite intensity was detected in G0/150 (**Figure 4.11** and **Figure 4.14**).

After treatment with nano dispersive calcium hydroxide ($Ca(OH)_2$) solution, the intensity of calcite peaks increased due to the carbonation reaction of calcium hydroxide nanoparticles resulting in calcite formation (**Figure 4.15**). The increase in the intensity of calcite traces indicates the completion of the carbonation process in treated AAC samples.

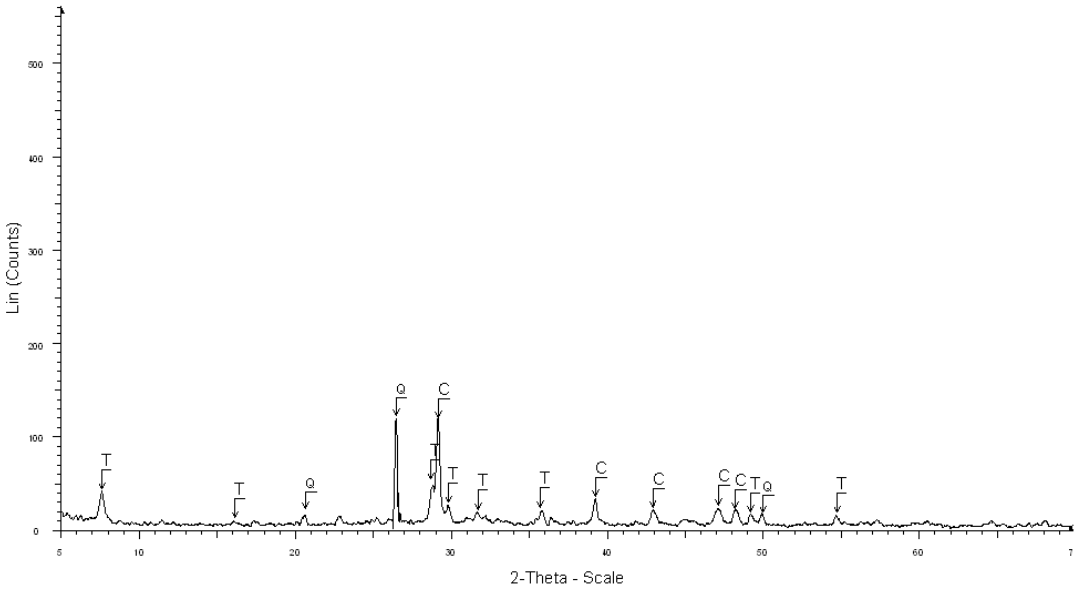

Figure 4.11. XRD traces of G0/150 sample (T: Tobermorite, Q: Quartz, C: Calcite).

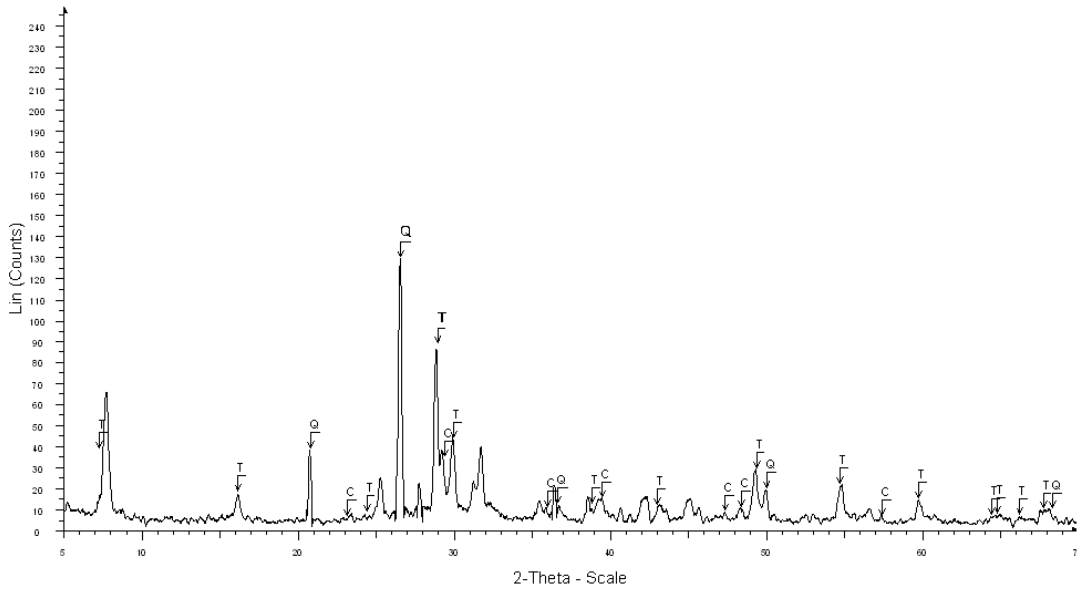

Figure 4.12. XRD traces of G2/400 sample (T: Tobermorite, Q: Quartz, C: Calcite).

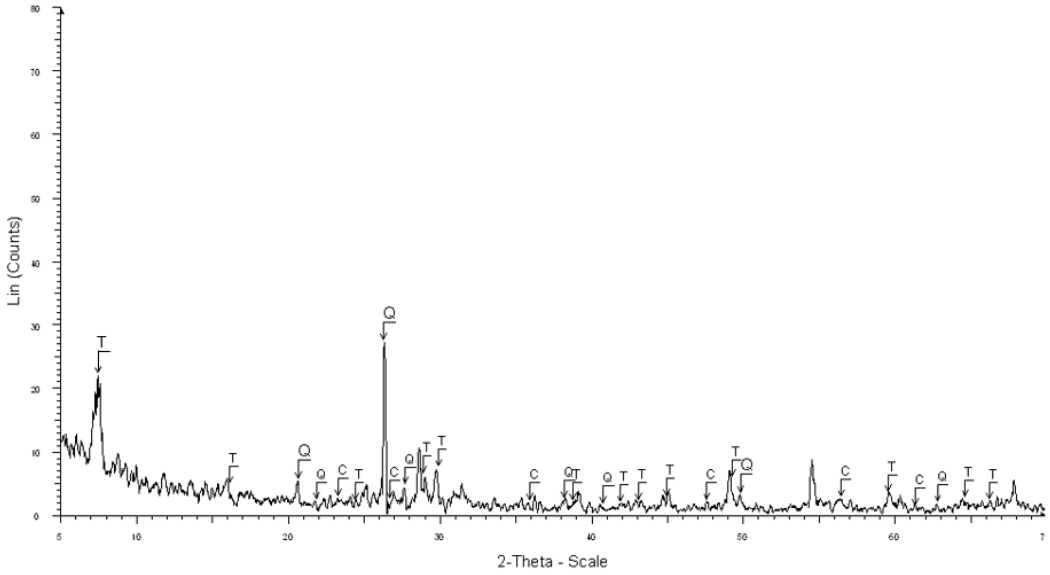

Figure 4.13. XRD traces of G3/500 sample (T: Tobermorite, Q: Quartz, C: Calcite).

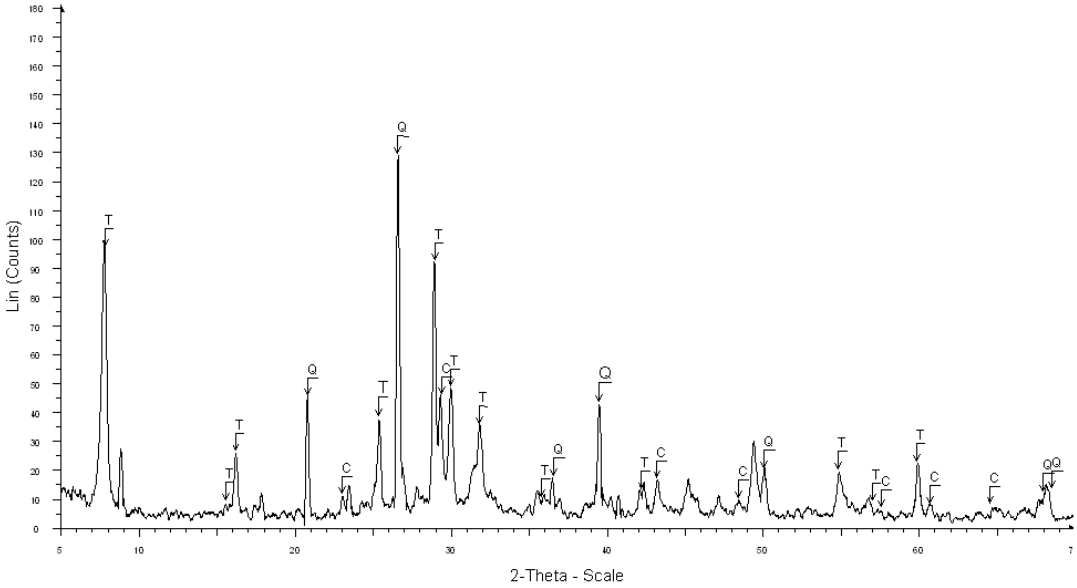

Figure 4.14. XRD traces of G4/600 sample (T: Tobermorite, Q: Quartz, C: Calcite).

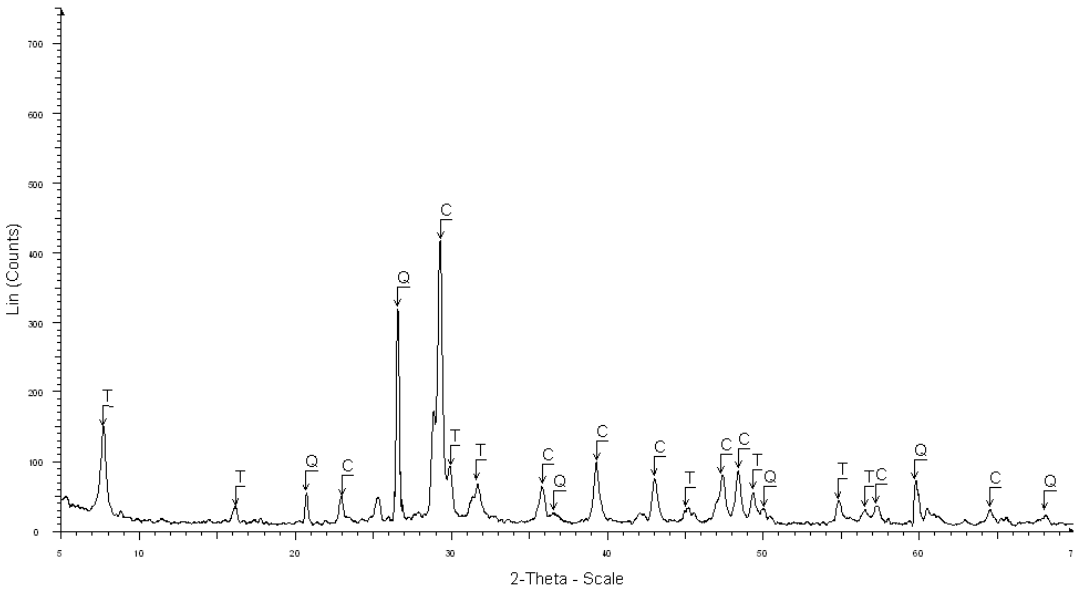

Figure 4.15. XRD traces of G4/600 sample treated with nano ($Ca(OH)_2$) solution (T: Tobermorite, Q: Quartz, C: Calcite).

4.7 Results of Image Analyses

In order to analyze the microstructure of the AAC samples after treatment with nano dispersive $Ca(OH)_2$ solution, image analyzes were performed on the surfaces and sections of AAC types in 7x and 40x magnification lenses. Visible pores were examined in terms of their size, shape, and distribution. The results of the image analyses are given as below:

— **Figure 4.16** shows stereomicroscope images taken from the surface perpendicular to the rising direction of the control G0/150, G2/400, G3/500, and G4/600 samples. The differences in porosity can clearly be observed in the images of G0/150 to G4/600 samples. While the abundance of large pores with small intervals is detected in G0/150, it is seen that the amount of air pores decreases in G2/400, G3/500, and G4/600. These observations are consistent with the results of measurements done on bulk density and porosity characteristics of the samples. As the amount of air pores decreases, the bulk density and the fine pore ratio increase, resulting in higher *UPV* values. The results of stereomicroscope images are well correlated with bulk density and porosity as well as *UPV* measurements results.

— As it is seen in **Figure 4.17**, large spherical pores of around 1 mm in size occupy a significant percentage of volume in sample G0/150. It is seen that spherical shaped pores are abundant on the sample matrix and placed very close to each other. Effective porosity of G0/150 was found to be 90% where only 0.7% of it was related to the fine pores. Therefore, it can be understood that, stereomicroscope images are in agreement with the results of the porosity measurements. Nano dispersive $Ca(OH)_2$ solution applied by penetration to the surface perpendicular to the rising direction of the G0/150 sample filled the large pores observed on the surface and a noticeable decrease in the size of the spherical pores was detected (**Figure 4.17 b**). The cross section of the sample perpendicular to the treated surface shows that nano dispersive ($Ca(OH)_2$) solution penetrated all through the sample. Calcium hydroxide nanoparticles were deposited in large pores and reduced their size to approximately 0.7–0.8 mm.

— As shown in **Figure 4.18**, G2/400 is less porous than G0/150 due to the reduction of aeration pores. Unevenly distributed large pores of diameters around 1 mm are less abundant. The distance between the large pores are less in comparison to G0/150. The pores on the treated surface seem to decrease in size after the treatment by nano dispersive ($Ca(OH)_2$) solution. At 7x magnification (**Figure 4.18 c**), the cross section surface of treated G2/400 shows that the nano solution has well penetrated through the sample. At the 40x magnification of the image (**Figure 4.18 c**), it can be seen that the nanoparticles filled the periphery of the aeration pores and decreased their size. The results of the porosity measurements showed a decrease in effective porosity as well as fine porosity after treatment. By observing nanoparticle deposition in the periphery of large pores as well as in the fine porosity matrix, stereomicroscope images support the results of the porosity characteristics.

— **Figure 4.19** represents the texture of control G3/500 sample. As it can see, G3/500 has lower ratio of large pores compared to G2/400 and G0/150 samples. As the AAC samples become denser, the distribution of large pores and the size of the aeration pores decrease. Large pores with diameters less than 1 mm are observed in the material matrix (**Figure 4.19 b**). Based on the results of porosity characteristics, a large decrease of about 10% in effective porosity of G3/500 sample, which is greater than G0/150 and G2/400, was determined after treatment. The pores on the treated surface seem to decrease in size after the treatment by nano dispersive ($Ca(OH)_2$) solution. The cross section surface of treated G3/500 shows that that the nano solution reached the bottom of the sample through the fine or capillary pores (**Figure 4.19 c**). The nano solution filled a large volume of fine pores, while the most of the air pores decreased in size.

— As shown in **Figure 4.20**, G4/600 is the least porous among other examined AAC types. Effective porosity of G4/600 was found to be 72%, where 1.40% of it was related to the fine pores. The fine pore ratio in G4/600 was determined to be higher compared to the other AAC types. Therefore, it can be understood that stereomicroscope images are in agreement with the results of the porosity

measurements. Unevenly distributed large pores of diameters around 0.7 mm in less intensity with higher intervals are observed. The pores on the treated surface seem to decrease in size after the treatment by nano dispersive ($Ca(OH)_2$) solution. The cross section surface of treated G4/600 shows that the nano solution reached the bottom of the sample (**Figure 4.20 c**). The nano ($Ca(OH)_2$) solution was transferred to the bottom of the treated surface by capillary suction and deposited in large pores as well as filled the fine pores.

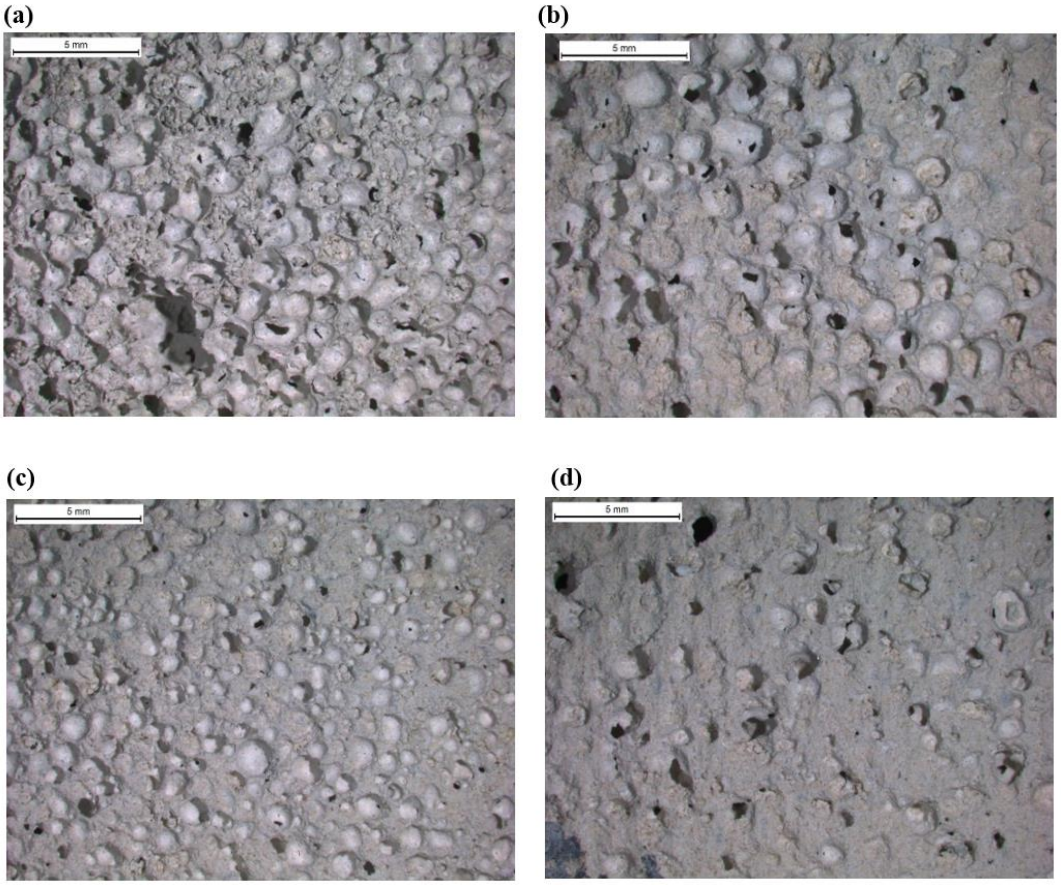

Figure 4.16. Stereomicroscope images of samples taken from the surfaces perpendicular to the rising direction of control samples with the magnification of 7x **(a)** G0/150; **(b)** G2/400; **(c)** G3/500, and **(d)** G4/600.

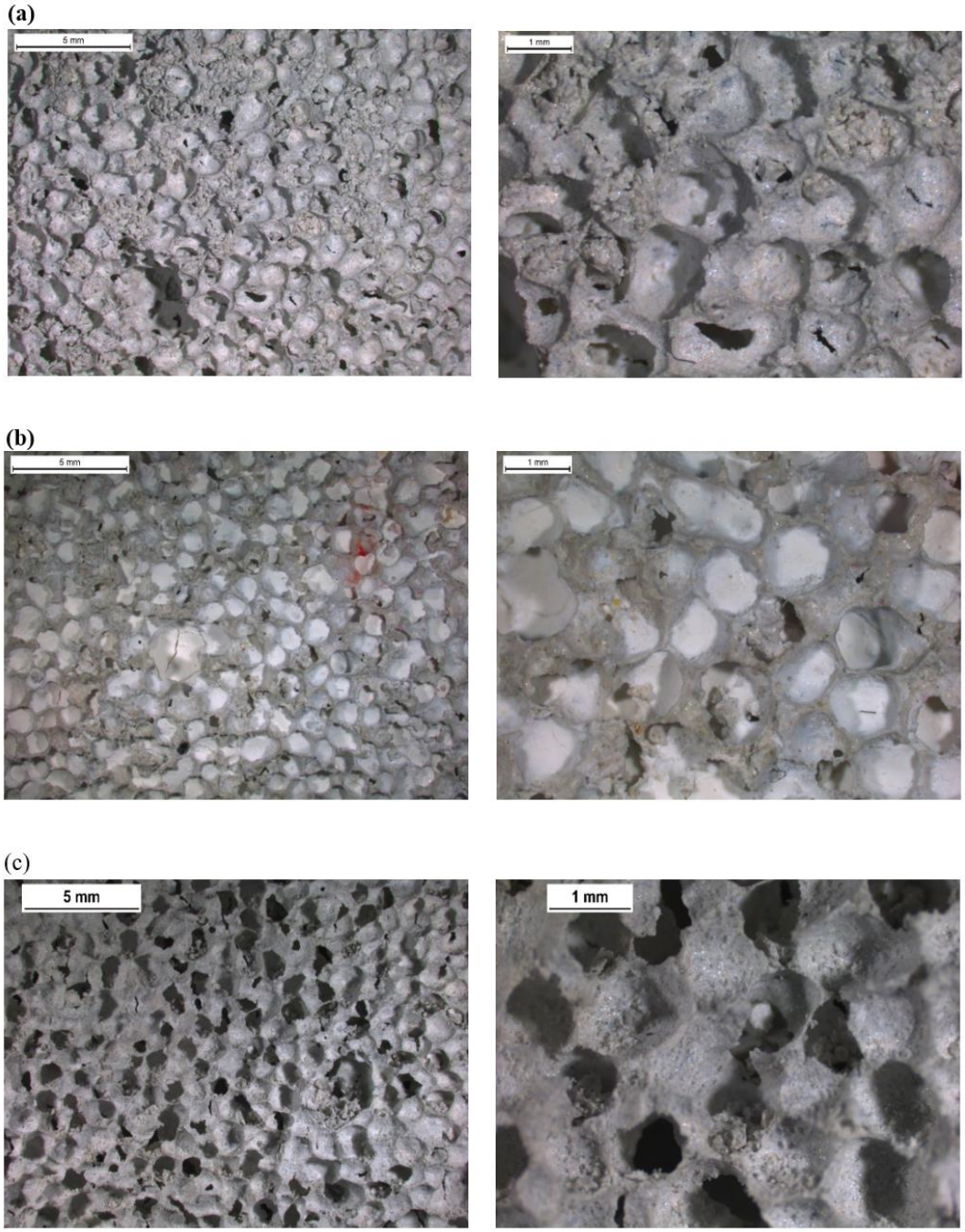

Figure 4.17. Stereomicroscope images showing the surfaces views of G0/150 sample in perpendicular to the rising direction **(a)** the untreated surface (7x-left, 40x-right); **(b)** the treated surface (with nano dispersive $Ca(OH)_2$ solution) (7x-left, 40x-right); and **(c)** stereomicroscope images of the cross section views taken from the lower part of the treated sample showing that nano dispersive solution is penetrated up to the end of the capillary rise direction of AAC sample (7x-left, 40x-right).

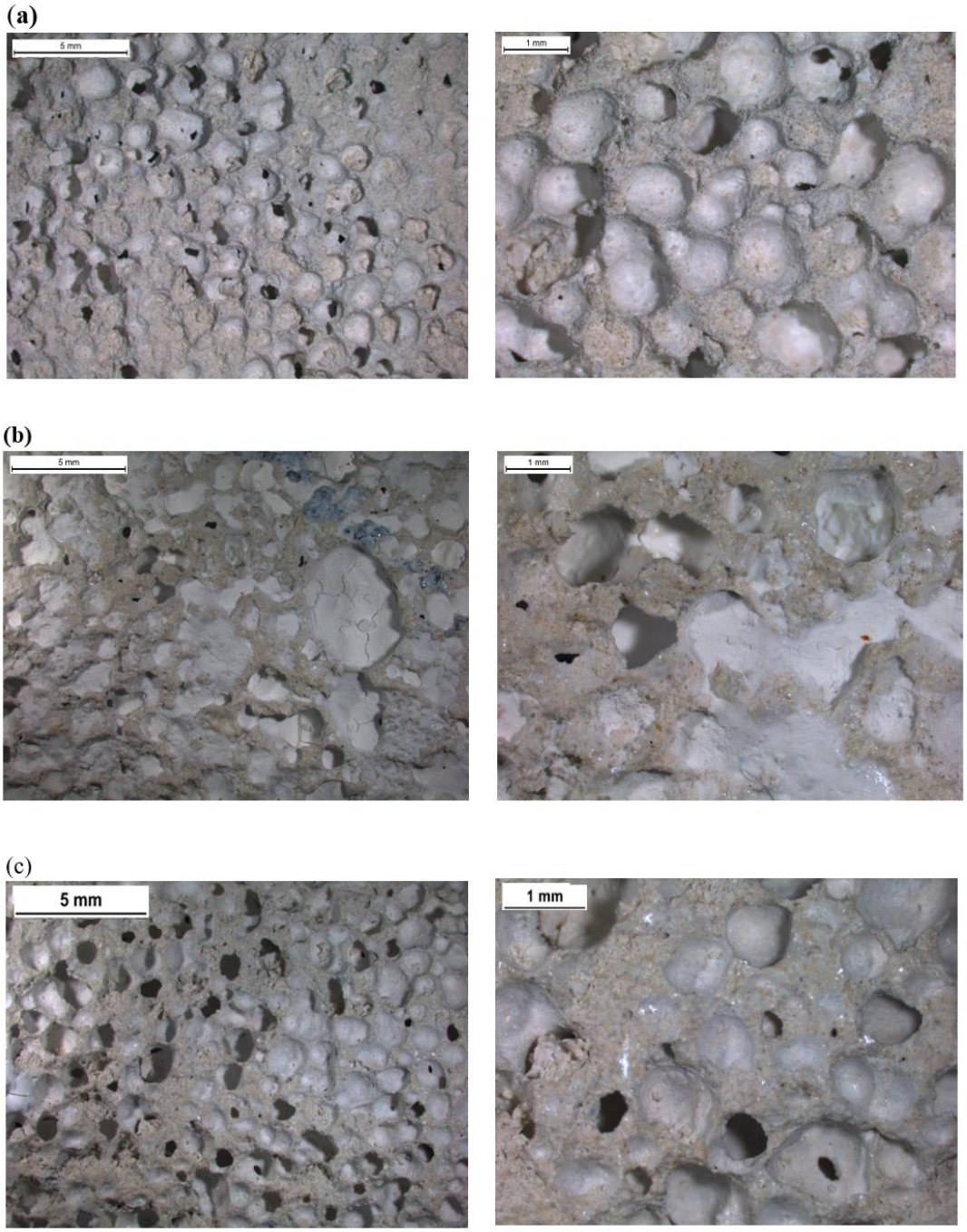

Figure 4.18. Stereomicroscope images taken from G2/400 sample: **(a)** surface views before treatment in perpendicular to the rising direction (7x-left, 40x-right); **(b)** the surface perpendicular to the rising direction treated with nano dispersive ($Ca(OH)_2$) solution (7x-left, 40x-right); **(c)** cross section view taken from the lower part of the treated sample (7x-left, 40x-right).

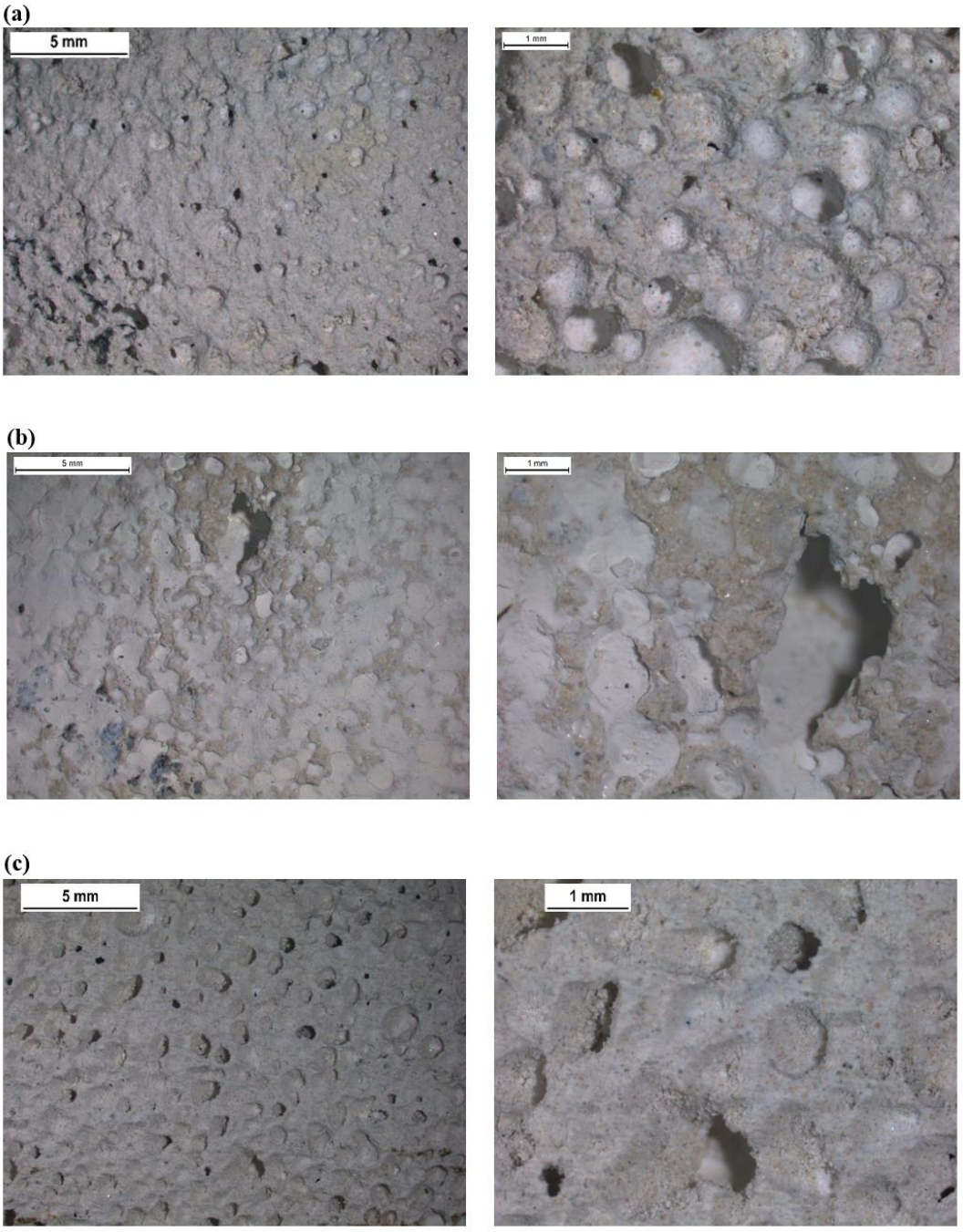

Figure 4.19. Stereomicroscope images taken from G3/500 sample: **(a)** surface views before treatment in perpendicular to the rising direction (7x-left, 40x-right); **(b)** the surface perpendicular to the rising direction treated with nano dispersive ($Ca(OH)_2$) solution (7x-left, 40x-right); **(c)** cross section view taken from the lower part of the treated sample (7x-left, 40x-right).

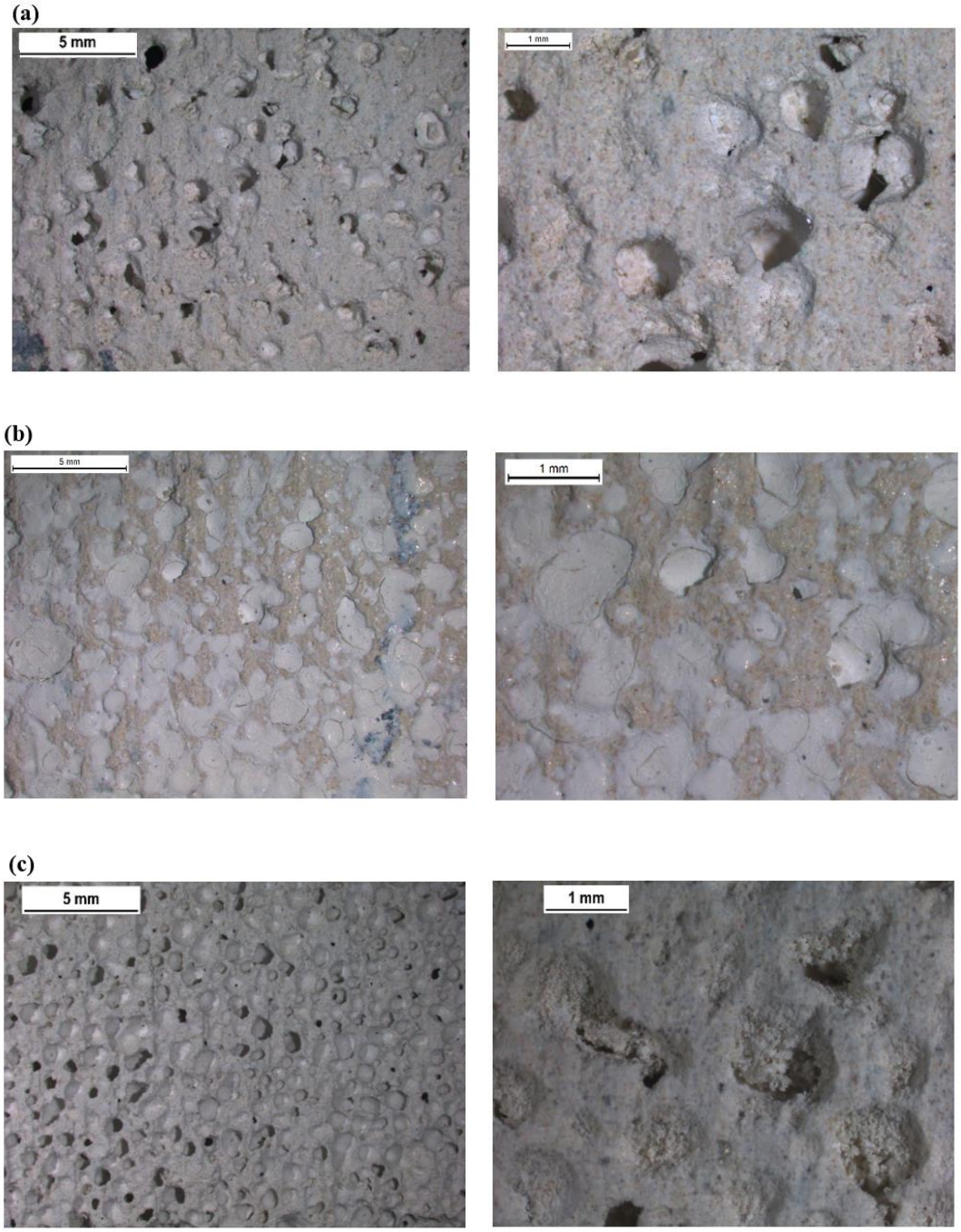

Figure 4.20. Stereomicroscope images taken from G3/500 sample: **(a)** surface views before treatment in perpendicular to the rising direction (7x-left, 40x-right); **(b)** the surface perpendicular to the rising direction treated with nano dispersive ($Ca(OH)_2$) solution (7x-left, 40x-right); **(c)** cross section view taken from the lower part of the treated sample (7x-left, 40x-right).

CHAPTER 5

DISCUSSION

In this chapter, the joint interpretation of the results was done:

- to evaluate the materials properties of four types of Autoclaved Aerated Concrete (AAC) products with a focus on their hygric properties, and to discuss their inherent potentials and shortcomings related to their moisture-related performances,
- to examine the porosity characteristics of AAC types before and after treatment with nano dispersive calcium hydroxide $Ca(OH)_2$ solution to better understand the effect of calcium hydroxide nanoparticles on porosity matrix,
- to evaluate the impact of treatment on hygric and physicomechanical properties of AAC types,
- to explain guiding remarks for ultrasonic testing, which is important in monitoring the effect of treatment in on-site applications.
- to discuss the data to be guiding for the improvement of standards related to the performance properties of AAC products.

5.1 Evaluating the Material Properties of AAC Products

The overall data achieved on the basic physical, physicomechanical and moisture-related properties of AAC products are discussed together to better understand their hygric behavior in comparison to each other. The data evaluation has shown the followings:

— All AAC products are lightweight, highly porous, and highly vapor permeable building materials having high water absorption and capillary

suction properties (**Table 5.1**). Therefore, these AAC materials should be protected from direct rainwater exposure.

Table 5.1. Material properties of AAC types in terms of bulk density (ρ), effective porosity (φ), water absorption capacity (θ), saturation coefficient (*S-value*), fine pore porosity ($\varphi_{0.5\mu}$), water vapor diffusion resistance index (μ-*value*), capillary water absorption coefficient perpendicular to rising direction (*A-value*), and ultrasonic pulse velocity (*UPV*) characteristics.

Sample Name	ρ	φ	θ	*S-value*	$\varphi_{0.5\mu}$	μ-*value*	*A-value*	*UPV*
	g/cm^3	% by volume	% by weight	unitless	% by volume	unitless	kg/m^{2}s$^{0.5}$	m/s
G0/150	0.16	90.25	561.43	0.32	0.7	2.25	0.0523	NA
G2/400	0.42	80.57	193.12	0.45	1.02	3.75	0.0675	1461
G3/500	0.50	77.33	154.99	0.52	1.19	3.97	0.0701	1559
G4/600	0.62	71.78	115.33	0.64	1.40	4.09	0.1225	1759

— AAC products specifically manufactured according to the functions expected from them exhibit a gradual increase in density and a gradual decrease in effective porosity (**Figure 5.1**). Briefly, the products serving as load-bearing purposes have higher bulk density while they are still remarkably lightweight masonry units or panels compared to other building materials, such as cement-based plasters, concrete, fired clay units, stone types (**Table 5.1**).

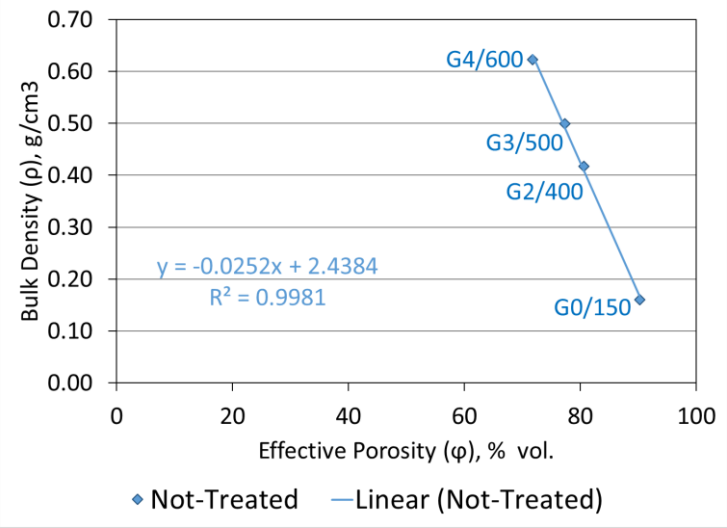

Figure 5.1. The graph showing the correlation between bulk density (ρ) and effective porosity (φ) of AAC types.

— The large-sized pores are visible in cross-section views taken by optic microscope. According to the image analyses, the largest pore sizes around 1mm in diameter are observed in the porosity matrices of G2/400 and G0/150 samples while G4/600 and G3/500 samples contain large pores, being smaller than 1mm in diameter (around 0.7-0.8 mm). (**Figures 4.16**). G0/150 sample differs from the other AAC products since it contains a significant amount of large pores. The distances between the largest-sized pores are much less when compared to the others' porosity matrix. (**Figures 4.16**).

— All AAC product differ in their basic physical and physicomechanical properties related to their functions (**Table 5.1**). For instance, G4/600 sample, used as the load bearing masonry unit, and G3/500 sample, used as AAC panels with reinforcement, have the highest bulk densities of 0.62g/cm^3 and 0.50g/cm^3 and the lowest effective porosities of 72% and 77% (by volume), respectively. However, G2/400 sample, used as masonry infill unit, has lower bulk density and higher effective porosity (with values of 0.42g/cm^3 and 81% by vol., respectively) compared to the former ones. The increase in *UPV* and E_{mod} values related to the bulk densities of these products verifies the differences in their performance properties related to their functions (**Figure 5.8**).

— G0/150 sample, used as thermal insulation board and specifically produced for external insulation purposes, differs from the other AAC products (G2/400, G3/500, G4/600) used as masonry unit and panel elements (**Table 5.1**). G0/150 products have extremely low bulk density and very high effective porosity (with the values of 0.16g/cm^3 and 90% by volume, respectively). Due to the discontinuities in the matrix of G0/150 samples, transit time from those samples could not be measured during *UPV* testing in direct and indirect transmission modes (**Figure 5.8**). That signals the weakness of G0/150 products in terms of physicomechanical properties.

— What is observed that the denser products having lower effective porosities have higher fine porosity, higher saturation coefficient (*S-value*) and

capillary water absorption coefficient (*A-value*) (**Figure 5.2** and **Figure 5.3**). In other words, the denser AAC products have higher fine pores in their matrix that makes them more vulnerable to capillary water absorption and freezing-thawing cycles.

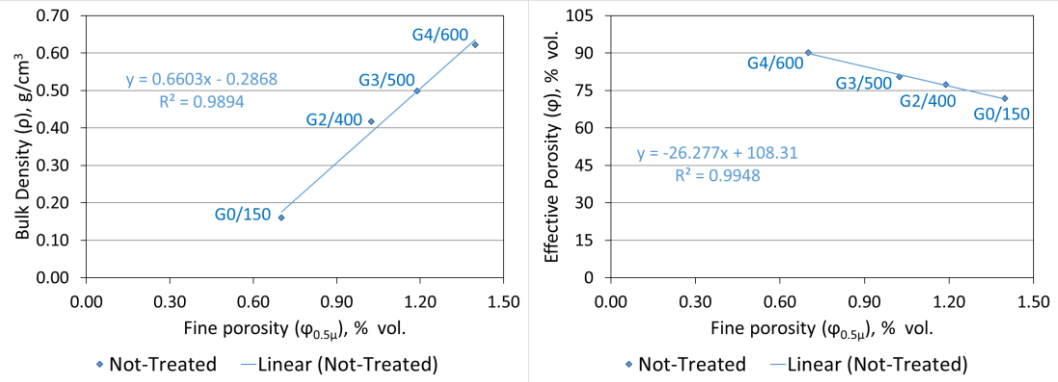

Figure 5.2. Graphs showing the correlations between bulk density (ρ) and fine porosity ($\varphi_{0.5\mu}$,) (left) effective porosity (φ) and fine porosity ($\varphi_{0.5\mu}$,) (right) of AAC types.

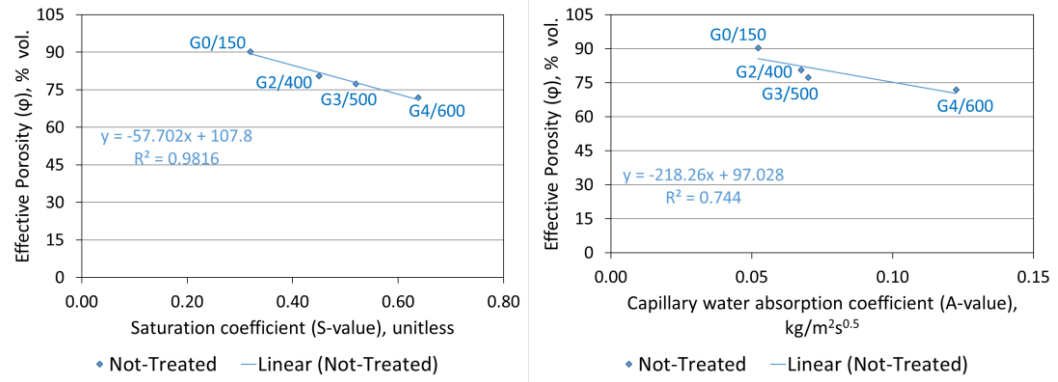

Figure 5.3. Graphs showing the correlations between effective porosity (φ) and saturation coefficient (*S-value*) (left) effective porosity (φ) and capillary water absorption coefficient (*A-value*) (right) of AAC types.

— When compared to other building materials, concrete has lower capillary water absorption (*A-value*) characteristics than the examined AAC products (**Table 5.2**). However, most natural stones, such as granite, andesite, marble types have considerably lower *A-value* than AAC products and concrete (**Table.5.2**). On the other hand, some tuffs have higher capillary suction than AAC products, while some tuffs have similar capillary suction characteristics

to the AAC products. Expectedly, polymer-modified cement-based plasters used as protective coats have lower *A-value* than AAC products. The fired-clay bricks, either historical or modern ones, have considerably higher capillary water suction characteristics than the building materials mentioned above. Adobe, such as handmade (unfired) earth bricks, have much lower capillary water suction characteristics than the AAC products, while some marble and granite stones have similar capillary suction to adobe (**Table 5.2**). In short, even the densest AAC types are not appropriate building materials that can be used in buildings below the ground level and at conditions exposed to rainwater penetration.

Table 5.2. List of capillary water absorption coefficient values of some building materials compiled from the literature and AAC products examined in this study.

Materials	**Capillary Water Absorption Coefficient (*A-value*, kg/m^{2}s$^{0.5}$)**	**Reference**
Traditional handmade fired clay brick	0.205	Karagiannis *et al*., 2016
Typical fired clay brick	0.270	Karagiannis *et al*., 2016
Tuff	0.190-0.401	Ünal and Altunok, 2019
Modern brick	0.150	Camino *et al*., 2014
Rhodes quarry stone (limestone)	0.101	Karagiannis *et al*., 2016
Rethymno quarry stone	0.089	Karagiannis *et al*., 2016
AAC products examined in the study	**0.0523-0.1225**	**This Study**
Concrete C20/25	0.014	Tuominen and Vinha, 2019
Concrete C32/40	0.010	Tuominen and Vinha, 2019
Andesite	0.005-0.018	Ünal and Altunok, 2019
Polymer modified cement-based plaster	0.0012	Tuominen and Vinha, 2019
Granite	0.0006-0.0007	Ünal and Altunok, 2019
Marble	0.0005	Ünal and Altunok, 2019
Adobe	0.0002	Babé *et al*., 2020

— Saturation coefficient (*S-value*) is defined as the durability of the material through freezing-thawing cycles. *S-values* of four types of AAC products are in the range of 0.32 and 0.64 (**Table 5.1**). That range is lower than the 0.8 threshold value, therefore AAC products can be assumed to suffer less from

freezing-thawing cycles since they are expected to get wet (saturated level) slower than the materials having a saturation coefficient above 0.8. On the other hand, the examined AAC products absorb water in high amounts. This means that the AAC products can get wet easier in water exposure and their wet parts may suffer from freezing-thawing cycles although their *S-value* is lower than 0.80.

— Presence of fine pores in an interconnected pore structure are known to result in a higher saturation coefficient and capillary water absorption. In other words, fine and capillary pores play a significant role in the transmission of water to the entire structure of the material. The results showed that AAC types with higher fine porosity (the volume of the pores below 0.5µm) have higher *S-value* (**Figure 5.4**), consequently, get wet faster in water-exposed conditions. G4/600 with a higher proportion of fine pores in its pore structure ($\varphi_{0.5\mu}$=1.40% by vol.) has a higher *S-value* among others, which indicates that G4/600 is more susceptible to weathering conditions than other AAC products. On the other hand, G0/150 has the lowest *S-value*, since fine pores account for a lower proportion of its porosity. There is a strong correlation between fine porosity and *S-value* of AAC types (**Figure 5.4**).

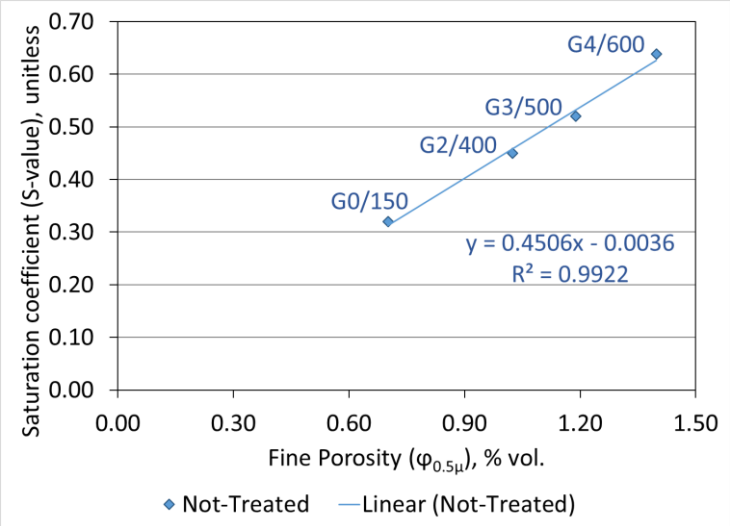

Figure 5.4. The graph showing the correlation between saturation coefficient (*S-value*) and fine porosity (***φ0.5µ*,**) of AAC types.

— In addition, as fine porosity increases, the AAC samples absorb a higher amount of water by capillary suction (**Figure 5.5**). Among the AAC products, G4/600 has a higher capillary water absorption capacity (*A-value*) both in the rising direction and perpendicular to the rising direction, as the proportion of fine pores is higher in its structure. However, G0/150 with lower fine porosity has the lowest *A-value* than other AAC types.

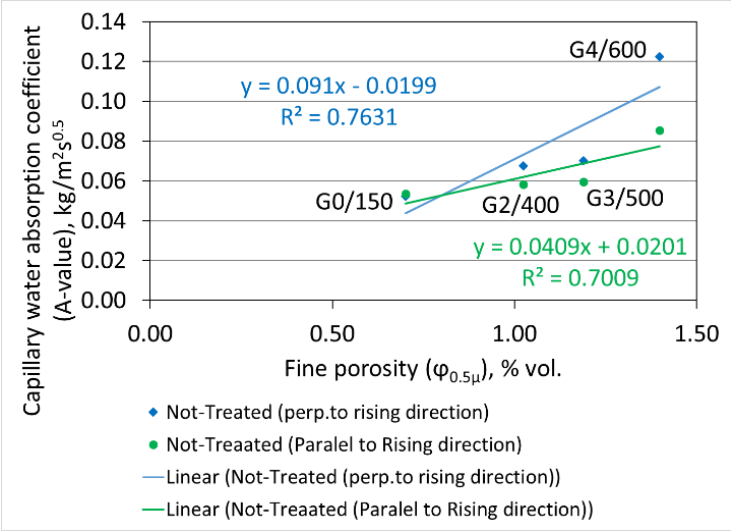

Figure 5.5. The graph showing the correlation between capillary water absorption coefficient (*A-value*) and fine porosity (***φ0.5μ*,**) of AAC types in both the rising direction and perpendicular to the rising direction.

— For G4/600 product, the capillary suction behavior changes depending on the rising direction (**Figure 4.9**). G4/600's *A-value* in perpendicular to the rising direction is higher than the capillary suction on the rising direction. This presents the anisotropic behavior of the G4/600 product. That property also signals that its pore structure on the axis perpendicular to the rising direction involves more capillary pores and/or interconnected fine pores. Depending on this property, the rainwater penetration through its exposed wall surface can be riskier than the capillary suction on the vertical axis through the wall height.

— The ultrasonic pulse velocity measurements taken in direct transmission mode (UPV_{DIRECT}) showed that AAC products varying in bulk density and

effective porosity have *UPV* data in different ranges. Among four AAC types, the denser AAC product have higher UPV_{DIRECT} and $UPV_{INDIRECT}$ values (**Figure 5.6** and **Figure 5.8**). A strong correlation was achieved between UPV_{DIRECT} and $UPV_{INDIRECT}$ values varying depending on ACC product types (**Figure 5.7**).

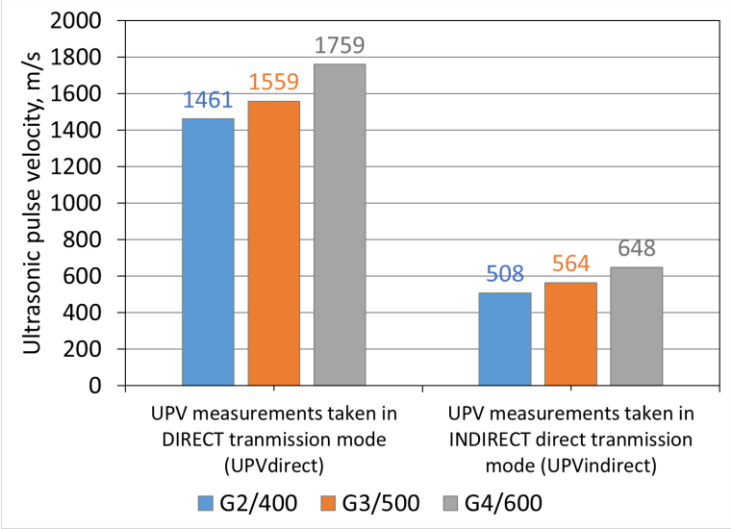

Figure 5.6. The graph showing the UPV_{DIRECT} and $UPV_{INDIRECT}$ values of AAC products, G2/400, G3/500 and G4/600.

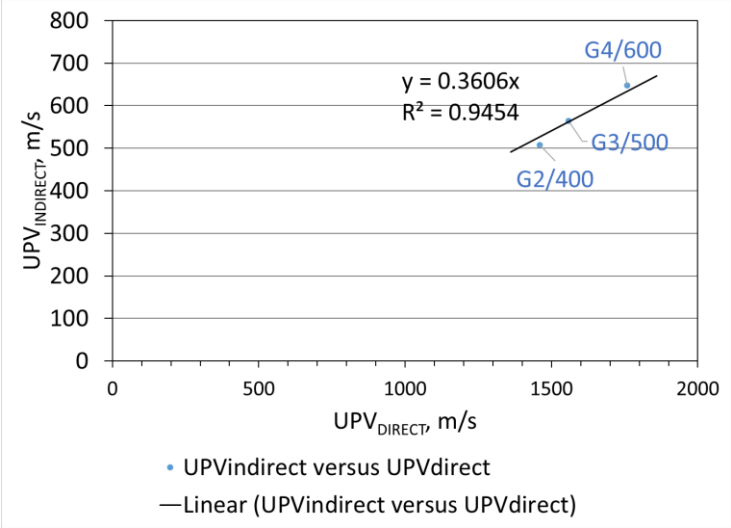

Figure 5.7. The graph showing the linear regression between UPV_{DIRECT} and $UPV_{INDIRECT}$ values of AAC products, G2/400, G3/500 and G4/600.

— The AAC products behave isotropic in terms of physicomechanical properties. The UPV_{DIRECT} and $UPV_{INDIRECT}$ measurements taken from each product type have shown that the *UPV* data are similar both in parallel and perpendicular to the rising direction (**Table 4.6** and **Figure 5.8**).

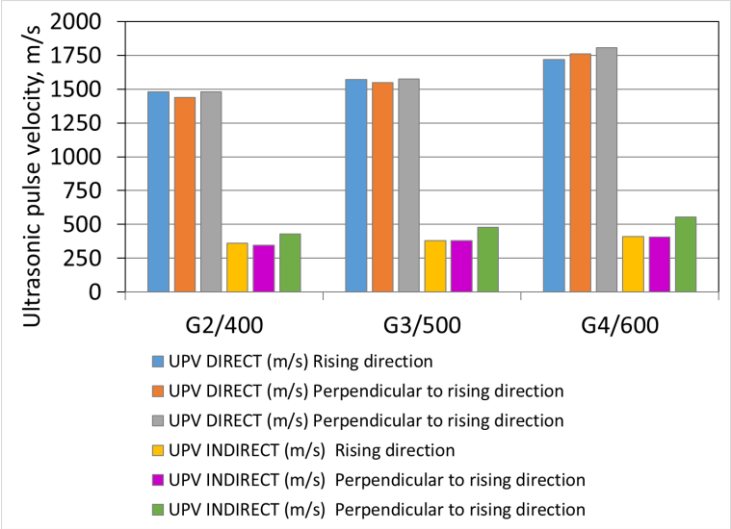

Figure 5.8. The graph showing the UPV_{DIRECT} and $UPV_{INDIRECT}$ data taken from all directions of AAC samples.

5.2 Impact of $Ca(OH)_2$ Nano Dispersive Treatment on Hygric Properties of AAC Products – Performance Evaluation

After being treated with nano dispersive $Ca(OH)_2$ solution from the surface perpendicular to the rising direction, nanoparticles penetrated the pore structure of the AAC samples and deposited in large pores, and filled the fine pores, thus increasing the density (**Table 5.5**). The effective porosity of treated G0/150, G2/400, G3/500, and G4/600 samples were found to decrease by approximately 2.8, 10, and 13% by volume, respectively (**Table 5.5**). The highest reduction in effective porosity was detected in G4/600, which has the lowest effective porosity among other AAC types. Since G4/600 is composed of higher amounts of fine pores, $Ca(OH)_2$ nanoparticles can easily transfer throughout the sample and fill the fine pores as well as deposition in the smaller and less abundant large pores. Therefore, it can be concluded that nano $Ca(OH)_2$ treatment is more effective in AAC types with lower

effective porosity and higher fine porosity. G0/150 showed a lowest reduction in effective porosity following treatment. According to the cross-section analyses, nano $Ca(OH)_2$ treatment reached the opposite side of the treated surface; however, nanoparticles were only deposited on the periphery of pores in a smaller amount. The reduction in fine porosity was determined to be the same in treated G0/150, G2/400, and G3/500 samples, which was about 26% by volume. However, due to the high proportion of fine pores in G4/600, the nano solution dispersed in all fine and capillary pores and deposited in them in lower amounts, resulting in the lowest reduction in fine porosity after treatment of about 23% by volume.

Consequently, G0/150 showed a higher increase in density after treatment, as higher amounts of nano $Ca(OH)_2$ solution were transferred through fine and capillary pores, which constitute a small percentage of volume in the porosity structure, resulting in a higher reduction in fine porosity. In contrary, G4/600 with a porosity structure composed of a higher proportion of fine pores has the highest reduction in effective porosity following treatment, but the lowest reduction in fine porosity and density, due to the small amounts of calcite crystals formed in capillary pores (**Table 5.5**).

Table 5.3. The changes in density and porosity characteristics of AAC types after treatment.

Material Properties	**Sample Name**			
	G0/150	**G2/400**	**G3/500**	**G4/600**
Density, (% increase)	13	3	2	2
Effective Porosity, (% decrease)	2	8	10	13
Fine porosity, (% decrease)	26	26	27	23

The reduction in effective porosity and fine porosity after treatment reduced the water absorption capacity in AAC samples to some extent. The water absorption capacity of AAC types is extremely high, and it increases as effective porosity increases. The reduction in effective porosity and water absorption values was higher in AAC types with higher density values, indicating that nano treatment was more successful in denser AAC samples. On the other hand, the nano solution treatment

enabled the AAC types even more permeable. The tiny cracks mentioned in the literature at the surface perpendicular to the rising direction of AAC products connect most of the large pores (Narayanan and Ramamurthy, 2000; Ioannou *et al*., 2008; Schober, 2011; Qu and Zhao, 2017; Matsuno *et al*., 2020; Chen, *et al*., 202). Therefore, after treatment, high amounts of water vapor seem to pass through a short channel consisting of cracks and large pores due to the deposition of calcium hydroxide nanoparticles in capillary pores.

The results of the evaporation rate and critical moisture content analyses determined that treated AAC samples absorbed less water with the reduction in their porosity. AAC samples with higher porosity were found to have a higher reduction in water content after treatment. Therefore, treated AAC samples dried in a shorter time than the control samples. The nano $Ca(OH)_2$ treatment applied on the surface perpendicular to the rising direction was observed to increase the evaporation rate (R_E), indicating that drying was faster from the wet surface. As a result, when the AAC product is wet, the surface will dry out faster. The critical moisture content (θ_C) in the treated AAC samples increased to almost half the effective porosity. This indicates that wetting by capillary suction from the surface perpendicular to the rising direction after treatment requires higher moisture content. This is an improvement in the hygric properties of AAC that results in delayed capillary absorption behavior.

The reduction of fine pores after treatment was found to be higher in AAC types with higher fine porosity as the nano ($Ca(OH)_2$) solution is transferred throughout the entire porosity matrix by interconnected fine pores and capillary pores. Therefore, the *S-value* of treated AAC samples was gradually reduced by decreasing fine porosity. The highest reduction in *S-value* was observed in treated AAC types with a high amount of fine pores. G4/600 has the highest reduction among other AAC types in *S-value* following treatment (**Figure 5.6**).

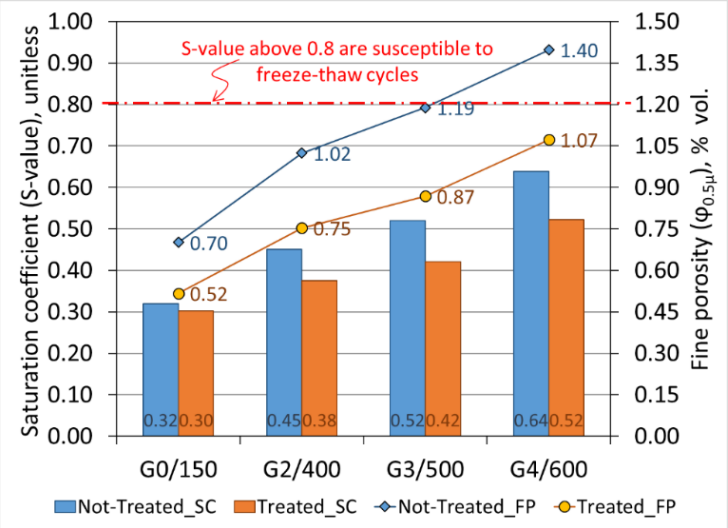

Figure 5.9. Saturation coefficient (*S-value*) and fine porosity ($\varphi_{0.5\mu}$) characteristics of both not-treated(control) and treated AAC samples.

After treatment, the increase in capillary suction in the rising direction indicates that calcite particles accumulated more horizontally than vertically. The cross-section image analyses showed that calcite particles filled the fine pores and accumulated in the inner periphery of the larger pores. This calcite deposition seems to change the pore structure in the rising direction to a certain depth by forming interconnected fine pores. On the other hand, the nano dispersive $Ca(OH)_2$ treatment applied on the surface perpendicular to the rising direction reduced the capillary water suction in the range of 13% to 18%, except for the G0/150 which is used as an insulation board. The nano $Ca(OH)_2$ solution penetrated quickly when applied to the surface perpendicular to the rising direction and deposited in the interconnected fine pores and capillaries, which are larger in amount, resulting in less capillary suction after treatment. The penetrativity of G0/150 with the lowest fine pores was determined to be the fastest, while the amount of water in the capillary pores was the lowest. On the contrary, G4/600 has the lower penetrativity than G0/150 with higher water content in the capillary pores. It is clear that G4/600, which has the highest fine porosity (volume of fine pores) and saturation coefficient (*S-value*), has the highest capillary water absorption coefficient (*A-value*) and sorptivity. The hygric behavior

of G4/600 signals that this AAC type is more susceptible to freezing-thawing than the other types when exposed to wetting conditions at cold seasons.

5.3 Impact of $Ca(OH)_2$ Nano Dispersive Treatment on Physicomechanical Properties of AAC products – Performance Evaluation

The physicomechanical properties of AAC products are influenced by their bulk density and effective porosity. Ultrasonic testing gives information about the porosity characteristics of the material. The more porous the material, the longer the ultrasonic waves find a path to run through the solid matrix, resulting in higher ultrasonic readings. Among four AAC products examined in this study, data acquisition by ultrasonic testing is not available for the G0/150 sample. This experience during *UPV* measurements shows that the solid part of G0/150 is weak to pressure. The reduction in ultrasonic readings after treatment with alcohol dispersion of $Ca(OH)_2$ nanoparticles indicates that the porosity of the AAC materials is decreased due to the penetration of nanoparticles into the pore structure and deposition in large pores and filling the capillaries. Changes in porosity following treatment resulted in an increase in density values. *UPV* values increase with the increase in density. The G4/600 sample with the highest density value has the highest *UPV* among other AAC types. The effect of alcohol dispersion of $Ca(OH)_2$ treatment is associated with an increase in their *UPV* values in direct and indirect transmission modes, while this effect is not significant in terms of bulk density. Denser AAC samples showed higher changes in their *UPV* values with a slight increase in density following treatment. The highest *UPV* value is recorded in G4/600 after treatment, even with a small increase in density (**Figure 5.7**).

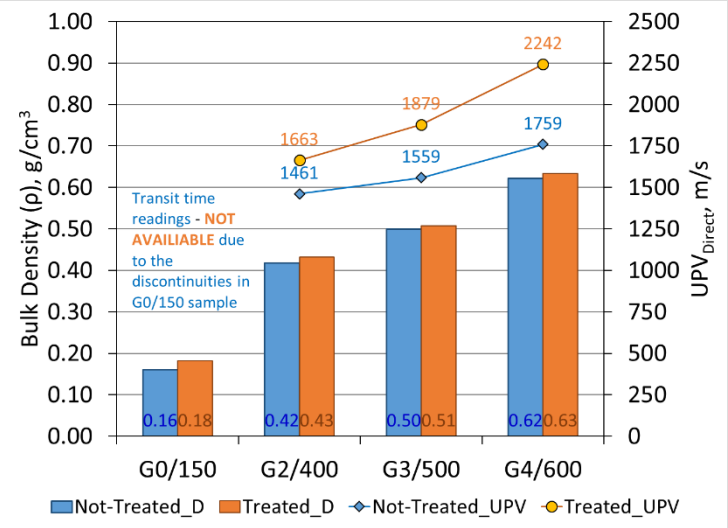

Figure 5.10. Bulk density (ρ) and UPV_{DIRECT} characteristics of both not-treated(control) and treated AAC samples.

The nano dispersive $Ca(OH)_2$ solution penetrated throughout the sample by the capillary pores. Therefore, AAC types with a higher proportion of fine and capillary pores showed higher penetration depth. According to the results of the UPV_{DIRECT} measurements, the penetration depth of the G2/400 is lower than G3/500 and G4/600, which is about 14 cm from treated surface (**Figure 5.11**). However, the penetration depth of the G3/500 and G4/600 samples are up to the 16 cm from treated surface (**Figure 5.12** and **Figure 5.13**). It has to be mentioned that depending on the amount of nano dispersive $Ca(OH)_2$ solution penetrated by capillary suction, the penetration depth can be varied. Furthermore, *UPV* measurements determine the strength of the material. As the *UPV* values increases, the strength of the material increases. Due to the reduction in porosity with the deposition of nanoparticles, the *UPV* values of examined AAC types were increased, leading to higher compressive and flexural strength

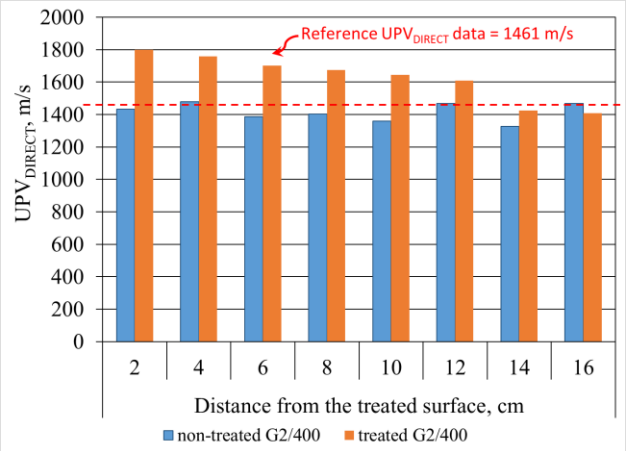

Figure 5.11. The penetration depth of nano dispersive $Ca(OH)_2$ solution from treated surface in G2/400 product.

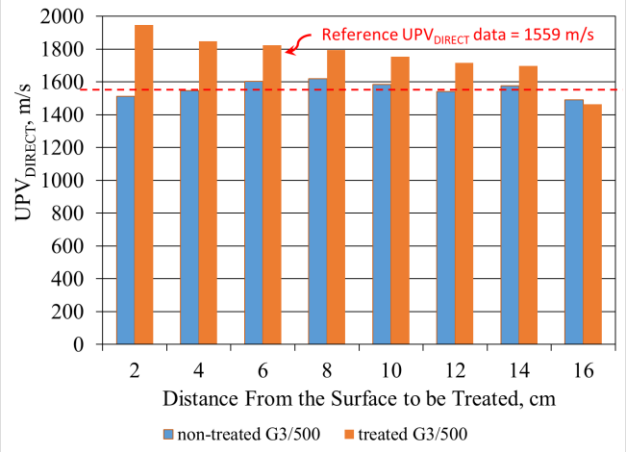

Figure 5.12. The penetration depth of nano dispersive $Ca(OH)_2$ solution from treated surface in G3/500 product.

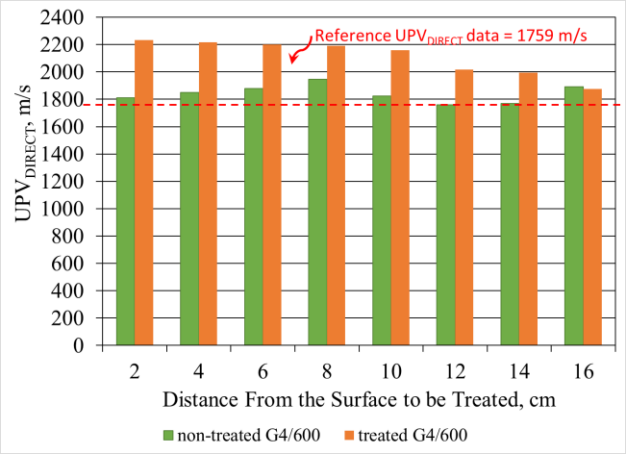

Figure 5.13. The penetration depth of nano dispersive $Ca(OH)_2$ solution from treated surface in G4/600 product.

5.4 Guiding Remarks for Reliable UPV Measurements of AAC samples

It is worthwhile to mention that ultrasonic testing is a promising non-destructive testing method for in-situ monitoring of G2/400, G3/500, and G4/600 products since reliable UPV_{DIRECT} and $UPV_{INDIRECT}$ data could be achieved in the study. On the other hand, due to the poor strength of G0/150 product against slight pressure applied by the probes during *UPV* measurements and discontinuities in its highly-porous structure, ultrasonic testing is not an appropriate testing method for G0/150 product.

The study introduces a measurement method to identify the $UPV_{INDIRECT}$ data for AAC products. In practice, it is determined that 5 cm is the minimum interval between the transmitter and receiver probes to measure reliable transit time readings from AAC surfaces. However, it was experienced that due to the discontinuities on the surfaces and the highly porous nature, sometimes unexpected $UPV_{INDIRECT}$ values (higher or lower values than expected) were measured. To minimize the number of $UPV_{INDIRECT}$ measurements which have to be repeated several times and ensure measuring reliable data, taking measurements from the surface in sequences by changing the receiver position while the transmitter probe, positioned in a constant point is recommended. The data achieved are plotted in a graph showing the intervals between probes as a function of transit time readings (**Figure 5.14**). The slope of the linear regression between the distance and transit time gives the $UPV_{INDIRECT}$ value of the measured sample.

A relationship is determined between UPV_{DIRECT} and $UPV_{INDIRECT}$ data that allows converting $UPV_{INDIRECT}$ data taken on-site to UPV_{DIRECT} data. The $UPV_{INDIRECT}$ value is almost nine-twenty fifth (9/25), which is the equivalent of 0.36 as coefficient) of UPV_{DIRECT} values.

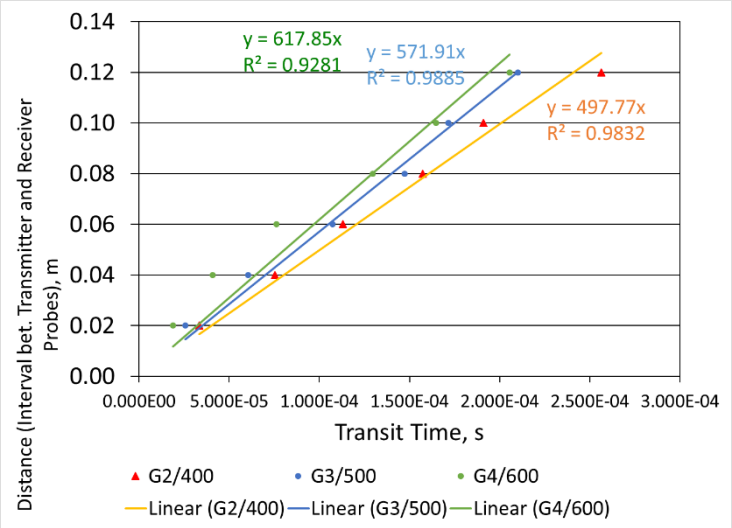

Figure 5.14. The graph showing distance data versus transit time readings where the slope of the linear regression gives the $UPV_{INDIRECT}$ data of the AAC products.

The *UPV* measurements, as a non-destructive method, are the only analysis that can be applied in-situ to monitor the effectiveness of treatment on the physical, hygric and physicomechanical properties of AAC materials. Therefore, some guidelines are provided for reliable *UPV* measurements that can be used both in-situ and in laboratory conditions as follows:

— In $UPV_{INDIRECT}$ measurements, a 2 cm interval between the transmitter and receiver probes can cause misleading readings. The experience during the ultrasonic testing of AAC samples showed that a minimum interval of 5 cm is required for taking $UPV_{INDIRECT}$ measurements, which are parallel to the surface.

— For UPV_{DIRECT} measurements, 2.5 cm distance between the transmitter and receiver probes that face each other can give misleading readings. The data showed that UPV_{DIRECT} measurements taken at a distance of 5 cm and above (until 20cm) give constant *UPV* values.

— To achieve reliable $UPV_{INDIRECT}$ readings, the surface measurements can be taken till 12 cm intervals between the transmitter and receiver probes. This means that the data corresponding to the deepest level in AAC samples can

be obtained with surface *UPV* measurements taken at 12 cm intervals. The 5cm interval measurements, if repeated give the $UPV_{INDIRECT}$ data underneath the surface level. However, the 12cm interval measurements, if repeated, give $UPV_{INDIRECT}$ data at the deepest level.

— *UPV* measurements revealed a strong correlation between direct transmission (UPV_{DIRECT}) and indirect ($UPV_{INDIRECT}$) transmission modes. This correlation is essential for converting $UPV_{INDIRECT}$ measurements taken on-site to UPV_{DIRECT} measurements of the material. In non-treated (control) AAC types (G2/400, G3/500, and G4/600), the ratio of $UPV_{INDIRECT}$ to UPV_{DIRECT} was determined to range from 0.22 and 0.31, with an average of 0.27. Therefore, for non-treated G2/400, G3/500, and G4/600, the conversion of $UPV_{INDIRECT}$ to UPV_{DIRECT} is calculated using **Equation 5.1**.

$$\boldsymbol{UPV_{INDIRECT} = 0.36 \times UPV_{DIRECT}} \quad \textbf{(5.1)}$$

— The ratio of $UPV_{INDIRECT}$ to UPV_{DIRECT} was decreased from one-fourth to almost one-fifth in G2/400, G3/500, and G4/600 after treatment with nano dispersive $Ca(OH)_2$ solution, resulting in the range of 0.24 and 0.58, with an average of 0.41. This conversion enables in-situ monitoring of the effect of nano $Ca(OH)_2$ treatment applied in the construction site. The correlation between $UPV_{INDIRECT}$ and UPV_{DIRECT} in treated G2/400, G3/500, and G4/600 is calculated by **Equation 5.2**.

$$\boldsymbol{UPV_{INDIRECT} = 0.40 \times UPV_{DIRECT}} \quad \textbf{(5.2)}$$

5.5 Discussion on Improving International Standards Related to AAC Products

Although there are several international standards and numerous research on AAC terminology, production (manufacturing), and performance characteristics in the literature, there is a lack of information about the procedures defined for each laboratory analysis, numerical data on the performance characteristics of AAC

products, and their qualification assessment. Therefore, it is necessary to explain the examination procedure, especially for ultrasonic testing, which is important for monitoring the effect of on-site treatment.

The AAC types tested in this study were found to be within the acceptable ranges determined by the standards for AAC products in density properties. The bulk density of the G0/150, G2/400, G3/500, and G4/600 samples with the values of 0.16, 0.42, 0.50, and 0.62 g/cm^3, were determined to belong to the density classes of 150, 400, 500, and 600, respectively, defined by European Standard (EN 12602:2015). In terms of hygric (moisture-related) properties, there is a lack of relevant information in national and international standards defining acceptable ranges for various AAC types. Therefore, there is a need to improve the content of international and national standards regarding the determination of numerical data for the performance characteristics of AAC types and the determination of acceptable ranges that contribute to the classification and characterization of AAC products.

The results of the laboratory analyses determined that the AAC types examined in this study had lower values in material properties compared to the same AAC types studied in the literature (**Table 5.4** and **Table 5.5**). The examined AAC types were found to have a slightly higher effective porosity, water vapor diffusion resistance index (μ-*value*), capillary water absorption coefficient (*A*-*value*), and penetrativity compared to the studies conducted by Andolsun (2006) and Jerman *et al*. (2013). This indicates that the examined AAC types are more susceptible to dampness problems.

The compiled data from the literature and the data achieved by this study were obtained by using the same laboratory tests defined in the standards. Therefore, the comparisons pointed out that AAC products of the various companies which are classified according to their bulk density, effective porosity (total open porosity), and compressive strength do not exhibit similar hygric properties. Therefore, the procedures for qualification assessment and classification of AAC products need to be improved. In this regard, the content of international standards related to their

production and performance properties should be revised by adding some performance parameters such as capillary suction, water vapor permeability, ultrasonic pulse velocity, and by defining acceptable ranges for these measurable parameters.

Table 5.4. Comparison of the AAC types examined in this study with the same AAC types examined in the literature in terms of material properties (Andolsun, 2006; Jerman *et al*., 2013).

Material Properties	**Reference**							
	This Study				**Andolsun (2006)**		**Jerman *et al*. (2013)**	
	G0/150	G2/400	G3/500	G4/600	G2/400	G4/600	G2/400	G3/50
Bulk density (ρ, g/cm^3)	0.16	0.42	0.50	0.62	0.4	0.6	0.36	0.5
Effective porosity (φ, % by volume)	90	81	77	72	78	69	84	78
Saturation coefficient (*S-value*, unitless)	0.32	0.45	0.52	0.64	0.46	0.62	-	-
Water vapor diffusion resistance index (μ*-value*, unitless)	2.2	3.7	4	4.1	3.7	3.1	3.3	3.1
Capillary water absorption coefficient (*A-value*, kg/m^{2}s$^{0.5}$)	0.052	0.068	0.070	0.123	0.026	0.037	0.031	0.044
Penetrativity (mm/s$^{0.5}$)	0.35	0.23	0.20	0.31	0.11	0.09	-	-

Table 5.5. Comparison of the AAC types examined in this study with the same AAC types examined in the literature in terms of physicomechanical properties (Andolsun, 2006; Jasinski, 2013).

Material Properties	**Reference**							
	This study			**Jasinski (2020)**			**Andolsun (2006)**	
	G2/400	**G3/500**	**G4/600**	**G2/400**	**G3/500**	**G4/600**	**G2/400**	**G4/600**
Bulk Density (ρ, g/cm^3)	0.42	0.50	0.62	0.37 – 0.44	0.46 – 0.53	0.56 – 0.61	0.40	0.60
UPV (m/s)	1461	1559	1759	1647 – 1801	1691 – 1849	1841 – 1942	1802 - 1974	1952 - 2282
E_{mod} (GPa)	0.83	1.12	1.81	-	-	-	1.4	2.1

CHAPTER 6

CONCLUSION

This research was shaped to investigate the impact of the alcohol dispersion of calcium hydroxide $Ca(OH)_2$ nanoparticles to control the excessive water absorption of Autoclaved Aerated Concrete (AAC) products by the penetration from their exposed surfaces by capillary suction. Laboratory analysis was performed on four common types of AAC products, including G0/150 (as an infill board), G2/400 (as a masonry infill unit), G3/500 (as a precast structural element), and G4/600 (as a load-bearing masonry unit). Some physical, hygric, physicomechanical, and microstructural properties of AAC types were analyzed before and after treatment to determine the effect of nano dispersive $Ca(OH)_2$ solution.

According to the obtained result of porosity characteristics, the effective porosity of G0/150 used as insulation boards is 90% by volume. However, highly porous AAC materials can absorb large amounts of water, restricting their use for outer blocks. The high water absorption capacity of AAC was determined as 500% by volume for G0/150 with the highest effective porosity (90% by volume) and 115% by volume for G4/600, with 72% by volume effective porosity. As effective porosity increases, the fine porosity, which are responsible for capillary water suction in the material matrix, decreases. G4/600 with the highest fine porosity ratio, has the highest capillary water suction value of 0.1225 $kg/m^2s^{0.5}$ among other AAC types. The high capillary suction properties make AAC materials susceptible to weathering cycles. The exposed surface of the AAC blocks experiences significant water penetration through capillary suction due to the highly porous structure of the AAC materials. Water-saturated AAC samples show lower durability in weathering conditions. Furthermore, as the moisture content in AAC materials increases, their compressive strength, tensile strength, thermal conductivity, and breathability decrease. In order

to control water absorption and capillary water suction characteristics, the exposed surface of AAC blocks should be coated. Surface coating not only can extend service life of AAC materials, but also decrease its high water absorption. For this purpose, nano dispersive calcium hydroxide $Ca(OH)_2$ was used in this study to control the high capillary water absorption properties of AAC materials. The nano dispersive $Ca(OH)_2$ treatment is compatible with AAC samples and slightly improves physical properties related to moisture and water intake since it does not significantly change the basic physical properties of AAC types. The main purpose of the nano treatment is to fill the fine pores and capillary pores to reduce the water penetration while still providing high vapor permeability.

Calcium hydroxide $Ca(OH)_2$ nanoparticles filled the periphery of the aeration pores and decreased their size which was observed by image analyses. Based on the porosity characteristics results, the reduction in fine pores and saturation coefficient (*S-value*) also detected after treatment. Therefore, nano dispersive $Ca(OH)_2$ solution applied on the surface perpendicular to the rising direction of AAC products decreased their capillary water suction without blocking their high water vapor permeability. The impact of nano dispersive solution on the hygric characteristics of AAC products was most noticeable in G4/600, which had the highest fine porosity ratio. After treatment, the water vapor permeability of the AAC samples increased as the water vapor passed through a short channel with limited pores not filled with nanoparticles. The treatment achieves a success on the surface perpendicular to the rising direction. However, the treatment process appears to adversely affect the capillary absorption behavior of AAC samples when applied to the rising direction surface. A significant increase was detected in *UPV* values after treatment. After treatment, a slight increase in density values resulted in greater *UPV* values, especially in denser AAC types. The nano dispersive Ca(OH)2 treatment appears to be significantly more successful in increasing physicomechanical properties and controlling the hygric behavior of G4/600 to a certain extent by;

— reducing effective porosity by 13%,

— reducing water absorption capacity by 12%,
— reducing *S-value* and fine porosity by 16% and 23%, respectively,
— reducing μ*-value* by 15%,
— increasing θ_C*-value* by 16%,
— reducing *A-value*, sorptivity, and penetrativity by 16%, 15%, and 12%, respectively,
— increasing *UPV* by 25%.

UPV measurements as a non-destructive technology are the only analyses that can be used in-situ to assess the efficiency of treatment on the physical, hygric, and physicomechanical characteristics of AAC materials. For this purpose, some criteria for accurate *UPV* measurements in both in-situ and laboratory settings were offered. In addition, based on the *UPV* measurements results, a strong correlation between UPV_{DIRECT} and $UPV_{INDIRECT}$ data was established which can enable $UPV_{INDIRECT}$ data collected on-site to be converted to UPV_{DIRECT} data.

Furthermore, Despite the existence of several international standards and numerous studies on AAC materials, there is a lack of numerical data specified for each AAC type in terms of their performance characteristics and qualification assessment. In this regard, the content of international standards has to be improved by including parameters related to AAC performances such as capillary suction, water vapor permeability, and ultrasonic pulse velocity.

REFERENCES

Ahmed, A., and Kamau, J. (2017). Sustainable Construction Using Autoclaved Aerated Concrete (Aircrete) Blocks. *Research and Development in Material Science, 1(4).*

Andolsun, S. (2006). *A Study on Material Properties of Autoclaved Aerated Concrete (AAC) and Its Complementary Wall Elements: Their Compatibility in Contemporary and Historıcal Wall Sections*, [Unpublished Master Thesis, Ankara: METU].

Arandigoyen, M., Bicer-Simsir, B., Alvarez, J., and Lange, D. (2006). Variation of microstructure with carbonation in lime and blended pastes. *Applied Surface Science, Volume 252(20),* 7562-7571.

Aroni, S. (2004). *Autoclaved Aerated Concrete - Properties, Testing and Design*. CRC Press.

ASTM C1585-20. Standard Test Method For Measurement Of Rate Of Absorption Of Water By Hydraulic-Cement Concretes.

ASTM C1660-10(2018). Standard Specification for Thin-bed Mortar for Autoclaved Aerated Concrete (AAC) Masonry.

ASTM C1686-09(2017). Standard Practice for Installation and Testing of Reinforced Autoclaved Aerated Concrete (AAC) Units.

ASTM C1691-21. Standard Specification for Unreinforced Autoclaved Aerated Concrete (AAC) Masonry Units.

ASTM C1692-18. Standard Practice for Construction and Testing of Autoclaved Aerated Concrete (AAC) Masonry.

ASTM C1693-11(2017). Standard Specification for Autoclaved Aerated Concrete (AAC).

ASTM C1694-09(2017). Standard Specification for Reinforced Autoclaved Aerated Concrete (AAC) Elements.

ASTM D 2845-08 – *Standard Test Method for Laboratory Determination of Pulse Velocities and Ultrasonic Constants of Rock* (2008). American Society for Testing and Materials, Philadelphia.

ASTM E96/E96M (2016). *Water Vapor Transmission of Materials*. American Society for Testing and Materials, Philadelphia.

Babé, C., Kidmo, D.K., Tom, A., Mvondo, R.R.N., Boum, R.B.E., Djongyang, N. (2020). Thermomechanical characterization and durability of adobes

reinforced with millet waste fibers (sorghum bicolor). *Case Studies in Construction Materials, 13*.

Badreddine, D., Beck, K., Brunetaud, X., Chaaba, A., Al-Mukhtar, A. (2020). Nanolime consolidation of the main building stone of the archaeological site of Volubilis (Morocco). *Journal of Cultural Heritge, 43,* 98-107.

Belkharchouche, D., Chaker, A. (2016). Effects of moisture on thermal conductivity of the lightened construction material. *International Journal of Hydrogen Energy, 41*, 1719-1725.

Beltagui, H., Sonebi, M., and Taylor. S. (2017). The Impact of Mix Design and Materials on the Microstructure of Autoclaved Aerated Concrete Blocks. *37th Cement and Concrete Science Conference.*

Billong, N., Boubakar, L., Bayiha, B. N., Njimbouombouo, S. M., Melo, U. C., Oti, J., Kinuthia, J. (2020). An investigation on the suitability of hydrated building lime from travertine limestone outcrop of Bogongo, South West of Cameroon. *Case Studies in Construction Materials, 13*.

Borsoi, G. (2017). *Nanostructured lime-based materials for the conservation of calcareous substrates. Architecture and the Built Environment*, [Doctoral dissertation, Delft University].

Boukhattem, L., Boumhaout, M., Hamdi, H., Benhamou, B., Nouh, F. A. (2017). Moisture content influence on the thermal conductivity of insulating building materials made from date palm fibers mesh. *Construction and Building Materials, 148,* 811-823.

BRE (1997). *Selecting Natural Building Stones*. Building Research Establishment in: Digest 420. 8p.

BS EN 12602 (2016). Prefabricated Reinforced Components of Autoclaved Aerated Concrete.

BS EN 772-11:2011. Determination of water absorption of aggregate concrete, autoclaved aerated concrete, manufactured stone, and natural stone masonry units due to capillary action.

BS EN ISO 13788 (2002). *Hygrothermal performance of building components and building elements* – Internal surface temperature to avoid critical surface humidity and interstitial condensation – Calculation methods. London: BSI, 2002.

Camino, M.S., León, F.J., Llorente, A., Olivar, J.M. (2014). Evaluation of the behavior of brick tile masonry and mortar due to capillary rise of moisture. *Materiales de Construcción, 64(314).*

Caner, E. (2011). *Limestone Decay in Historic Monuments and Consolidatıon with Nanodispersive Calcium Hydroxide Solutions*, [Unpublished Master Thesis, Ankara: METU].

Caner-Saltık, E.N., Schumann, I., Franke, L. (1998). Stages of damage in the structure of brick due to salt crystallization. *Conservation of Historic Brick Structures*. 137 Editor: Baer, N.S., Fitz, S., Livingston, R.A. UK, Shaftesbury: Donhead Publishing, pp. 47-58.

Charakterisierung, Mineralogische, and Zusammensetzung Der Naturwissenschaftlichen Fakult. "Mineralogy of Autoclaved Aerated Concrete and Characterization of Tobermorite - Advanced Analytical Methods and Effect of Changes in the Chemical Composition Jürgen Schreiner."

Chen, T.C., Yeung, M.R. and Mori, N. (2004). Effect of water saturation on deterioration of welded tuff due to freeze-thaw action. *Cold Reg Sci Technol 38*, 127–136.

Chen, G., Li, F., Jing, P., Geng, J., Si, Z. (2021). Effect of Pore Structure on Thermal Conductivity and Mechanical Properties of Autoclaved Aerated Concrete. *Materials 14(2)*, 1–28.

Çizer, Ö., Van Balen, K., Elsen, J., and Van Gemert, D. (2012). Real-time investigation of reaction rate and mineral phase modification of lime carbonation. *Construction and Building Materials, 65,* 741-751.

Colinart, T., Glouannec, P. (2021). Water vapor permeability of building materials: improved analysis of dry cup experiment. *1st International Conference on Moisture in Buildings (ICMB21).*

Cultrone G., Sebastián E., Ortega Huertas M. (2005). Forced and natural carbonation of limebased mortars with and without additives: Mineralogical and textural changes. *Cement and Concrete Research, Volume 35(12),* 2278-2289.

D'Armada, P., and Hirst, E. (2012). Nano-Lime for Consolidation of Plaster and Stone. *Journal of architectural con servation, 1,* 63-80.

Daehne, A., Herm, C. (2013). Calcium hydroxide nanosols for the consolidation of porous building materials - results from EU-STONECORE. *Heritage Science, 1(11).*

Davey, N. (1961). *A History of Building Materials,* London, The Camelot Press Ltd.

De Castro, E. (1978). Les methods de succion dans l'etude de l'alternation des pierres, *Deterioration and Protection of Stone Monuments International Symposium*, 2.2. Paris: UNESCO-RILEM.

Deng, C., Cai, W., Yin, J., Yang, F., Li, L. (2019). Influence of Moisture Content on Mechanical Properties of Autoclaved Aerated Concrete. *International Journal of Transportation Engineering and Technology, 5(4),* 97-102.

Desani, P., Soni, M., Gandhi, N., Mishra, V. (2016). Autoclaved Aerated Concrete: A Sustainable Alternate of Clay Brick Masonry in Form of Light Weight Concrete. *Global Research and Development Journal for Engineering (Recent Advances in Civil Engineering for Global Sustainability), 79.*

Drochytka, R. (2020). Influence of Fluidized Bed Combustion Fly Ash Admixture on Hydrothermal Synthesis of Tobermorite in the Mixture with Quartz Sand, High Temperature Fly Ash and Lime. *Construction and Building Materials, 230,* 1–11.

Drochytka, R, and Černý, V. (2020). Influence of Fluidized Bed Combustion Fly Ash Admixture on Hydrothermal Synthesis of Tobermorite in the Mixture with Quartz Sand, High Temperature Fly Ash and Lime. *Construction and Building Materials, 230,* 1–11.

Duano, H., Chen, B., and Lang, L. (2021). Novel Plastering Mortar Incorporating Cenospheres for Autoclaved Aerated Concrete Based on Magnesium Phosphate Cement. *Journal of Materials in Civil Engineering, 33(4).*

Edvin, E. C. (1929*). Cements, Limes and Plasters: their Materials, Manufacture, and Properties*. Nature 124, 439.

EN 12602:2016. Prefabricated reinforced components of autoclaved aerated concrete.

EN 15304. Determination of the freeze-thaw resistance of autoclaved aerated concrete.

EN 680:2006/Az1:2008. Determination of the drying shrinkage of autoclaved aerated concrete.

EN 771-4+A1:2015. Specification for masonry units–Part4: Autoclaved aerated concrete masonry units.

EN 772-10:2011. Determination of moisture content of calcium silicate and AAC.

EN 845-2:2013+A1:2016. Specification for ancillary components for masonry–Part2: Lintels.

Feng, C., and Janssen, H. (2021). Hygric Properties of Porous Building Materials (VII): Full-Range Benchmark Characterizations of Three Materials. *Building and Environment, 195*.

Feng, C, Janssen, H., Feng, Y., and Meng, Q. (2015). Hygric Properties of Porous Building Materials: Analysis of Measurement Repeatability and Reproducibility. *Building and Environment, 85*, 160–72.

Fernandeza, A. S., Villalba, L.S.G., Rabanal, M.E., and Fort, R. (2017). New nanomaterials for applications in conservation and restoration of stony materials: A review. *Materiales de Construcción, 67(325*), e107.

Fudge, C., Fouad, F., and Kligner, R. (2019). Developments in the Formulation and Reinforcement of Concrete (Second Edition). *Woodhead Publishing Series in Civil and Structural Engineering*, 345-363.

García-Vera, V. E., Tenza-Abril, A. J., Solak, A. M., Lanzón, M. (2020). Calcium hydroxide nanoparticles coatings applied on cultural heritage materials: Their influence on physical characteristics of earthen plasters. *Applied Surface Science, 504*.

Garrecht H. (1996). Corrosion of Building Materials Caused by Microclimatic and Weathering Attack. In C. Sjöström (Ed.), *Durability of Building Materials and Components 7, Vol.1*. London: E. & FN Spon, pp.150-159.

Ghaffari, E., Köberle, T., Weber, J. (2012). Methods of Polarising Microscopy and Sem to Assess the Performance of Nano-Lime Consolidants in Porous Solids. *12th International Congress on the Deterioration and Conservation of Stone.*

Giorgi, R., Ambrosi, M., Toccafondi, N., Baglioni, P. (2010). Nanoparticles for Cultural Heritage Conservation: Calcium and Barium Hydroxide Nanoparticles for Wall Painting Consolidation. *Chemistry A European Journal, Volume 16(31),* 9374-9382.

Gökmen, F. (2017). *Seismic Behavior of Autoclaved Aerated Concrete Reinforced Vertical Panel Buildings,* [Unpublished Master Thesis, Ankara: METU].

Grandet, B. (1975). *Physico-chemical mechanisms of the bond between clay and cement*. Proc., (3rd Int). Brick and Block Masonry Conf., H. Glitza and K. Göbel, eds., Bonn, Germany, 217–221.

Hamad, A. J. (2014). Materials, Production, Properties and Application of Aerated Lightweight Concrete: Review. *International Journal of Materials Science and Engineering, 2(2),* 152-157.

He, X., Yin, J., Yang, J., Liang, Q., and Wu, S. (2018). Effect of Dry-Wet Circulation on the Mechanical Properties and Pore Structure of Autoclaved Aerated Concrete. *Materials and technology 53(2),* 177-182.

Hirschwald, J. (1908). *Die Prüfung der Natürlichen Bausteine auf Ihre Wetterbestandigkeit*. Verlag von Wilhelm Ernst & Sohn, Berlin, p 675.

Holmes, S., and Wingte, M. (1997). *Building with Lime*, London, Intermediate Technology Publications.

Houst, Y., Alou, F., and Wittmann, F. H. (1983). Influence of Moisture Content on Mechanical Properties of Autoclaved Aerated Concrete. *Developments in Civil Engineering (August 2014),* 219–34.

Ioannou, I., Hamilton, A., and Hall, C. (2008). Capillary Absorption of Water and N-Decane by Autoclaved Aerated Concrete. *Cement and Concrete Research 38(6),* 766–71.

Jacobs, F. and Mayer, G. (1992). *Porosity and permeability of autoclaved aerated concrete, in: Proceedings of the Third RILEM International Symposium on Autoclaved Aerated Concrete* (p.71-75). Advances in Autoclaved Aerated Concrete, F.H. Wittmann, ed. A.A. Balkema, Rotterdam, Brookfield (ISBN 90-5410-086-9).

Jasiński, R. (2020). Identification of Stress States in Compressed Masonry Walls Using a Non-Destructive Technique (NDT). *Materials, 13*.

Jasiński, R., Drobiec, Ł., Mazur, W. (2019). Application of the Minor Destructive Test (MDT) method for determination of AAC masonry compressive strength. *Welding Technology Review, 91*.

Jerman, M., Keppert, M., Výborný, J., and Černý, R. (2013). Hygric, Thermal and Durability Properties of Autoclaved Aerated Concrete. *Construction and Building Materials, 41,* 352–59.

Kapala, S., and Dachowski, R. (2016). The influence of the Chalcedony on the Properties of Autoclaved Aerated Concrete. *Procedia Engineering, 161,* 699-703.

Karagiannis, N., Karoglou, M., Bakolas, A., Moropoulou, A. (2016). Building Materials Capillary Rise Coefficient: Concepts, Determination and Parameters Involved. *Building Pathology and Rehabilitation, 6*.

KÇS GAZBETON www.kcs.com.tr. Last accessed date: 20 October 2021.

Kočí, J., Maděra, J., Jerman, M., and Černý, R. (2019). Experimental Determination of Heat and Moisture Transport Properties of AAC in the Range of Subzero to Room Temperatures. *International Journal of Thermophysics, 40(1).*

Korniyenko, S.V., Vatin, N.I., Gorshkov, A.S. (2016). Heat and power characteristics analysis carried out for the residential building made of autoclaved aerated concrete blocks.

Koronthalyova, O., and Bagel, L. (2015). Effect of Carbonation on Long-Term Measurements of Sorption Isotherms of Autoclaved Aerated Concrete. *Advanced Materials Research, 1126,* 81–86.

Koudelka, T., Kruis, J., Madeˇra, J. (2015). Coupled shrinkage and damage analysis of autoclaved aerated concrete. *Applied Mathematics and Computation, 267,* 427-435.

Kunchariyakun, K., Asavapisit, S., and Sombatsompop, K. (2015). Properties of autoclaved aerated concrete incorporating rice husk ash as partial replacement for fine aggregate. *Cement and Concrete Composites, 55,* 11-16.

Kus, H. (2003). Silicon-based water repellents: Long-term performance evaluation by artificially accelerated ageing. *Surface Coatings International Part B: Coatings Transactions, 86*, 1-90.

Kus, H., Norberg, P. (1999). Evaluatıon of the Long-Term Performance of Water Repellants on Rendered Autoclaved Aerated Concrete. *Durability of Building Materials and Components, 8*, 980-988.

Lange, N. A. and Forker, G.M. (1967). *Handbook of Chemistry*. USA: McGraw-Hill, Inc.

Li, X., Liu, Z., Lv, Y., Cai, L., Jiang, D., Jiang, W., Jian, S. (2018). Utilization of municipal solid waste incineration bottom ash in autoclaved aerated concrete. *Construction and Building Materials, 178*, 175-182.

Liu, C., Hou, J., Hao, Y., Hao, H., and Meng, X. (2021). Effect of high strain rate and confinement on the compressive properties of autoclaved aerated concrete. *International Journal of Impact Engineering, 156*.

Massa, S., Amadori, M.L. (1990). "The environment and moisture content of the bricks", *Proceedings 4th Expert Meetings*, NATO-CCMS Pilot Study, Conservation of Historic Brick Structures, Berlin: Umweltbundesamt, Editör: Fitz, pp, 41-45.

Massari, G. & M. Massari (1993*). Damp Buildings*, Old and New. Rome: ICCROM.

Matsui, K., Kikuma, J., Tsunashima, M., Ishikawa, T., Matsuno, S. Y., Ogawa, A., Sato, M. (2011). In Situ Time-Resolved X-Ray Diffraction of Tobermorite Formation in Autoclaved Aerated Concrete: Influence of Silica Source Reactivity and Al Addition. *Cement and Concrete Research 41(5),* 510–19.

Matsuno, A., Ishızuka, S., Nguyen, T. L., Dung, N. T., Nguyen, V. T., Nguyen, H. G., Kawamoto, K. (2020). Comparison of Macropore Structures and Networks of Autoclaved Aerated Concrete Blocks Using Micro-Focus X-Ray Computed Tomography. *International Journal of GEOMATE 19(71),* 160–65.

Matsushita, F., Aono, Y., and Shibata. S. (2000). Carbonation Degree of Autoclaved Aerated Concrete. *Cement and Concrete Research 30(11),* 1741–45.

Melichar, J, Cerný, V., Fleischhacker, J., and Drochytka, R. (2018). Content of Aluminium Hydroxide in Lime-Silica Composite and Its Influence on Tobermorite Formation. *Materials Science Forum, 916*, 195–99.

Mold, P., & Godbey. R. (2005). Limewash: Compatible coverings for Coverings for Masonry and Stucco. *International Building Lime Symposium*, Orlando, Florida.

Moorehead, D.R. (1986). *Cementation by the carbonation of hydrated lime*. Cement and Concrete Research, Vol.16(5), 700-708.

Mostafa, N. Y. (2005). Influence of Air-Cooled Slag on Physicochemical Properties of Autoclaved Aerated Concrete. *Cement and Concrete Research 35(7),* 1349–57.

Naik, T., Malhotra, V. & Popovics, J. (2004). *The ultrasonic pulse velocity*. In V. Malhotra and N. Carino (Eds.)., Handbook on Nondestructive testing of concrete. CRC Press LLC.

Narayanan, N., and Ramamurthy, K. (2000a). Structure and Properties of Aerated Concrete: A Review. *Cement and Concrete Composites 22(5),* 321–29.

Narayanan, N., and Ramamurthy, K. (2000b) . Microstructural investigations on aerated concrete. *Cement and Concrete Research, 30,* 457-464.

Natali, I., Saladino, M. L., Andriulo, F., Martino, D.C., Caponetti, E., Carretti, E., Dei, L. (2014). Consolidation and protection by nanolime: Recent advances for the conservation of the graffiti, Carceri dello Steri Palermo and of the 18th century lunettes, SS. Giuda e Simone Cloister, Corniola (Empoli). *Journal of Cultural Heritage, 15(2),* 151-158.

Ndagi, A., Umar, A. A., Hejazi, F., Jaafar, M. S. (2019). Non-destructive assessment of concrete deterioration by ultrasonic pulse velocity: A review. *Sustainable Civil and Construction Engineering Conference (IOP Conference Series: Earth and Environmental Science), 357*.

Ordonez, S., Fort, R., & Garcia del Cura, M. A. (1997). Pore size distribution and the durability of a porous limestone. *Quarterly Journal of Engineering Geology and Hydrogeology, 30(3),* 221–230.

Pachideh, G., Gholhaki, M. (2019). Effect of pozzolanic materials on mechanical properties and water absorption of autoclaved aerated concrete. *Journal of Building Engineering, 26*.

Pehlivanlı, Z. O., Uzun, I., Demir, I. (2015). Mechanical and microstructural features of autoclaved aerated concrete reinforced with autoclaved polypropylene, carbon, basalt and glass fiber. *Construction and Building Materials, 96,* 428-433.

PN-89/B-06258(1989). Autoclaved Aerated Concrete.

Pražák J., and Lunk, P. (1992). *Capillary Suction of AAC, in: Proceedings of the Third RILEM International Symposium on Autoclaved Aerated Concrete* (p.119- 123). Advances in Autoclaved Aerated Concrete, F.H. Wittmann, ed. A.A. Balkema, Rotterdam, Brookfield. (ISBN 90-5410-086-9).

Qin, L., and Gao, X. (2019). Recycling of Waste Autoclaved Aerated Concrete Powder in Portland Cement by Accelerated Carbonation. *Waste Management, 89,* 254–64.

Qiu, Q. (2020). A State-of-the-Art Review on the Carbonation Process in Cementitious Materials: Fundamentals and Characterization Techniques. *Construction and Building Materials, 247*.

Qu, X, and Zhao, X. (2017). Previous and Present Investigations on the Components, Microstructure and Main Properties of Autoclaved Aerated Concrete – A Review. *Construction and Building Materials, 135*, 505–16.

Ramamurthy, K., and N. Narayanan. 2000. Influence of Composition and Curing on Drying Shrinkage of Aerated Concrete. *Materials and Structures (Materiaux et Constructions), 33(4),* 243–50.

Revilla, C. F., Ramirez, S. M., and Varela,M. B. (2006). Modelling of slaked lime-metakaolin mortar engineering characteristics in terms of process variables. *Cement & Concrete Composites, 28,* 458-467.

RILEM. (1980). Tentative Recommendations, Comission-25-PEM. Recommended test to measure the deterioration of stone and to access the effectiveness of treatment methods. *Materiaux and Construction. 13(73),* 173-253.

RILEM, 1993. *Recommended practice- RILEM Technical Commities: 78-MCA and 51-ALC. Autoclaved Aerated Concrete- Properties, Testing and Design.* S. Aroni, G. J. de Groot, M. J. Robinson, G. Svanholm and F.H. Wittman ed. Taylor & Francis Group, London and New York, 1993.

Rodriguez-Navarro, C., Vettori, I., Ruiz-Agudo, E. (2016). Kinetics and Mechanism of Calcium Hydroxide Conversion into Calcium Alkoxides: Implications in Heritage Conservation Using Nanolimes. *American Chemical Society, 32*, 5183-5194.

Różycka, A., and Pichór, W. (2016). Effect of perlite waste addition on the properties of autoclaved aerated concrete. *Construction and Building Materials, 120*, 65-71.

Seddighi, F., Pachideh, G., Salimbahrami, S.B. (2021). A study of mechanical and microstructures properties of autoclaved aerated concrete containing nano-graphene. *Journal of Building Engineering, 43*.

Sezemanas, G., Sinica, M., Zacharčenko, P., Pivenj, N., Mikulskis, D., Kligys, M. (2013). Influence of Zeolite Additive on the Properties of Plaster Used for External Walls from Autoclaved Aerated Concrete. *Materials Science (Medžiagotyra), 19(2),* 222-229.

Schober, G. (2005). The Most Important Aspects of Microstructure Influencing Strength of AAC. *Autoclaved Aerated Concrete Innovation and Development - Proceedings of the 4th International Conference on Autoclaved Aerated Concrete: 145–53*.

Schober, G. (2011). Porosity in Autoclaved Aerated Concrete (AAC): A Review on Pore Structure, Types of Porosity, Measurement Methods and Effects of Porosity on Properties. *Cement, Wapno, Beton (SPEC.ISSUE): 39–43*.

Schreiner, J., Goetz-Neunhoeffer, F., Neubauer, J., Volkmann, S., Bergold, S., Webler, R., Jansen, D. (2019). Advanced Rietveld Refinement and Sem Analysis of Tobermorite in Chemically Diverse Autoclaved Aerated Concrete. *Powder Diffraction 34(2)*, 143–50.

Sherin, K., and Saurabh, J. K. (2018). Review of Autoclaved Aerated Concrete: - Advantages and Disadvantages. *Proceedings of National Conference: Advanced Structures, Materials And Methodology in Civil Engineering.*

STP1356-EB. Structural Properties of Autoclaved Aerated Concrete Masonry.

Łaskawiec, K., Gębarowski, P., Misiewicz, L. (2018). Performance of autoclaved aerated concrete from the designer, developer, and user perspective. *CE Papers, 2*, 535-540.

Taşdemir, C. and Ertokat, N. (2002). Gazbetonun Fiziksel ve Mekanik Özellikleri Üzerine Bir Değerlendirme, Proceedings of 1. *Ulusal Yapı Malzemesi Kongresi ve Sergisi*, pp.425- 437, İstanbul: TMMOB Mimarlar Odası.

Tavukçuoğlu, A., Caner-saltik, E. N., Güney, B. A., Caner, E. (2016). Akdeniz havzasındaki kültürel mirasın korunması kapsamında yenilikçi nano taneli ürünler ile taş sağlamlaştırma işlemleri. TÜBİTAK Proje Sonuç Raporu.

Tavukçuoğlu, A., Grinzato, E. (2006). "Determination of critical moisture content in porous materials by IR thermography", QIRT (Quantitative InfraRed Thermography) *Journal, 3 (2),* 231-245.

Teutonico, J.M., (1988). *A Laboratory Manual for Architectural Conservators*, ICCROM, Rome, pp.32-122.

Tian, S. Q., Wang, K., Fan, L. W., Yu, Z. T., Ge, J. (2019). Effects of Sample Length on the Transient Measurement Results of Water Vapor Diffusion Coefficient of Porous Building Materials: A Case Study of Autoclave Aerated Concrete (AAC) with Various Porosities. *International Journal of Heat and Mass Transfer*, *135*, 209–19.

Timoshenko, S. (1970). *Strength of Materials, in: Chapter II*, Analysis of Stress and Strain, Van Nostrand Reinhold Company, Holland, p.53.

Topal, T. (1995) *Formation and Deterioration of Fairy Chimneys of the Kavak Tuff in Ürgüp-Göreme Area (Nevşehir-Turkey)*, Ph.D. Thesis, Department of Geological Engineering, Middle East Technical University, Ankara, pp.61-67.

Topal, T., and Sözmen, B. (2003). Deterioration mechanisms of tuffs in Midas monument. *Engineering Geology, 68(3–4)*, 201–223.

Torraca G. (1988). *Porous Building Materials* - Materials Science for Architectural Conservation, (3rd ed.). Rome, Italy: ICCROM.

TS EN 1015-19/A1 (2013). Methods of Tests for Mortar for Masonry-Part 19: *Determination of Water Vapor Permeability of Hardened Rendering and Plastering Mortars*. Ankara, Institute of Turkish Standards.

TS EN 12602 (2011). Prefabricated Reinforced Components of Autoclaved Aerated Concrete. Ankara, Institute of Turkish Standards.

TS EN ISO 12572 (2001). Hygrothermal performance of building materials and products - *Determination of water vapor transmission properties.* Ankara, Institute of Turkish Standards.

TS EN ISO 7783 (2012). Paint and Varnishes - *Determination of Water Vapour Transmission Properties* - Cup Method. Ankara, Institute of Turkish Standards.

Tunçoku, S.S. (2001). *Characterization of Masonry Mortars used in Some Anatolian Seljuk Monuments in Konya, Beyşehir and Akşehir*, Ph.D Thesis, METU, Ankara, 128p.

Tuominen, E., and Vinha, J. (2019). Calculation method to determine capillary properties of building materials with automatic free water intake test. *Central European Symposium on Building Physics 2019 (MATEC Web of Conferences), 282*.

Ünal, M., Altunok, E. (2019). Determınatıon of Water Absorptıon Properties of Natural Buıldıng Stones and Theır Relatıon to Porosıty. *Engineering Sciences, 14(1),* 39-45.

UNE-EN 15304:2011. Determination of the freeze-thaw resistance of autoclaved aerated concrete.

UNE-EN 679:2006. Determination of the compressive strength of autoclaved aerated concrete.

UNE-EN 680:2006. Determination of the drying shrinkage of autoclaved aerated concrete.

Van Balen, K. (2005). Carbonation reaction of lime, kinetics at ambient temperature. *Cement and Concrete Research, 35*, 647-657.

Vejmelková, E., Pavlíková, M., Jerman, M., & Černý, R. (2009). Free Water Intake as Means of Material Characterization. *Journal of Building Physics, 33(1),* 29–44.

Wakili, K. G., Hugi, E., Karvonen, L., Schnewlin, P., Winnefeld, F. (2015). Thermal Behaviour of Autoclaved Aerated Concrete Exposed to Fire. *Cement and Concrete Composites, 62*, 52–58.

Washburn, E. W. (1921). *The Physical Review (The Dynamıcs of Capıllary Flow)*.

Yi, S. Y., Fan, L. W., Fu, J. H., Xu, X., Yu, Z. T. (2016). Experimental Determination of the Water Vapor Diffusion Coefficient of Autoclaved Aerated Concrete (AAC) via a Transient Method: Effects of the Porosity and Temperature. *International Journal of Heat and Mass Transfer, 103,* 607–10.